Durham E-Theses

A Quantum Degenerate Mixture of ^{87}Rb and ^{133}Cs

MCCARRON, DANIEL,JOHN

How to cite:

MCCARRON, DANIEL,JOHN (2011) *A Quantum Degenerate Mixture of ^{87}Rb and ^{133}Cs*, Durham theses, Durham University. Available at Durham E-Theses Online: http://etheses.dur.ac.uk/3242/

Use policy

The full-text may be used and/or reproduced, and given to third parties in any format or medium, without prior permission or charge, for personal research or study, educational, or not-for-profit purposes provided that:

- a full bibliographic reference is made to the original source
- a link is made to the metadata record in Durham E-Theses
- the full-text is not changed in any way

The full-text must not be sold in any format or medium without the formal permission of the copyright holders.

Please consult the full Durham E-Theses policy for further details.

Academic Support Office, Durham University, University Office, Old Elvet, Durham DH1 3HP
e-mail: e-theses.admin@dur.ac.uk Tel: +44 0191 334 6107
http://etheses.dur.ac.uk

A Quantum Degenerate Mixture of ^{87}Rb and ^{133}Cs

Daniel J. McCarron

Abstract

This thesis reports the formation of a dual-species Bose-Einstein condensate of ^{87}Rb and ^{133}Cs in the same trapping potential. Quantum degenerate mixtures exhibit rich physics inaccessible to single species experiments and provide an ideal starting point for the creation of ultracold dipolar molecules. These molecules offer a wealth of new research avenues including precision metrology, quantum simulation and computation.

The experimental method exploits the efficient sympathetic cooling of ^{133}Cs via elastic collisions with ^{87}Rb, initially in a magnetic quadrupole trap and subsequently in a levitated optical trap. Evaporative cooling in the dipole trap must compete against a high interspecies three-body inelastic collision rate $\sim 10^{-25} - 10^{-26}$ cm^6/s. The two condensates each contain up to 2×10^4 atoms and exhibit a striking phase separation, revealing the mixture to be immiscible due to strong repulsive interspecies interactions. Sacrificing all the ^{87}Rb during the cooling leads to the creation of single-species ^{133}Cs condensates of up to 6×10^4 atoms. In addition this thesis reports the observation of an interspecies Feshbach resonance at 181.7(5) G and the creation of a pure sample of Cs_2 molecules via magneto-association on the 4(g)4 resonance at 19.8 G. These results represent important steps towards the creation of ultracold polar RbCs molecules.

A Quantum Degenerate Mixture of ^{87}Rb and ^{133}Cs

Daniel J. McCarron

A thesis submitted in partial fulfilment
of the requirements for the degree of
Doctor of Philosophy

Department of Physics
Durham University

September 19, 2011

Contents

Page

Abstract **i**

Contents **ii**

Declaration **v**

Acknowledgements **vi**

1 Introduction **1**
- 1.1 Ultracold Mixtures . . . 2
- 1.2 Ultracold Polar Molecules . . . 3
- 1.3 A Mixture of Rubidium and Caesium . . . 6
- 1.4 Overview of Thesis . . . 9
- 1.5 Publications . . . 10

2 Basic Theory **11**
- 2.1 Ultracold Collisions . . . 11
  - 2.1.1 Elastic Collisions . . . 11
  - 2.1.2 Behaviour of the Scattering Length . . . 15
  - 2.1.3 Inelastic Collisions . . . 16
- 2.2 Feshbach Resonances . . . 18
  - 2.2.1 Magneto-association . . . 20
- 2.3 Bose-Einstein Condensation . . . 21
  - 2.3.1 Origin of BEC . . . 21
  - 2.3.2 A Bose Gas in a Harmonic Trap . . . 23
  - 2.3.3 The Thomas-Fermi Approximation . . . 26
  - 2.3.4 Tunable Interactions . . . 28
  - 2.3.5 Condensate Expansion . . . 29
- 2.4 Quantum Degenerate Mixtures . . . 30
- 2.5 Magnetic Trapping . . . 32
  - 2.5.1 Majorana Transitions . . . 34
  - 2.5.2 Magnetic Levitation . . . 35
- 2.6 RF Evaporation in a Quadrupole Trap . . . 36
- 2.7 Optical Trapping . . . 37

3 Experimental Apparatus: New Tools and Upgrades 39
3.1 Overview . . . 40
3.2 Optical Frequencies . . . 40
3.3 Laser System Overview . . . 41
3.3.1 Optical Setup . . . 42
3.4 Laser Frequency Stabilisation . . . 44
3.4.1 Modulation Transfer Spectroscopy . . . 44
3.4.2 Frequency Modulation Spectroscopy . . . 55
3.4.3 Comparing modulation transfer spectroscopy with FM spectroscopy . . . 56
3.5 Slave Laser Setup . . . 57
3.6 Magnetic and RF Coils . . . 59
3.6.1 Magnetic Field Coils . . . 59
3.6.2 RF Coils . . . 62
3.7 Double MOT System . . . 62
3.7.1 Pyramid MOT . . . 62
3.7.2 Science MOT . . . 64
3.8 The Hybrid Trap . . . 65
3.8.1 Dipole Trap Setup . . . 66
3.8.2 The Loading Trap . . . 69
3.8.3 The Levitated Trap . . . 70
3.9 Diagnostics . . . 73
3.9.1 Absorption Imaging . . . 74
3.9.2 Fluorescence Detection . . . 77
3.9.3 Selective control of the ^{133}Cs MOT number . . . 78
3.9.4 Stern-Gerlach Separation . . . 78
3.10 Experimental Control . . . 79

4 Optimisation and Characterisation 81
4.1 Pyramid MOT . . . 81
4.2 Science MOT . . . 84
4.3 Compressed MOT . . . 85
4.4 Optical Molasses . . . 86
4.5 Optical Pumping . . . 86
4.6 Magnetic Trap Loading . . . 90
4.7 Hybrid Trap Characterisation . . . 90
4.7.1 Trap Depth . . . 90
4.7.2 Trap Frequencies . . . 92

5 ^{87}Rb BEC in a Hybrid Trap 94
5.1 RF Evaporation in the Quadrupole Trap . . . 94
5.2 Aligning and Loading a Single Beam Hybrid Potential . . . 97
5.3 Evaporation in the Hybrid Trap to BEC . . . 100
5.4 Condensate Properties . . . 101
5.5 The Crossed Dipole Trap . . . 104

5.6 Adiabatic Rapid Passage . . . 105
5.7 Sympathetic Cooling in ^{87}Rb . . . 107
5.8 A Spinor Condensate in ^{87}Rb . . . 110

6 An Ultracold Mixture of ^{87}Rb and ^{133}Cs 112
6.1 Precooling and Loading the Dipole Trap . . . 112
6.2 Interspecies Three-Body Loss . . . 115
6.3 ^{133}Cs Bose-Einstein Condensation . . . 117
6.4 A Tunable Quantum Gas . . . 120
6.5 An Ultracold Molecular Gas . . . 122
6.6 A Dual-Species BEC of ^{87}Rb and ^{133}Cs . . . 124
6.7 Immiscibility in a Degenerate Mixture . . . 125
6.8 An Interspecies Feshbach Resonance . . . 128

7 Conclusions and Outlook 130
7.1 Summary . . . 130
7.2 Outlook . . . 132
7.2.1 Towards a Quantum Gas of Polar RbCs Molecules . . . 132
7.2.2 A Mixture of ^{85}Rb and ^{133}Cs . . . 135
7.2.3 ^{133}Cs BEC at High Bias Fields . . . 136
7.2.4 Concluding Remarks . . . 137

A Atomic Properties 139

B Atom Number Calculations 140
B.1 Fluorescence Detection . . . 140
B.2 Absorption Imaging . . . 141

C Coil Parameters 144

D Electronics 146

Bibliography 148

Declaration

I confirm that no part of the material offered has previously been submitted by myself for a degree in this or any other University. Where material has been generated through joint work, the work of others has been indicated.

Daniel J. McCarron
Durham, September 19, 2011

The copyright of this thesis rests with the author. No quotation from it should be published without their prior written consent and information derived from it should be acknowledged.

Acknowledgements

The work presented in this thesis could not have been completed without the guidance, support and encouragement of faculty, friends and family members. First and foremost I would like to thank my supervisor Simon Cornish for his guidance, enthusiasm and constant support. Simon's training has not only impacted upon my behaviour in the lab but shaped me as a person providing skills that I will carry with me through life. I am hugely grateful to him for proof reading various drafts of this thesis. I would also like to thank my co-supervisor Ifan Hughes for always being happy to aid my understanding of various physical concepts during the course of my studies.

I have been fortunate to work with many motivated and talented people on the Durham RbCs mixture experiment. I thank Margaret Harris and Patrick Tierney for their patience when teaching me how to run the experiment. It has been a pleasure to work alongside the current team of PhD students Daniel Jenkin, Michael Köppinger and Kirsteen Butler. Steve Hopkins was instrumental in designing and modeling the dipole trap. Special thanks go to Hung Wen Cho for his contagious passion for experimental physics. Thanks also go to our neighbours and fellow members of 'The Cornish Division' Sylvi Händel, Anna Marchant and Time Wiles. In addition, I am grateful to the ever expanding Durham AtMol group for providing a friendly and stimulating environment in which to work.

The technical staff in the Durham physics department must also be thanked for their help. I am especially grateful to Phil Armstrong, Steve Lishman, Malcolm Robertshaw and Lee Bainbridge from the mechanical workshop and John Scott from the electronics workshop. Their work has contributed towards essential parts of our experiment.

Thanks to all at Durham Amateur Rowing Club, especially the Men's Senior Squad, my surrogate family in the north east. The escapism provided on the river Wear has been invaluable. I would also like to thank Lucy for her support during the writing of this thesis.

I thank my brother, Tom for his friendship and providing laughter during our late night conversations. Finally I want to thank my Mum and Dad for their endless love and support, from the pre-paper round cup of tea to the countless journeys across the Pennines. Thank you for pointing me in the right direction.

This thesis is dedicated to Mum and Dad,
for all of the 'thought-support'.

Chapter 1

Introduction

The realisation and development of laser cooling and trapping neutral atoms [1] led to the birth of the field of ultracold atomic gases in the 1980s and enabled the preparation of dilute atomic clouds at temperatures typically in the microkelvin (μK) range. A major goal from the outset in this new and rapidly developing field was the experimental realisation of Bose-Einstein condensation (BEC). However, the required temperatures for this elusive state of matter are typically in the sub-microkelvin regime and cannot be achieved by laser cooling alone. Subsequent evaporative cooling in conservative traps [2] made the achievement of BEC possible in 1995 for ^{87}Rb , ^{23}Na and ^{7}Li [3–5]. The experimental milestones of laser cooling and trapping, and Bose-Einstein condensation were rewarded with Nobel prizes in 1997 and 2001 respectively [6–10].

Following these advances the number of elements and isotopes that have been cooled to quantum degeneracy has expanded dramatically to consist of both bosonic and fermionic species. For some species, such as ^{85}Rb [11] and ^{133}Cs [12], BEC has only been possible due to the exceptional control over atomic interactions provided by Feshbach resonances [13].

The proliferation of degenerate species has accompanied pioneering work investigating the properties and behaviour of quantum degenerate systems. The continued rapid progress of this field is driven by a combination of new experimental techniques evolving with theoretical advances. Landmark results include the observation of interference between two condensates [14],

the demonstration of the atom laser [15, 16], the creation of vortices in superfluid quantum gases [17, 18] and the formation of bright matter-wave solitons [19, 20]. When combined with optical lattices the field of ultracold atoms is linked to the world of condensed matter physics. Ultracold atoms confined in these arrays of optical micro-potentials have a band structure comparable to that in solid state physics [21]. Precise control of the lattice parameters allows this model system to address solid-state physics problems including the Mott insulator transition [22]. In recent years the field of ultracold quantum gases has greatly diversified with one new research avenue being the production and study of ultracold mixtures. Work and progress made in this specific area is discussed in section 1.1.

A key feature in the field of ultracold quantum gases is the full control over interactions through the s-wave scattering length. Feshbach resonances allow the sign and magnitude of the scattering length to be tuned. These features enable control of interactions in degenerate clouds and represent an essential tool to manipulate the behaviour of ultracold atoms [12]. The exquisite and full control achieved over all degrees of freedom in atomic quantum gases has given rise to substantial interest in obtaining a similar level of control in molecular quantum systems. In this field a major research target is the production of a Bose-Einstein condensate of ground state molecules. The complex internal structure of molecules would result in molecular BECs having many internal degrees of freedom allowing the study of novel chemical and physical processes. Molecular condensates have been realised for the special case of long lived Feshbach molecules composed of fermions [23–25] and have led to studies of the crossover regime between strongly and weakly bound fermionic pairs [26]. Away from this special case other more general methods for the production of ultracold molecules are making rapid progress and are discussed in section 1.2.

1.1 Ultracold Mixtures

Quantum degenerate mixtures [27–38] of atomic gases are currently the focus of intensive experimental and theoretical research, exhibiting rich physics inaccessible to single species experiments. Phase separation of the constituent

gases is a particularly dramatic example [28, 34–36]. In an optical lattice, the myriad of quantum phases for two different atomic species [39, 40] goes far beyond the seminal observations of the superfluid to Mott-insulator transition [22] and offers many intriguing applications. Amongst these applications, the creation of degenerate samples of heteronuclear ground state molecules is of paramount interest [41].

Sympathetic cooling is a valuable technique in mixture experiments. Here species with small elastic to inelastic collision ratios are efficiently cooled through elastic collisions with a second evaporatively cooled species. This technique was first demonstrated in a mixture of ^{87}Rb in different hyperfine states [27]. In spin polarised fermionic samples *s*-wave collisions are forbidden and sympathetic cooling in the only possible route to Fermi degeneracy [29]. This is not the case for a mixture of fermionic spin states which enabled the first observation of Fermi degeneracy in an ultracold quantum gas [42].

Efficient sympathetic cooling relies on a non-zero interspecies elastic collision cross-section. This and other collisional dynamics of a two-species mixture rely critically on both the intra- and interspecies interactions. This added layer of complexity in mixture experiments becomes apparent when considering the example of a Bose-Fermi mixture of ^{40}K - ^{87}Rb. Here the single species scattering lengths are both positive making each degenerate species separately stable. However, the *interspecies* scattering length is negative resulting in the degenerate mixture becoming unstable against collapse when the number of *either* species is above a critical value [43].

1.2 Ultracold Polar Molecules

Ultracold molecular quantum systems offer many new and exciting directions of scientific research [41, 44, 45]. Theoretical proposals for these systems range from precision metrology [46] and ultracold chemistry [47] to simulations of many-body quantum systems [48]. Within this field polar molecules are a subject of significant interest. Such molecules possess permanent electric dipole moments which give rise to anisotropic, long range dipole-dipole interactions. These interactions differ greatly from the isotropic, short-range

contact interaction commonly encountered in quantum degenerate atomic gases [49]. For a polarised dipolar gas in which all dipoles point in the same direction the energy due to the dipole-dipole interaction is [50]

$$V_{\mathrm{dd}} = \frac{C_{\mathrm{dd}}}{4\pi} \frac{(1 - 3\cos^2\theta)}{r^3}, \tag{1.1}$$

where r is the interparticle distance and θ is the angle between the relative position of the particles and the direction of polarization. The constant C_{dd} is d^2/ϵ_0 for particles with a permanent electric dipole moment d (ϵ_0 is the permittivity of vacuum) and $\mu_0\mu^2$ for particles with a permanent magnetic dipole moment μ (μ_0 is the permeability of vacuum). The anisotropic and long range ($\sim 1/r^3$) character of the dipole-dipole interaction is clear from equation 1.1. This equation shows that the dipole-dipole interaction is attractive for dipoles in a 'head to tail' configuration ($\theta = 0$) and repulsive, with half the strength of the previous case, for dipoles sitting side by side ($\theta = \pi/2$). For a 'magic angle' of $\theta_{\mathrm{m}} = \arccos(1/\sqrt{3}) \simeq 54.7°$ the dipole-dipole interaction is zero. To measure the absolute strength of the dipole-dipole interaction between two particles of mass m the 'dipole length' is defined as $a_{\mathrm{dd}} = \frac{C_{\mathrm{dd}} m}{12\pi\hbar^2}$. The dipole length provides a length scale comparable to the s-wave scattering length, a, and is often quoted in units of the Bohr radius, a_0, where $a_0 = 0.0529$ nm. Table 1.1 presents the dipole moments and dipole lengths for various atoms and molecules. Here electric dipole moments are given in debye, D, where 1D $\simeq 0.39\ e a_0$. In order for dipole-dipole interactions to be observable in atomic gases the contact interaction must be weakened such that $a \lesssim a_{\mathrm{dd}}$. This has been done for ^{39}K using a Feshbach resonance to reduce a to 0.06 a_0 [51].

Polar molecules are a promising candidate to realise strongly correlated dipolar quantum gases. In order for a molecule to have a significant electric dipole moment it must be heteronuclear, with the exception of long-range homonuclear Rydberg molecules [54]. The molecule must also be in a low rovibrational state as the dipole moment scales with r^{-7}, where r is the internuclear separation within the diatomic molecule [56]. Finally an external electric field must be applied to the molecules in the laboratory frame in order to polarise the molecular sample and create an electric dipole moment.

The orientation of the molecular dipoles is controlled by the direction of the

Species	Dipole moment	a_{dd} (a_0)
^{87}Rb	0.5 μ_{B}	0.2
^{133}Cs	0.75 μ_{B}	0.6
^{52}Cr	6 μ_{B}	15
^{40}K - ^{87}Rb	0.57 D	4×10^3
^{87}Rb - ^{133}Cs	1.25 D	3×10^4

Table 1.1: Comparison of the dipole moments and dipole lengths for various atoms and molecules in the atomic and rovibrational grounds states respectively. The quoted dipole length for ^{52}Cr and the dipole moment for ^{40}K - ^{87}Rb were determined experimentally [52, 53]. The data for ^{87}Rb - ^{133}Cs molecules are theoretical predictions [54, 55].

applied external electric field. This control, in combination with control of the trapping geometry, enables the interactions within the quantum system to be tuned with exquisite sensitivity and may be used to suppress inelastic collisions [57]. When loaded onto an optical lattice the long-range interaction of these dipoles leads to a rich spectrum of quantum phases [58] and offers potential applications for quantum information processing [59] and simulation [60].

Realising an ultracold quantum gas of polar molecules is challenging, in part due to the complex internal structure that makes molecules interesting. This complexity is due to additional rotational and vibrational degrees of freedom and renders standard laser cooling techniques ineffective for the majority of molecules. Experimental approaches towards the creation of a quantum degenerate gas of polar molecules have mostly followed two routes.

The first approach involves the direct cooling of ground-state polar molecules. This has led to the development of many new experimental techniques [41], including Stark deceleration [61] and buffer gas cooling [62]. Typically these methods have only attained final temperatures in the millikelvin regime and phase-space densities far from degeneracy. Further advances in direct cooling will probably require the development of sympathetic cooling [63] or laser cooling [64, 65].

The second indirect approach uses the powerful laser cooling techniques ap-

plicable to atoms and starts with a high phase-space density atomic gas. Atom pairs are then associated into ground state molecules via an appropriate photoassociation scheme in which the molecular binding energy is removed by a photon [66]. The challenge of this indirect approach is to find an efficient scheme in which the population is transferred into a single target molecular state without any heating of the sample. In recent years there have been a large number of successes using the indirect approach and several schemes have produced molecules in their rovibrational ground state [67–71]. Of particular significance are two experiments that have produced ground state molecular samples close to quantum degeneracy in ^{40}K-^{87}Rb [53] and Cs_2 [72, 73]. These experiments follow a two step scheme in which weakly bound molecules are first made via magneto-association using a Feshbach resonance [74]. The resulting Feshbach molecules are then transferred into the rovibrational ground state using stimulated Raman adiabatic passage (STIRAP) [75]. The efficiency of this transfer can be enhanced using the magnetic field to tune the character of the weakly bound Feshbach molecule. Although this approach is limited to molecules whose constituent atoms can be laser cooled, near 100 % conversion efficiency is possible with little heating of the gas.

1.3 A Mixture of Rubidium and Caesium

A mixture of ^{87}Rb and ^{133}Cs offers many interesting and exciting prospects for experiments on the production of a quantum degenerate mixture. Such a mixture would be an ideal starting point for the production of ^{87}Rb - ^{133}Cs molecules in the rovibrational ground state providing to be an ideal gateway into the realm of dipolar molecular quantum gases. Both species have been separately condensed [3, 12] and the intraspecies two-body interactions are now well understood [76, 77].

A ^{87}Rb - ^{133}Cs mixture exhibits complementary scattering properties. The ^{87}Rb scattering length is essentially independent of magnetic field with only a few narrow Feshbach resonances up to 170 mG wide at accessible magnetic fields [76]. In contrast, ^{133}Cs has a rich Feshbach structure with many broad and narrow resonances combined with a large background scattering length

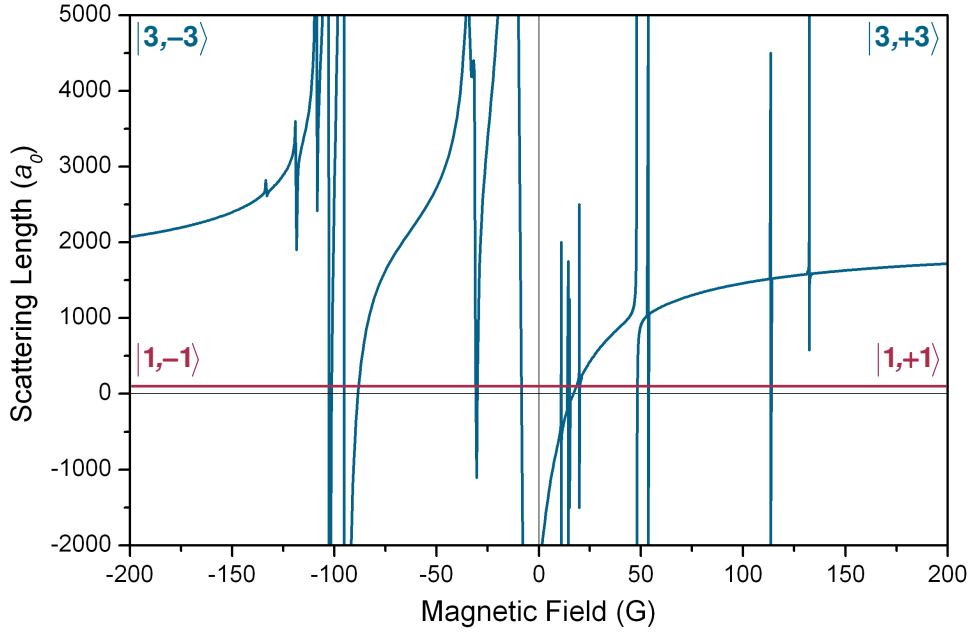

Figure 1.1: Single species scattering lengths as a function of the applied bias field for ^{87}Rb (red) and ^{133}Cs(blue) atoms in the $|F = 1, m_F = \pm 1\rangle$ and $|F = 3, m_F = \pm 3\rangle$ states respectively. The region of negative bias field corresponds to the low field seeking spin states while the positive bias field region corresponds to the high field seeking spin states. The data for this figure is taken from [82].

of $a_{\mathrm{Cs}} \simeq 2400\ a_0$ [78]. In previous work this structure has been exploited to Feshbach associate Cs_2 dimers [79], create Efimov trimer states [80] and tune interactions in a ^{133}Cs condensate [12, 81]. Figure 1.1 shows the scattering lengths for the ^{87}Rb $|F = 1, m_F = \pm 1\rangle$ states (red line) and ^{133}Cs $|F = 3, m_F = \pm 3\rangle$ states (blue line) for bias fields up to 200 G. Here F denotes the total angular momentum and m_F the magnetic quantum number. These complementary properties enable the ^{133}Cs scattering length to be tuned without affecting the ^{87}Rb scattering length and will allow the relative strength of interactions in this mixture (equation 2.53) to be varied.

^{87}Rb is a commonly condensed species and is an excellent buffer gas for sympathetic cooling due to its fortuitously high ratio of elastic to inelastic collisions. This is due to the cancellation of the spin-spin and second order spin-orbit interactions resulting in an anomalously low dipolar relaxation rate. In contrast ^{133}Cs exhibits high two- and three-body inelastic losses

associated with the rich Feshbach spectrum in ^{133}Cs. These complicate the evaporative cooling of ^{133}Cs and make the ^{133}Cs scattering length a critical parameter. Indeed such complications have meant that prior to this work only two groups had achieved Bose-Einstein condensation of ^{133}Cs [12, 83].

When in the $|1, \pm 1\rangle$ and $|3, \pm 3\rangle$ states for ^{87}Rb and ^{133}Cs respectively the magnetic moment-to-mass ratios differ by less than 2% for bias fields less than $\sim$ 90 G. This allows both species to be levitated against gravity using the same magnetic field gradient and ensures excellent spatial overlap between the two clouds. The mass ratio of these species allows rethermalisation to be achieved after few interspecies elastic collisions [84]. Both of these features are important prerequisites for efficient sympathetic cooling.

Previous work with ^{87}Rb - ^{133}Cs mixtures includes the sympathetic cooling of ^{133}Cs in $|4, +4\rangle$ via ^{87}Rb in $|2, +2\rangle$ in a magnetic trap down to several μK by the Pisa group led by E. Arimondo. Here rethermalisation measurements determined the interspecies collisional cross-section to be 595 a_0, in agreement with a theoretical prediction [85, 86]. The group of D. Meschede in Bonn has demonstrated sub-μK sympathetic cooling of ^{133}Cs via ^{87}Rb in a magnetic trap using the same spin states as the Pisa group. Here the sympathetic cooling dynamics were used to derive a lower limit of 200 a_0 for the modulus of the ^{87}Rb - ^{133}Cs interspecies triplet s-wave scattering length [87].

Finally a group led by R. Grimm and H.-C. Nägerl in Innsbruck work with an optically trapped mixture of ^{87}Rb and ^{133}Cs in the $|1, +1\rangle$ and $|3, +3\rangle$ states respectively. This group have located 23 interspecies Feshbach resonances in this mixture [88]. These features permit, in principle, the control of interspecies interactions and offer numerous resonances on which to explore the magneto-association of RbCs Feshbach molecules.

Crucially, the RbCs molecule in the rovibrational ground state is stable against atom exchange reactions of the form RbCs + RbCs $\rightarrow$ Rb_2 + Cs_2, unlike the KRb molecule [89]. Compared to other bi-alkali molecules the RbCs molecule in the rovibrational ground state is predicted to carry a comparatively large electric dipole moment of 1.25 debye [55]. It is anticipated that these bosonic molecules will eventually be used to produce the first condensate of polar molecules.

Recently the Innsbruck experiment have reported on the simultaneous production of Bose-Einstein condensates of ^{87}Rb and ^{133}Cs in separate optical dipole traps [90]. This separation is performed to avoid significant interspecies three-body losses and enables the creation of ^{87}Rb condensates containing 2×10^4 atoms and ^{133}Cs condensates containing 1×10^4 atoms. After preparation the condensates can be merged for mixed species quantum gas experiments and the production of RbCs Feshbach molecules [91].

The latest theoretical refinement of the interspecies collision potential [92] shows excellent agreement with the published Feshbach spectrum [88] and the observation of a weakly bound molecular level $\simeq h \times 100$ kHz below threshold [90, 91]. These calculations indicate a current best estimate for the background interspecies scattering length of $\simeq 650\ a_0$ for the states used in this work.

1.4 Overview of Thesis

This thesis is organised as follows:

• Chapter 2 gives an overview of the theoretical background required to understand the results presented in this thesis. This chapter is not intended to be a complete guide, more complete information can be found in the references therein.

• Chapter 3 describes improvements and upgrades made to the experimental apparatus and method. Existing features from the original apparatus are described in references [93, 94].

• Chapter 4 presents and discusses the results from the optimisation and characterisation of the apparatus and experimental sequence up to and including the loading of the magnetic quadrupole trap.

• Experiments using ^{87}Rb alone in both the single beam hybrid trap and the crossed-dipole trap are explored in chapter 5. The route to ^{87}Rb BEC in these hybrid potentials is presented and condensate dynamics are investigated.

• Chapter 6 contains results from experiments working with an ultracold mixture of ^{87}Rb and ^{133}Cs. Key results include a new route to ^{133}Cs BEC and the production of a dual-species condensate of ^{87}Rb and ^{133}Cs.

• Conclusions are drawn in chapter 7 and an outlook is given towards future experiments using the ^{87}Rb -^{133}Cs apparatus.

1.5 Publications

The following publications have been prepared during the course of this work:

- **Modulation transfer spectroscopy in atomic rubidium**
  D. J. McCarron, S. A. King and S. L. Cornish
  Meas. Sci. Technol. **19**, 105601 (2008)

- **Bose-Einstein condensation of ^{87}Rb in a levitated crossed dipole trap**
  D. L. Jenkin, D. J. McCarron, M. P. Köppinger, H. W. Cho, S. A. Hopkins and S. L. Cornish
  Eur. Phys. J. D, published online 27$^{\text{th}}$ April 2011
  (DOI: 10.1140/epjd/e2011-10720-5)

- **A high phase-space density mixture of ^{87}Rb and ^{133}Cs: towards ultracold heteronuclear molecules**
  H. W. Cho, D. J. McCarron, D. L. Jenkin, M. P. Köppinger and S. L. Cornish
  Eur. Phys. J. D, published online 27$^{\text{th}}$ April 2011
  (DOI: 10.1140/epjd/e2011-10716-1)

- **Dual-Species Bose-Einstein Condensate of ^{87}Rb and ^{133}Cs**
  D. J. McCarron, H. W. Cho, D. L. Jenkin, M. P. Köppinger and S. L. Cornish
  Phys. Rev. A **84**, 011603 (2011)

Chapter 2

Basic Theory

The theory behind the production of and physics within ultracold dilute atomic gases has been extensively documented and reviewed in numerous publications, see for example [6–10, 13, 95, 96]. The aim of this chapter is to simply provide an introduction to the theoretical aspects relevant to the work presented in this thesis. More complete information on the subjects detailed in this chapter can be found in the publications referenced herein.

2.1 Ultracold Collisions

Collisions between ultracold atoms result in elastic or inelastic scattering. This scattering behaviour plays a key role in understanding the properties of ultracold atomic gases. Elastic collisions are crucial for rethermalisation and enable efficient evaporative and sympathetic cooling of atomic samples while inelastic collisions normally result in trap loss and heating. The complex scattering behaviour can be characterised by one parameter, the s-wave scattering length.

2.1.1 Elastic Collisions

For elastic collisions the total kinetic energy of the two colliding atoms does not change but the individual kinetic energies can change. The Hamiltonian

for the relative motion of two colliding atoms is

$$H = E_{\text{kin}} + V(r), \tag{2.1}$$

where E_{kin} denotes the relative kinetic energy of the atoms, $V(r)$ is the interaction potential and r is the distance between the atoms. As the scattering potential $V(r)$ is spherically symmetric the Hamiltonian can be decoupled into a radial part and a part depending on the angular momentum l [97]

$$H = -\frac{\hbar^2}{2m^*}\left[\frac{1}{r^2}\frac{d}{dr}\left(r^2\frac{d}{dr}\right) - \frac{l(l+1)}{r^2}\right] + V(r), \tag{2.2}$$

where m^* is the reduced mass and l denotes the quantum number of the orbital angular momentum. For $l \neq 0$ a centrifugal barrier is added to the long range attractive part of the potential. In the limit of $r \to \infty$ the solutions to the Schrödinger equation for this Hamiltonian have the form of an incoming plane wave and an outgoing spherical wave

$$\psi_k(r) = e^{ikr} + f(\mathbf{k})\frac{e^{ikr}}{r}. \tag{2.3}$$

Here $f(\mathbf{k})$ is the scattering amplitude and $\mathbf{k}$ is the wavevector of the scattered wave given by

$$k = \frac{m^*\langle v_R\rangle}{\hbar} = \left(\frac{16m^* k_{\text{B}}T}{\pi\hbar^2}\right)^{1/2}, \tag{2.4}$$

where m^* is the reduced mass and $\langle v_R\rangle$ is the mean relative velocity. The scattering cross-section is related to the scattering amplitude by

$$\sigma(\mathbf{k}) = \int |f(\mathbf{k})|^2 d\Omega. \tag{2.5}$$

Assuming that the interaction between atoms is spherically symmetric the scattering amplitude only depends on the scattering angle θ and can be written as

$$f(\theta) = \frac{1}{2ik}\sum_{l=0}^{\infty}(2l+1)(e^{i2\delta_l} - 1)P_l(\cos\theta). \tag{2.6}$$

Here l denotes the contribution from each orbital angular momentum to the total scattering amplitude, δ_l is the phase shift associated with each partial wave and $P_l(\cos\theta)$ are Legendre polynomials [98]. The total scattering cross-section is obtained using equations 2.5 and 2.6 and integrating over the full solid angle to obtain

$$\sigma(k, \delta_l) = \frac{4\pi}{k^2}\sum_{l=0}^{\infty}(2l+1)\sin^2\delta_l. \tag{2.7}$$

If the particles are bosons (fermions) the wavefunction ψ_k must be symmetric (antisymmetric) under interchange of the coordinates of the two particles. Exchanging the two particle coordinates corresponds to changing the sign of the relative coordinate, *i.e.* $\mathrm{r} \rightarrow -\mathrm{r}$, $\theta \rightarrow \pi - \theta$ and $\varphi \rightarrow \pi + \varphi$, where φ is the azimuthal angle. To calculate the scattering cross-section for indistinguishable particles the limits of the integral in equation 2.5 are reduced to half the full solid angle to avoid double counting. This results in a cross-section with twice the amplitude of classical particles

$$\sigma(k, \delta_l) = \frac{8\pi}{k^2} \sum_{l=0}^{\infty} (2l+1) \sin^2 \delta_l. \tag{2.8}$$

The $(-1)^l$ parity of the Legendre polynomials and the requirement that ψ_k be symmetric for identical bosons means that only even partial waves ($l = 0, 2, 4, ...$) can contribute to the total scattering cross-section. The reverse is true for fermions and the suppression of s-wave scattering makes quantum degeneracy impossible to achieve in pure single species Fermi gases. By adding a second species s-wave collisions can be introduced to fermionic systems and therefore allow Fermi degeneracy to be reached via sympathetic cooling with the second species [42]. Similarly the suppression of p-wave collisions in single species bosonic gases is removed when a second bosonic species is introduced. This is the case for a mixture of ^{87}Rb and ^{133}Cs as the two-species are distinguishable. This change results in a cross-section defined by equation 2.7 and allows p-wave collisions.

Low Energy Scattering

At low energies the centrifugal barrier for $l \neq 0$ in the long range attractive potential (equation 2.2) results in the scattering cross-section for bosons being dominated by the $l = 0$ term. If the relative kinetic energy of two atoms is less than the barrier height the atoms never achieve interparticle separations where $V(r)$ is non-negligible and scattering does not take place. Here scattering is due to pure s-wave collisions described by the elastic s-wave cross-section $\sigma(k, \delta_0)$ and the s-wave scattering length a

$$\sigma(k, \delta_0) = \frac{8\pi}{k^2} \sin^2 \delta_0 \quad \text{and} \quad a = -\lim_{k \rightarrow 0} \frac{\tan \delta_0}{k}. \tag{2.9}$$

Using the s-wave scattering length a and neglecting corrections for the effective range [99, 100] the elastic cross-section can be written in the form

$$\sigma_0 = \frac{8\pi a^2}{1 + k^2 a^2}. \tag{2.10}$$

This relation has two important results. In the limit of low energies, $ka \ll 1$, $\sigma = 8\pi a^2$ is independent of energy and equivalent to scattering from a hard sphere of radius a. This is called the ultracold limit. At higher energies or large values of the scattering length $ka \gg 1$. Here the cross-section reaches the unitarity limit where $\sigma = 8\pi/k^2$. The scattering cross-section now has a maximum value and is independent of the scattering length.

Higher Partial Waves

If the scattered atoms have a kinetic energy greater than the centrifugal potential barrier the approximation that only s-wave collisions contribute to the total scattering cross-section is no longer valid. The centrifugal potential is given by

$$V_{\text{rep}} = \frac{\hbar^2 l(l+1)}{2mr^2}, \tag{2.11}$$

therefore the minimum energy required for higher partial waves to contribute is given by

$$E_l = \frac{\hbar^2 l(l+1)}{2m^* R_{\text{min}}^2} - \frac{C_6}{R_{\text{min}}^6}. \tag{2.12}$$

Here m^* is the reduced mass, C_6 is the van-der-Waals coefficient and R_{min} is the radius at which the potential reaches a maximum value given by

$$R_{\text{min}}^2 = \left(\frac{6m^* C_6}{\hbar^2 l(l+1)} \right)^{1/2}. \tag{2.13}$$

The values of the van-der-Waals coefficients quoted in the literature are often given in atomic units. To convert these values into units of energy appropriate for equations 2.12 and 2.13 the C_6 coefficient must be multiplied by a_0^6 and the Hartree energy $E_h = \hbar^2/(m_e a_0^2)$ where m_e is the electron mass. The relevant scattering thresholds and C_6 coefficients for a ^{87}Rb - ^{133}Cs mixture are presented in table 2.1. This table shows that d-wave scattering occurs for collisional energies with $T \gtrsim 200$ μK. During this experiment the mixture temperature does not exceed 184(3) μK however it is likely that there is

	^{133}Cs -^{133}Cs	^{87}Rb -^{87}Rb	^{87}Rb -^{133}Cs
C_6	6851	4691	5284
p-wave	n/a	n/a	56 μK
d-wave	180 μK	410 μK	290 μK

Table 2.1: Van-der-Waals C_6 coefficients in atomic units with the corresponding p-wave and d-wave scattering thresholds for a ^{87}Rb -^{133}Cs mixture [101, 102].

still a d-wave contribution to the scattering cross-section as some collision energies will be greater than the d-wave threshold. This behaviour has been observed in previous work with a ^{87}Rb - ^{133}Cs mixture at ~ 7 μK [88]. Here interspecies p-wave Feshbach resonances were observed despite the mixture temperature being a factor of ~ 8 below the 56 μK p-wave threshold.

2.1.2 Behaviour of the Scattering Length

Free atoms have a wavefunction described by the de Broglie wavelength (equation 2.17). When two atoms collide the potential experienced (figure 2.1 (a)) increases the energy of the atom pair by that of the potential. This energy increase results in both the de Broglie wavelength and oscillation amplitude within the potential decreasing and gives rise to a phase shift of the free atom de Broglie wave. This phase shift determines the maximum distance at which free atoms begin to interact with each other and so governs the separation at which free atom de Broglie oscillations begin. This distance is known as the scattering length, a (figure 2.1 (b)).

Outside the region of interaction the wavefunction is $\psi_k(r) \propto \frac{1}{r}\sin(kr + \delta_0)$. For small r the interaction potential results in the wavefunction following $\psi_k(r) \simeq kr\cos(\delta_0) + \sin(\delta_0)$. This modified wavefunction approximates a straight line with a zero-crossing at $a = -\tan(\delta_0)/k$. Figures 2.1 (c), (d) and (e) highlight the asymptotic nature of the scattering wavefunction for negative, zero and positive scattering lengths respectively. The sign of the scattering length dictates the nature of the interactions in a quantum degenerate gas and is set by the position of the last bound state. For a real

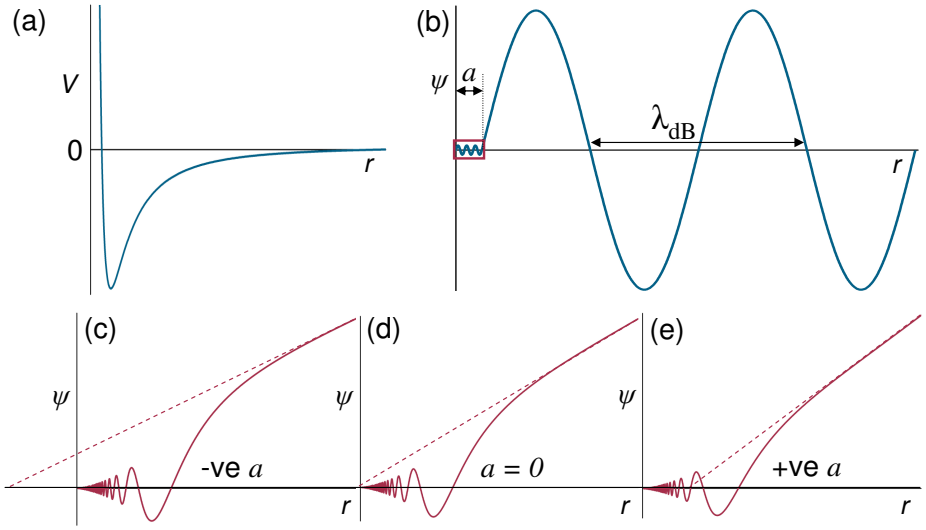

Figure 2.1: Schematic detailing the modification of the wavefunction for two colliding atoms due to an interaction potential. (a) The potential energy of the colliding atom pair V as a function of the separation r. (b) At short range (red box) the interaction potential results in a phase shift of the wavefunction. This changes the separation at which free atoms interact by an amount a called the scattering length. The zero-crossing of the asymptotic wavefunction gives the sign and magnitude of the scattering length. This value is highly dependent on the short range potential and can be (c) negative (d) zero or (e) positive.

bound state $a > 0$ while for a virtual bound state $a < 0$. When $a \neq 0$ the bounding condition of the wavefunction is changed. For positive scattering lengths the wavefunction is compressed and the energy is higher, therefore interactions are repulsive. Analogously a negative scattering length leads to a lower energy and attractive interactions.

2.1.3 Inelastic Collisions

Inelastic collisions change the atomic internal states during the scattering process provided there is a coupling between the states. To conserve energy and momentum a loss of internal energy results in a rise of the kinetic energy of the particles. This gain of kinetic energy is typically greater than the trap depth and results in trap loss. Inelastic losses can be separated into three

different categories: single particle loss, two-body loss and three-body loss.

Single particle loss removes atoms from the trapped sample through collisions with the background gas. Although not necessarily inelastic, these collisions do change the total kinetic energy of the trapped sample and at low densities limit the lifetime of a trapped gas. The rate of these collisions is independent of the atomic density meaning that this loss process does not lead to significant heating of the sample. Typical lifetimes in a well designed ultra-high vacuum (UHV) system due to this loss process are in excess of 100 s.

For inelastic two-body collisions the atoms internal states change. When in the lower hyperfine ground state this process occurs through dipolar angular momentum changing collisions only. Two specific mechanisms allow such dipolar collisions, direct spin-spin coupling and the second order spin-orbit interaction. The relative strengths of these two coupling processes increases with atomic mass due to the reduction of the energy level spacing and the spin-orbit interaction is stronger for heavier atoms due to relativistic electron velocities [97]. The spin-spin and second order spin-orbit interaction have opposite sign. For ^{87}Rb the two effects are almost equal in magnitude resulting in an anomalously low dipolar relaxation rate. For ^{133}Cs, with its higher atomic number, spin-orbit effects are larger and overwhelm the spin-spin contribution to give a dipolar relaxation rate $\simeq 50,000$ times greater than that for ^{87}Rb [103]. By preparing atoms in the lowest internal energy state (*e.g.* $F = 3, m_F = +3$ for ^{133}Cs) inelastic two-body losses can be avoided as atoms cannot relax into a state with lower energy [104].

A collision between three atoms can form a deeply bound molecule and a single atom. Energy and momentum conservation result in the molecule and atom carrying away 1/3 and 2/3 of the binding energy respectively. The binding energy released is typically much greater than the trap depth resulting in both the molecule and the atom escaping from the trap. The three body loss rate is proportional to the mean squared density, $\langle n^2 \rangle$, therefore this loss process occurs predominantly at the trap centre and causes the coldest atoms to be lost. This 'anti-evaporation' gives rise to heating in the trap and can make three-body collisions a significant hurdle to overcome during the final steps towards a quantum degenerate sample.

Accounting for the three inelastic loss mechanisms the evolution of the atom number is described using

$$\frac{dN}{dt} = -\alpha N - L_2 \int n^2 d^3r - L_3 \int n^3 d^3r, \tag{2.14}$$

where α is the background collision rate, L_2 and L_3 are the two- and three-body loss rate coefficients respectively, N is the particle number and n is the atomic density.

2.2 Feshbach Resonances

Since the first observation of a Feshbach resonance in an ultracold gas [105] these features have become an essential tool to control atomic interactions and have found a manifold of applications in this field [13]. This phenomena takes place when two atoms collide with energy E_c in an entrance channel and resonantly couple to a bound molecular state with energy $\Delta E(B)$ in a closed channel, figure 2.2 (a). The energy difference between the atomic and molecular states can be tuned via a magnetic field provided that the corresponding magnetic moments are different, figure 2.2 (b). The Feshbach resonance occurs when a bound molecular state crosses threshold of the open channel. As the molecular state approaches the atomic state the scattering length is highly sensitive to the magnetic field, figure 2.2 (c).

When the molecular state is above the entrance channel threshold a virtual bound state exists and the scattering length is negative. As the bound state moves down in energy towards threshold the negative scattering length becomes larger and ultimately goes to infinity when the bound state passes through the collision threshold. Beyond this point there is a real bound state just below threshold corresponding to a large positive scattering length. This corresponds to adding a new node to the wavefunction, see figure 2.1. As the real molecular state becomes more deeply bound the positive scattering length decreases in magnitude and approaches the background scattering length, a_{bg}, which is the scattering length far from resonance. This feature in the scattering length is described as a magnetic Feshbach resonance, here the scattering length a can be described as a function of the magnetic field

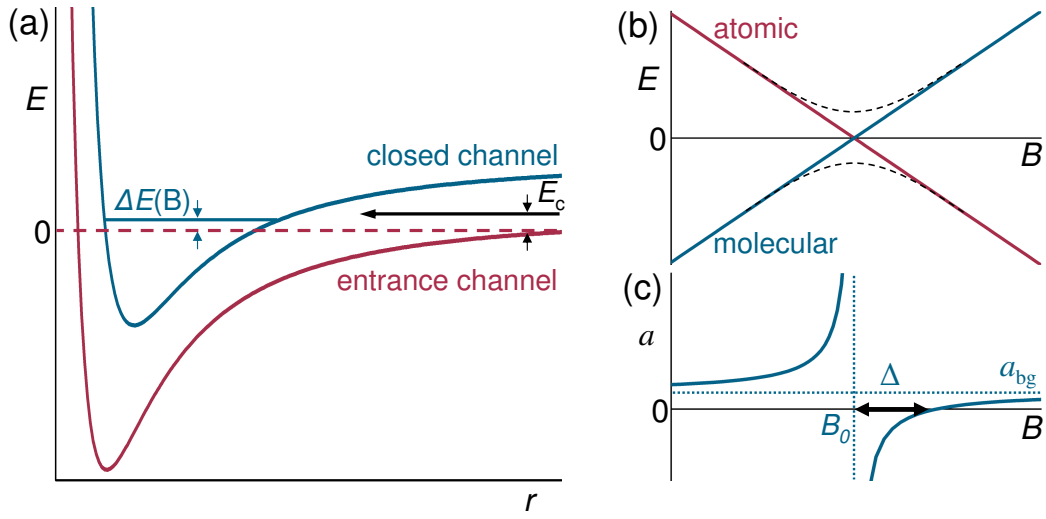

Figure 2.2: Schematic of a Feshbach resonance. (a) Two atoms colliding in the entrance channel (red curve) with an energy E_c can resonantly couple to a molecular bound state in a closed channel (blue curve) with energy $\Delta E(B)$. For ultracold atoms $E_c \to 0$ so resonant coupling occurs when $\Delta E(B)$ approaches the open channel threshold. (b) The energies of the atomic continuum (red line) and molecular bound state (blue line) can be tuned with a magnetic field and coincide at the resonance position B_0. Coupling leads to an avoided crossing between the atomic and molecular states (black dashed lines). Note that above the scattering continuum the molecules are unstable and rapidly dissociate into atoms. (c) Near the Feshbach resonance the scattering length is very sensitive to the magnetic field, becoming $\pm\infty$ at B_0.

B using [106]

$$a(B) = a_{\mathrm{bg}}\left(1 - \frac{\Delta}{B - B_0}\right). \tag{2.15}$$

The parameter Δ is the resonance width and B_0 denotes the resonance position where the scattering length diverges $a \to \pm\infty$. The zero-crossing of the scattering length associated with the Feshbach resonance occurs at a magnetic field of $B_0 + \Delta$, figure 2.2 (c). The divergence of the scattering length at a Feshbach resonance and the a^4 scaling of the three-body loss rate [107] lead to a dramatic enhancement of inelastic three-body losses from the trap when a Feshbach resonance is encountered. This enhanced loss is used to measure the locations of Feshbach resonances in ultracold gases, see section 6.8.

As Feshbach resonances offer the possibility to adjust the scattering length the interatomic interactions can be controlled. This valuable degree of freedom provides experimentalists with further control over experimental conditions. Examples of this control include the optimisation of evaporative cooling by varying the elastic collision cross-section and the tuning of the mean-field interaction in a BEC, see section 6.4.

Coupling between atomic and molecular states can also occur by tuning the scattering length via the application of radio-frequencies, oscillating magnetic fields [13] or optical fields [108]. The field of ultracold tunable gases has also led to the observation of and experiments involving intriguing resonance features between three free atoms and weakly bound trimer states referred to as Efimov quantum states [80, 109].

2.2.1 Magneto-association

The coupling between the atomic and molecular states at a Feshbach resonance leads to an avoided crossing being formed, black dashed lines in figure 2.2 (b). By adiabatically ramping the magnetic field across such an avoided crossing colliding atom pairs can be associated into Feshbach molecules [74]. This magneto-association only works for real molecular bound states ($\Delta E(B) < 0$) *i.e.* for the example in figure 2.2 (c) ramping the field from high to low values. Above the scattering continuum ($E = 0$) the molecules are unstable and rapidly dissociate into atoms. Below threshold coupling between molecular bound states leads to avoided crossings in the molecular energy spectrum [110]. A careful choice of magnetic field ramps can be used to navigate this spectrum to tune the character of the Feshbach molecule. The binding energies of these Feshbach molecules is extremely low and the molecules are very large, of the order of the scattering length. Inelastic atom-molecule and molecule-molecule collisions severely limit the trap lifetime of bosonic Feshbach molecules to several milliseconds [111]. Feshbach molecules created in three dimensional optical lattices have greatly enhanced lifetimes as individual molecules are isolated at single lattice sites [112]. The challenge to efficiently transfer these highly excited ultracold molecules into the rovibrational ground state is currently an area of ongoing research [53, 72, 73].

Early experiments that created molecules via magneto-association detected the molecules by means of RF-induced [113] or laser-induced [114] dissociation. However the molecular samples were not spatially separated from the atoms meaning that the Feshbach molecules could not be directly imaged or analysed. Pure molecular quantum gases are created by applying Stern-Gerlach separation immediately after the Feshbach sweep [79] and allow the molecular cloud to be directly monitored, see section 6.5.

2.3 Bose-Einstein Condensation

The phenomena of Bose-Einstein condensation (BEC) was first predicted by Bose [115] and Einstein [116] in 1924 and can be derived from quantum mechanical statistics. Here an ensemble of identical bosons occupy the lowest energy quantum state forming a coherent matter wave. This strikingly reveals the wave nature of matter and allows quantum behaviour to be demonstrated on a macroscopic scale. This was first experimentally realised in 1995 [3–5] thanks to advances in both laser cooling [6–8] and evaporative cooling in conservative traps [2].

2.3.1 Origin of BEC

Basic theory

The criteria for Bose-Einstein condensation is presented in figure 2.3. The Heisenberg uncertainty principle states that

$$\Delta x \Delta p \geq \frac{\hbar}{2} \tag{2.16}$$

where Δx (Δp) is the uncertainty in position (momentum). A high temperature (high velocity) results in the atom's positions being well defined (figure 2.3(a)). As the atoms are cooled the uncertainty in position increases and the atoms are better described as wave packets (figure 2.3(b)) with a thermal de Broglie wavelength

$$\lambda_{\mathrm{dB}} = \sqrt{\frac{2\pi\hbar^2}{m k_{\mathrm{B}} T}}, \tag{2.17}$$

where m is the mass of the particles and T is the temperature. Equation 2.17 shows that the extent of each wave packet is determined by the temperature. The number of particles contained in a volume equal to the cube of the thermal de Broglie wavelength is known as the phase-space density

$$\rho = n_0 \lambda_{\mathrm{dB}}^3, \tag{2.18}$$

with n_0 being the peak density in the sample. As the ensemble is cooled further individual wavefunctions begin to overlap (figure 2.3(c)) and at a critical temperature, T_c, collapse into the lowest energy quantum state forming a Bose-Einstein condensate when $\rho \sim 1$.

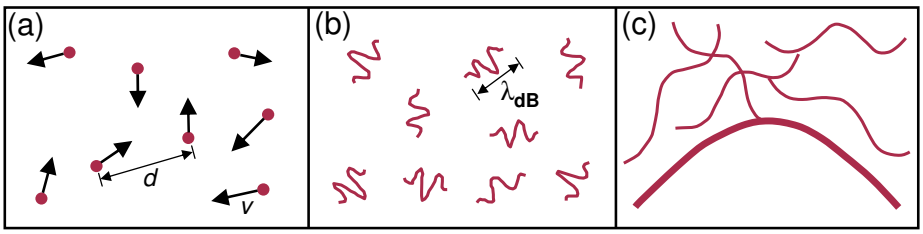

Figure 2.3: An illustration of the phase transition to BEC. (a) At high temperatures ($\gg T_\mathrm{c}$) the atomic separation, d, is much greater than their size and the atoms behave as point-like objects. (b) As the atoms are cooled the de Broglie wavelength, λ_{dB}, increases and the wave-like nature of the atoms increases. (c) When $T = T_\mathrm{c}$ the atomic wave packets begin to overlap ($\lambda_{\mathrm{dB}} \approx d$) and form a coherent matter wave.

A Quantum Statistical Approach

For an ideal Bose gas in thermal equilibrium the occupation number of an atomic state i with energy ε_i is given by [97]

$$N_i = \frac{1}{e^{(\varepsilon_i - \mu)/k_\mathrm{B}T} - 1}, \tag{2.19}$$

where μ is the chemical potential governed by the total number of atoms, $N = \sum_i N_i$. At high temperatures many different states are populated and for a given state the occupation number $N_i \ll 1$, this implies that $\varepsilon_i \gg \mu$. Equation 2.19 also provides the physical constraint $\varepsilon_0 > \mu$ as a chemical potential

equal to the energy of the ground state, ε_0, would lead to a negative or diverging occupation number. It is this mechanism that leads to Bose-Einstein condensation. To avoid the atom number in the ground state diverging the total atom number is split into two parts: N_0 the occupation number in the ground state and $N_{\rm th}$ the sum over all other states often referred to as the thermal component,

$$N = N_0 + N_{\rm th} = N_0 + \sum_{i=1}^{\infty} \frac{1}{e^{(\varepsilon_i - \mu)/k_{\rm B}T} - 1}. \tag{2.20}$$

A change in temperature implies a change in μ in order for the total atom number to be conserved. Specifically when the atom temperature is decreased, μ has to increase in value. Consider $N_{\rm th}$ as the atoms are cooled and therefore $\mu \to \varepsilon_0$. At a certain temperature $N_{\rm th}$ drops far below N, this is called the critical temperature $T_{\rm c}$. In order for the total atom number to be conserved these 'missing' atoms must be in the ground state. This macroscopic occupation of the ground state marks the onset of Bose-Einstein condensation. If the temperature continues to decrease below $T_{\rm c}$ the occupation number in the ground state increases until $N_0 = N$ and a pure Bose-Einstein condensate remains with no thermal component present.

2.3.2 A Bose Gas in a Harmonic Trap

The conservative traps used to confine the ultracold atoms in this work create potentials, $U(\mathbf{r})$, that can be approximated as harmonic

$$U(\mathbf{r}) = \frac{1}{2} m(\omega_x^2 x^2 + \omega_y^2 y^2 + \omega_z^2 z^2). \tag{2.21}$$

In such harmonic trapping potentials the conditions for Bose-Einstein condensation can be calculated. For a gas trapped in 3D the critical temperature is given by [117]

$$T_{\rm c} = \frac{\hbar \omega_{\rm ho}}{k_{\rm B}} \left(\frac{N}{1.202} \right)^{1/3} \tag{2.22}$$

with N the number of atoms and $\omega_{\rm ho} = (\omega_x \omega_y \omega_z)^{1/3}$ the geometric mean of the harmonic trap frequencies. The peak atomic density, n_0, in the trap is given by dividing the number of atoms by the effective volume V_E

$$n_0 = N/V_E = N\omega_{\rm ho}^3 \left(\frac{m}{2\pi k_{\rm B} T} \right)^{3/2}, \tag{2.23}$$

where the effective volume $V_E = \int \exp\left(\frac{-U(\mathbf{r})}{k_\mathrm{B}T}\right) d^3r$. Equations 2.17 and 2.23 can then be used to express the phase-space density defined by equation 2.18 as

$$\rho = N\left(\frac{\hbar\omega_\mathrm{ho}}{k_\mathrm{B}T}\right)^3. \tag{2.24}$$

At temperatures close to or below T_c a semi-classical approximation is used to calculate n_th, the density of the thermal bosons in the trap [96]

$$n_\mathrm{th}(\mathbf{r}) = \frac{g_{3/2}}{\lambda_\mathrm{dB}^3 \mathrm{e}^{(U(\mathbf{r})/k_\mathrm{B}T)}} \quad \text{for} \quad T \lesssim T_\mathrm{c}, \tag{2.25}$$

with the corresponding peak density $n_0 = n_\mathrm{th}(\mathbf{r} = 0)$. The function $g_{3/2}$ is of the form $g_\alpha(z) = \sum_{n=1}^{\infty} z^n/n^\alpha$ [118]. In free space the critical phase-space density is $\rho_c \simeq 2.612$ [96], a strikingly similar result to $\rho_c \sim 1$ given by the simple model in 2.3.1.

By integrating equation 2.25 over space it is possible to obtain an expression for how the condensate fraction varies with temperature

$$N_0/N = 1 - \left(\frac{T}{T_\mathrm{c}}\right)^3. \tag{2.26}$$

All calculations in this section have neglected atom-atom interactions within the BEC. However corrections for these interactions are typically of the order of just a few percent [97].

An Ideal Bose-Einstein Condensate

By neglecting atom-atom interactions the BEC behaves as an ideal gas with all atoms occupying the ground state of the harmonic potential $U(\mathbf{r})$. This case is accurately described by the ground state wavefunction of a three-dimensional harmonic trap given by

$$\phi_0(\mathbf{r}) = \left(\frac{m\omega_\mathrm{ho}}{\pi\hbar}\right)^{3/4} \exp\left(-\frac{m}{2\hbar}(\omega_x x^2 + \omega_y y^2 + \omega_z z^2)\right). \tag{2.27}$$

The density distribution of the ground state $n(\mathbf{r}) = N|\phi_0(\mathbf{r})|^2$ has a Gaussian profile and grows linearly with N. In contrast, the size of the condensed cloud is independent of N and is determined by the harmonic oscillator length

$$a_\mathrm{ho} = \sqrt{\frac{\hbar}{m\omega_\mathrm{ho}}}, \tag{2.28}$$

which is the average width of the Gaussian in equation 2.27. The individual condensate widths $\sigma_i = a_{\mathrm{ho,i}} = \sqrt{\hbar/(m\omega_i)}$, where $i = x, y, z$ can then be used to determine the momentum spread using the Heisenberg uncertainty principle

$$\sigma_{p,i} = \frac{\hbar}{\sigma_i} = \frac{\hbar}{a_{\mathrm{ho,i}}} = \sqrt{\hbar m \omega_i}. \tag{2.29}$$

By using $E_{\mathrm{rel}} = \frac{p^2}{2m}$ the average release energy for a non-interacting condensate can be calculated and is independent of N

$$E_{\mathrm{rel}} = \frac{1}{2}\hbar(\omega_x + \omega_y + \omega_z). \tag{2.30}$$

Bogoliubov Approximation

The properties of condensates consisting of interacting particles can be calculated using a many body Hamiltonian for N particles in an external potential. However this method becomes impractical for systems with large N. To solve this problem a mean field description for dilute Bose gases was proposed by Bogoliubov [119]

$$\hat{\Psi}(\mathbf{r}, t) = \Phi(\mathbf{r}, t) + \hat{\Psi}'(\mathbf{r}, t). \tag{2.31}$$

Here the field operator $\hat{\Psi}(\mathbf{r}, t)$ is split into the complex function $\Phi(\mathbf{r}, t)$, defined as the expectation value of the field operator $\Phi(\mathbf{r}, t) = \langle\hat{\Psi}(\mathbf{r}, t)\rangle$, and a first order perturbation term $\hat{\Psi}'(\mathbf{r}, t)$. The term $\Phi(\mathbf{r}, t)$ is often referred to as the condensate wavefunction while the BEC density distribution is given by $n(\mathbf{r}, t) = |\Phi(\mathbf{r}, t)|^2$.

Gross-Pitaevskii Equation

In dilute and cold gases binary collisions form the main contribution to particle interactions. The condition for such a weakly interacting system is $\langle n\rangle|a|^3 \ll 1$, with $\langle n\rangle$ being the mean atomic density and a being the s-wave scattering length. This simplification allowed both Gross [120] and Pitaevskii [121] to replace the interaction potential between the particles with an effective interaction potential

$$V(\mathbf{r} - \mathbf{r'}) = g\delta(\mathbf{r} - \mathbf{r'}) \quad \text{with} \quad g = \frac{4\pi\hbar^2 a}{m}. \tag{2.32}$$

For $T \ll T_c$ the term $\hat{\Psi}'$ in equation 2.31 can be neglected and so $\hat{\Psi}$ can be replaced by Φ. Writing Φ as $\psi(\mathbf{r},t)e^{-i\mu t/\hbar}$ yields a time independent Gross-Pitaevskii equation (GPE)

$$\left[-\frac{\hbar^2\nabla^2}{2m} + V(\mathbf{r}) + g|\psi(\mathbf{r})|^2\right]\psi(\mathbf{r}) = \mu\psi(\mathbf{r}). \tag{2.33}$$

This has the form of a non-linear Schrödinger equation due to the $|\psi(\mathbf{r})|^2$ interaction term and is reduced to the usual Schrödinger equation when there are no interactions, $g = 0$.

In the ground state the energy is a function of the density only and can be written in the form [96]

$$E[n] = \int d\mathbf{r}\left[\frac{\hbar^2}{2m}|\nabla\sqrt{n}|^2 + nV(\mathbf{r}) + \frac{gn^2}{2}\right] = E_{\text{kin}} + E_{\text{ho}} + E_{\text{int}}. \tag{2.34}$$

The first term, E_{kin}, is derived from the uncertainty principle and corresponds to the quantum kinetic energy. It is usually referred to as 'quantum pressure'. The harmonic oscillator energy, E_{ho}, is the potential energy in the system and the mean field energy, E_{int}, arises from the interactions between particles. By directly integrating equation 2.33 the chemical potential can be expressed in terms of the different energy contributions

$$\mu = \frac{E_{\text{kin}} + E_{\text{ho}} + 2E_{\text{int}}}{N}. \tag{2.35}$$

Taking the sum over the three directions derives the virial relation

$$2E_{\text{kin}} - 2E_{\text{ho}} + 3E_{\text{int}} = 0. \tag{2.36}$$

The release energy of a BEC can be measured by rapidly switching off the trapping potential and integrating over the velocity distribution observed through absorption imaging. During the first phase of expansion both the quantum kinetic energy and interaction energy are rapidly converted into expansion energy

$$E_{\text{rel}} = E_{\text{kin}} + E_{\text{int}}. \tag{2.37}$$

2.3.3 The Thomas-Fermi Approximation

Atom-atom interactions influence many properties of condensates and are well described by a self-interaction energy, E_{int}, in a mean-field model this

depends only on the density of the condensate, n, and the s-wave scattering length, a. To estimate the effect of interatomic interactions the following useful expression is used [96]

$$\frac{E_{\text{int}}}{E_{\text{kin}}} = \frac{N|a|}{a_{\text{ho}}}. \tag{2.38}$$

For sufficiently large condensates this ratio is much larger than one and allows the ground state energy to be obtained by neglecting the kinetic energy term, E_{kin}, in the GPE equation (equation 2.33). This is called the Thomas-Fermi approximation. Since $|\psi|^2 = n(\mathbf{r})$ the following expression is then derived from equation 2.33

$$n(\mathbf{r}) = \begin{cases} \frac{\mu - V(\mathbf{r})}{g} & \text{for } \mu - V(\mathbf{r}) > 0, \\ 0 & \text{otherwise.} \end{cases} \tag{2.39}$$

The atomic density reflects the shape of the potential, *e.g.* for a harmonic potential the density would be an inverted parabola. The density vanishes at the classic turning points where $\mu = V(\mathbf{r})$ defined as the Thomas Fermi radii

$$R_{\text{TFi}} = \sqrt{\frac{2\mu}{m\omega_i^2}} = a_{\text{ho}} \frac{\omega_{\text{ho}}}{\omega_i} \left(\frac{15Na}{a_{\text{ho}}} \right)^{1/5}, \tag{2.40}$$

where $i = x, y, z$ marks the axis with trap frequency ω_i. By inserting $V(\mathbf{r} = 0) = 0$ into equation 2.39 the peak density at the trap centre can be calculated

$$n_0 = \frac{\mu}{g} = \frac{\mu m}{4\pi\hbar^2 a} \tag{2.41}$$

The normalisation condition on $n(\mathbf{r})$ then provides an equation linking the chemical potential and the number of particles

$$\mu = \frac{\hbar\omega_{\text{ho}}}{2} \left(\frac{15Na}{a_{\text{ho}}} \right)^{2/5} \tag{2.42}$$

By neglecting the quantum kinetic energy the release energy (equation 2.37) depends only on the interaction energy, E_{int}. Again, by integrating over the density distribution (equation 2.34) the average energy and release energy in the Thomas-Fermi approximation can be calculated

$$E = \frac{5}{7}\mu \quad \text{and} \quad E_{\text{rel}} = \frac{2}{7}\mu, \quad \text{respectively.} \tag{2.43}$$

Several experiments have demonstrated the dependence of the release energy with the atom number in the condensate [122, 123] and the scattering length [124].

2.3.4 Tunable Interactions

The energies calculated in equation 2.43 describe a condensate in equilibrium. For the majority of BEC experiments these equations are always valid as the scattering length is determined by the choice of atom and fixed from the outset. However for specific alkali atoms such as ^{133}Cs and ^{85}Rb, magnetically induced Feshbach resonances allow the scattering length to be tuned to control atom-atom interactions within the condensate [11, 12]. When the scattering length is changed adiabatically ($\dot{R}_{\mathrm{TFi}}/R_{\mathrm{TFi}} \ll \omega_i$) the density distribution will evolve in time and equations 2.43 are valid, therefore the release energy per particle scales with $a^{2/5}$ [124].

In contrast, fast non-adiabatic changes in the scattering length from the equilibrium value a to a new value a' alter the interaction energy between particles according to a'. In contrast, the density distribution does not have sufficient time to evolve and is determined by a. This results in the release energy per particle being modified using equations 2.41 and 2.43

$$E_{\mathrm{rel}}(a') = \frac{2}{7} n_0(a) g(a') = \frac{2}{7} \mu(a) \frac{a'}{a}. \tag{2.44}$$

For non-adiabatic changes in the scattering length the release energy per particle scales linearly with a' [124].

When $a > 0$ repulsive interactions produce stable condensates with a strong mean-field expansion and a size determined by the interaction energy. In contrast, when $a < 0$ interactions are attractive and the gas density increases at the trap centre to reduce the interaction energy. These attractive forces can be countered by the quantum kinetic energy which also increases with the gas density. However, the different scaling of E_{int} and E_{kin} with the particle number results in stable condensates only forming with an atom number limited to a small critical value, N_{cr}, determined by [20, 125]

$$N_{\mathrm{cr}} = k^* \frac{a_{\mathrm{ho}}}{|a|}, \tag{2.45}$$

where k^* is a dimensionless constant called the stability coefficient. The exact value of k^* is determined by the ratio of the trap frequencies. When $N > N_{\mathrm{cr}}$ the condensate is unstable and the density increases at the trap centre until inelastic losses become dominant and reduce N to be below N_{cr}.

For tunable quantum gases large stable condensates can initially be made at positive scattering lengths. When the scattering length is quickly changed to a negative value the nature of interactions in the condensate are suddenly changed from repulsive to attractive. Now the condensate collapses [126] resulting in a substantial loss of atoms and a large momentum spread. The resemblance of this collapse (on an immensely lower energy scale) to a supernova has led to this process being referred to as a 'Bosenova'.

Finally when $a = 0$ the condensate is essentially non-interacting with minimum internal energy. By switching off the self-interaction between atoms the cloud expansion is minimal and a 'frozen' condensate is realised.

2.3.5 Condensate Expansion

When a condensate is released from the trapping potential the internal energy (mean-field energy) is converted to kinetic energy in an anisotropic way. The accelerating force due to the internal mean field energy is proportional to the gradient of the mean field energy and therefore proportional to the density gradient [96]. For cigar shaped condensates released from an anisotropic confining potential, where the radial trap frequency $\omega_\rho > \omega_z$, the axial trap frequency, the acceleration in the radial direction is larger than that in the axial direction. This results in the aspect ratio of a freely expanding condensate inverting, an important signature of BEC [127].

For a condensate released from an axially symmetric trap the Thomas-Fermi radii in the radial (ρ) and axial (z) directions evolve during the free expansion according to

$$R_{\rho,z}(t) = \lambda_{\rho,z}(t) R_{\rho,z}(0). \tag{2.46}$$

The initial size $R_{\rho,z}(0)$ can be calculated using equation 2.40. For the case of a sudden and total opening of the trap at $t = 0$ the evolution of the scaling parameters, λ_ρ and λ_z, is described by [127]

$$\begin{aligned} \frac{d^2}{d\tau^2}\lambda_\rho &= \frac{1}{\lambda_\rho^3 \lambda_z}, \\ \frac{d^2}{d\tau^2}\lambda_z &= \frac{\epsilon^2}{\lambda_\rho^2 \lambda_z^2}, \end{aligned} \tag{2.47}$$

here $\tau = \omega_\rho t$ and $\epsilon = \omega_z/\omega_\rho$. Equations 2.47 only apply when $\epsilon \ll 1$.

In contrast to condensates, thermal clouds undergo isotropic expansion when released from a trap. The width of a thermal cloud, $\sigma_{\rho,z}$, dropped from a harmonic trap is given by

$$\sigma_{\rho,z}^2 = \frac{k_\mathrm{B}T}{m}\left(\frac{1}{\omega_{\rho,z}^2} + t^2\right), \tag{2.48}$$

where T is the cloud temperature and m is the atomic mass. This equation shows that the trap frequencies govern the initial cloud size in the trap but the temperature dictates the rate of expansion of the cloud after release. For long times-of-flight the aspect ratio of the thermal cloud does not depend on the trap frequencies and $\sigma_\rho/\sigma_z \to 1$. Experimental data on the expansion of condensates and thermal atoms are presented in section 5.4.

2.4 Quantum Degenerate Mixtures

Quantum degenerate mixtures [27–38] of atomic gases are currently the subject of intensive research, exhibiting rich physics inaccessible in single species experiments. To accurately describe a two-species degenerate mixture a pair of coupled Gross-Pitaevskii equations are required with an additional nonlinear term which represents interspecies interactions [128, 129]

$$\left[-\frac{\hbar^2}{2m_1}\nabla^2 + V_1(\mathbf{r}) + g_{11}|\psi_1(\mathbf{r})|^2 + g_{12}|\psi_2(\mathbf{r})|^2\right]\psi_1(\mathbf{r}) = \mu_1\psi_1(\mathbf{r}), \tag{2.49}$$

$$\left[-\frac{\hbar^2}{2m_2}\nabla^2 + V_2(\mathbf{r}) + g_{21}|\psi_1(\mathbf{r})|^2 + g_{22}|\psi_2(\mathbf{r})|^2\right]\psi_2(\mathbf{r}) = \mu_2\psi_2(\mathbf{r}). \tag{2.50}$$

Here $\psi_1(\mathbf{r})$ ($\psi_2(\mathbf{r})$) is the wavefunction for species 1 (2) with mass m_1 (m_2) and chemical potential μ_1 (μ_2). As in most BEC systems, the atomic interaction energies dominate these equations. The single species interactions are governed by the terms $g_{11}|\psi_1(\mathbf{r})|^2$ and $g_{22}|\psi_2(\mathbf{r})|^2$ while the interspecies interactions are encompassed in the additional $g_{12}|\psi_2(\mathbf{r})|^2$ and $g_{21}|\psi_1(\mathbf{r})|^2$ terms. The interaction coupling constants are defined as

$$g_{11} = \frac{4\pi\hbar^2 a_{11}}{m_1}, \quad g_{22} = \frac{4\pi\hbar^2 a_{22}}{m_2} \quad \text{and} \tag{2.51}$$

$$g_{12} = g_{21} = 2\pi\hbar^2 a_{12}\left(\frac{m_1 + m_2}{m_1 m_2}\right) \tag{2.52}$$

with the single species scattering lengths a_{11} and a_{22} and the interspecies scattering length a_{12} [129]. The behaviour of the mixture is determined by the relative strengths of the single species and interspecies interactions and can be characterised by the interaction parameter Δ,

$$\Delta = \frac{g_{12}}{\sqrt{g_{11}g_{22}}} = \frac{a_{12}}{\sqrt{a_{11}a_{22}}}\sqrt{\frac{(m_1 + m_2)^2}{4m_1 m_2}} \simeq \frac{a_{12}}{\sqrt{a_{11}a_{22}}}. \tag{2.53}$$

For a ^{87}Rb - ^{133}Cs mixture this ratio reduces to be essentially dependent only on the scattering lengths and reveals three distinct regimes for an interacting dual-species BEC highlighted in figure 2.4 [129]. Implicit in this discussion is the assumption that both single species scattering lengths are positive. When $\Delta < -1$ the mixture is miscible and becomes unstable against collapse as the attractive interspecies interactions overwhelm the individual repulsive terms (figure 2.4(a)). When $|\Delta| < 1$ the single species interactions dominate and the mixture is stable and miscible (figure 2.4(b)). When $\Delta > 1$ the dominant repulsive interspecies interactions lead to a phase separation of the two components (figure 2.4(c)). This phase separation is a particularly dramatic

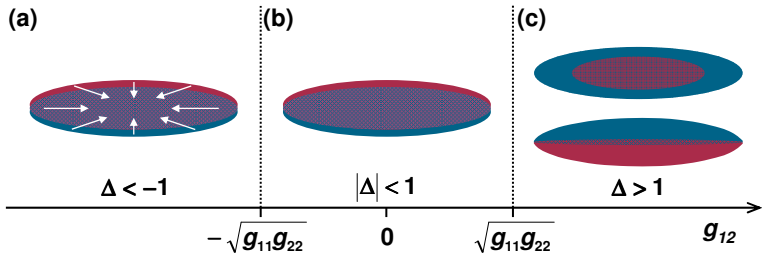

Figure 2.4: Characteristics of a dual-species BEC as a function of the interaction parameter $\Delta = g_{12}/\sqrt{g_{11}g_{22}}$. (a) For $\Delta < -1$ the mixture is miscible but unstable against collapse. (b) If $|\Delta| < 1$ the system is stable and miscible and consists of interpenetrating superfluids. (c) When $\Delta > 1$ the mixture is stable but immiscible and the two components phase separate.

example of the rich physics accessible to quantum degenerate mixtures and has been demonstrated in several experiments [28, 34–36].

The ability to independently control the value of either of the single species scattering lengths, or the interspecies scattering length, allows the relative

strengths of interactions and therefore the miscibility to be tuned across these three regimes. The contrasting behaviour of the ^{87}Rb and ^{133}Cs scattering lengths (figure 1.1) and the numerous interspecies Feshbach resonances [88] potentially make tunable interactions possible in a ^{87}Rb - ^{133}Cs mixture. Such tunable miscibility has already been demonstrated in a degenerate mixture of ^{87}Rb and ^{85}Rb by exploiting a Feshbach resonance in ^{85}Rb [36].

2.5 Magnetic Trapping

When an atom is in the presence of a magnetic field the degeneracy of the Zeeman sublevels is lifted. For the $^2S_{1/2}$ ground states of the alkalis, the energy shift is described exactly by the Breit-Rabi formula

$$\Delta E = -\frac{h\Delta\nu}{2(2I+1)} - g_I\mu_B B m_F \pm \frac{1}{2}h\Delta\nu\left(1 + \frac{4m_F}{2I+1}x + x^2\right)^{1/2}, \quad (2.54)$$

where $\Delta\nu$ is the hyperfine splitting of the ground states at zero B-field and

$$x = \frac{(g_I + g_J)\mu_B B}{h\Delta\nu}. \quad (2.55)$$

For 'low' bias fields the energy shift is approximated by

$$\Delta E = m_F g_F \mu_B B, \quad (2.56)$$

where g_F is the Landé g-factor and μ_B is the Bohr magneton [130]. Hence for low bias fields the energy of the m_F sublevels varies linearly with increasing B-field. Atoms with $m_F g_F > 0$ are called 'low field seekers' and can be trapped at a local magnetic field minimum. Atoms with $m_F g_F < 0$ are called 'high field seekers' and cannot be confined with magnetic fields alone. At 'high' bias fields coupling between the applied magnetic field and the individual magnetic moments dominates that between the total nuclear magnetic and electronic magnetic moments [131]. For this case the energy shift is approximated by

$$\Delta E = m_J g_J \mu_B B - m_I g_I \mu_B B. \quad (2.57)$$

Figures 2.5 and 2.6 show the magnetic field dependent energy shifts of the hyperfine ground states of ^{87}Rb and ^{133}Cs respectively. This behaviour can

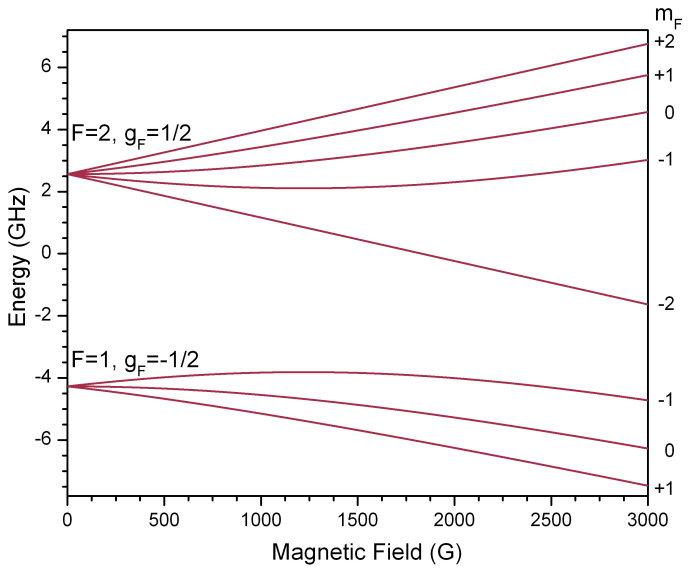

Figure 2.5: Breit-Rabi diagram showing the magnetic field dependent energy shifts of the hyperfine ground states in ^{87}Rb .

result in atomic states being magnetically trappable at low B-fields but not trappable at high B-fields and vice versa. This change in character is shown in figure 2.5 for the $|1,-1\rangle$ ^{87}Rb state at $B \simeq 1200$ G and in figure 2.6 for the $|3,-3\rangle$ ^{133}Cs state at $B \simeq 2500$ G.

The magnetic trap used in this experiment is a simple magnetic quadrupole potential formed by the pair of anti-Helmholtz coils, Quad 1 (figure 3.12). The quadrupole potential is described by

$$B = C(\rho^2 + 4z^2)^{1/2}, \tag{2.58}$$

where $\rho^2 = x^2 + y^2$ and $C = m_F g_F \mu_B \left|\frac{\partial B}{\partial \rho}\right|$ is the trap constant. The linear potential produced by the Quad 1 coils has an axial gradient of 1.001(7) G/cm/A and offers tight atomic confinement making efficient evaporative cooling possible. This, coupled with its simplicity and excellent optical access, makes the magnetic quadrupole trap an attractive option to many experimentalists. However, the presence of the zero field at the trap centre allows the coldest atoms to undergo Majorana 'spin flip' transitions and prevents quantum degeneracy from being reached in this simple magnetic trap.

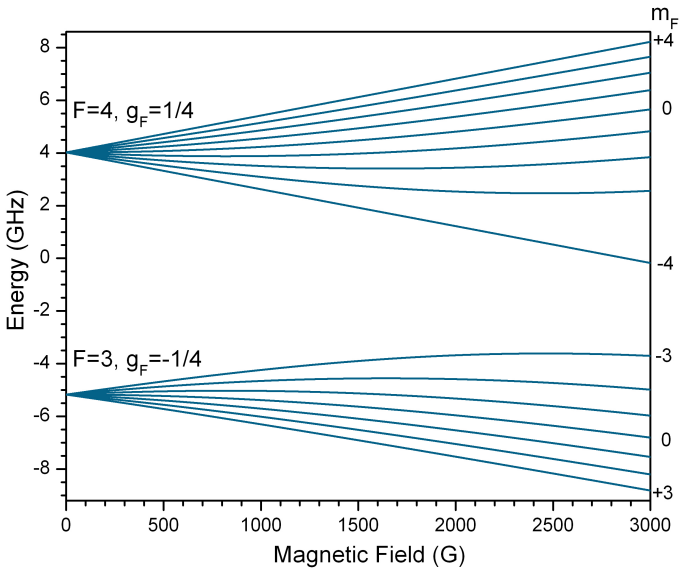

Figure 2.6: Breit-Rabi diagram showing the magnetic field dependent energy shifts of the hyperfine ground states in ^{133}Cs.

2.5.1 Majorana Transitions

The magnetic moment, μ, of an atom in a magnetic field of magnitude B precesses about the magnetic quantisation axis at the Larmor frequency

$$\omega_{\text{Larmor}} = \frac{\mu B}{\hbar}. \tag{2.59}$$

In order for the atom to remain trapped the magnetic moment must follow the magnetic field adiabatically. In low field regions near the centre of the quadrupole trap the rate of change of the magnetic field becomes comparable to the Larmor frequency. Here the magnetic moment can no longer follow the field and the atom may flip its spin into an untrapped or an anti-trapped state thus being lost from the trap. As these Majorana transitions occur at the centre of the quadrupole potential the coldest atoms are lost, leading to this process causing both loss and heating. A simple argument presented in [132] allows the Majorana loss rate to be estimated as

$$\Gamma_{\text{maj.}} = 1.85\frac{\hbar}{m}\left(\frac{C}{k_{\text{B}}T}\right)^2. \tag{2.60}$$

This estimate assumes thermal equilibrium and so is independent of elastic collision rate [133]. Majorana losses can be slightly mitigated by adiabatically expanding the trap, since the temperature scales more weakly than the field

gradient, T $\propto \left(\frac{\partial B}{\partial \rho}\right)^{2/3}$. So weakening the trap will decrease the loss rate but at the expense of a lower elastic collision rate.

2.5.2 Magnetic Levitation

In order for an atom to be exactly levitated against gravity the force due to the magnetic gradient must equal and oppose the gravitational force on the atoms

$$F_z = \mu \left| \frac{\partial B}{\partial z}_{\text{lev.}} \right| - mg = 0. \tag{2.61}$$

The magnetic field gradients required to levitate ground state ^{87}Rb and ^{133}Cs atoms with no bias field present are summarised in tables 2.2 (a) and (b) respectively.

(a) ^{87}Rb

F	m_{F}	$\frac{\partial B}{\partial z}$ (G/cm)
2	± 2	15.3
	± 1	30.5
	0	N/A
1	± 1	30.5
	0	N/A

(b) ^{133}Cs

F	m_{F}	$\frac{\partial B}{\partial z}$ (G/cm)
4	± 4	23.3
	± 3	31.1
	± 2	46.7
	± 1	93.4
	0	N/A
3	± 3	31.1
	± 2	46.7
	± 1	93.4
	0	N/A

Table 2.2: Magnetic field gradients required to levitate ground state (a) ^{87}Rb and (b) ^{133}Cs atoms against gravity with no bias field present.

The quadratic nature of the Zeeman effect revealed in equation 2.54 results in the magnetic moment, μ, being a function of the bias field, B. This results in the magnetic field gradient required for levitation also depending on the applied bias field. This behaviour is approximated using equations 2.62 and 2.63 for the $|1, -1\rangle$ state in ^{87}Rb and the $|3, -3\rangle$ state in ^{133}Cs respectively,

where the applied field B is in Gauss.

$$\frac{\partial B}{\partial z}_{\text{Rb}} = (30.5 + 0.019 \times B) \text{ G/cm}, \tag{2.62}$$

$$\frac{\partial B}{\partial z}_{\text{Cs}} = (31.1 + 0.0055 \times B) \text{ G/cm}. \tag{2.63}$$

For bias fields < 90 G the magnetic gradient required to levitate the $|1, -1\rangle$ and $|3, -3\rangle$ states for ^{87}Rb and ^{133}Cs respectively differ by just $\simeq 2$ %. This allows both species to be levitated against gravity using the same magnetic field gradient and ensures excellent spatial overlap between the two clouds. The addition of a bias field in the vertical direction to offset the field zero position allows either high or low field seeking states to be levitated. By offsetting the zero to be above the cloud low field seeking states are levitated and when the zero is positioned below the cloud high field seeking states are levitated.

2.6 RF Evaporation in a Quadrupole Trap

A trapped atomic sample in thermal equilibrium can be evaporatively cooled by the selective removal of atoms with energies higher than the mean energy of the sample. Once elastic collisions have rethermalised the sample the temperature of the cloud will have reduced. In the magnetic quadrupole trap this selective removal is achieved using forced radio-frequency (RF) induced transfer into non-magnetically trappable states [134]. In the trap hot atoms have a large spatial extent and span a large range of magnetic field values. These can be specifically addressed by selecting a higher RF frequency that only removes atoms with large Zeeman shifts, equation 2.56. Efficient evaporative cooling relies on a large ratio of 'good' (elastic) to 'bad' (inelastic) collisions to ensure the rethermalisation time is much shorter than the lifetime of the trapped atomic sample. The evaporation efficiency is defined as

$$\gamma = -\frac{\log(D_0/D)}{\log(N_0/N)}, \tag{2.64}$$

where N_0 (D_0) and N (D) are the initial and final numbers (phase-space densities) respectively.

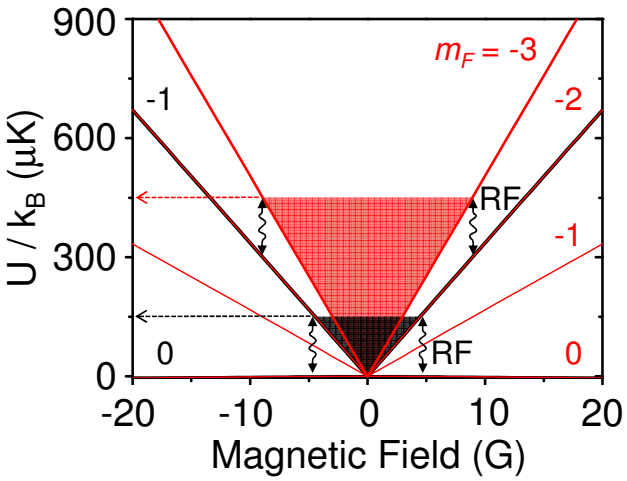

Figure 2.7: The magnetic quadrupole potential for ^{87}Rb (black) and ^{133}Cs (red). The depth of the quadrupole trap defined by the RF is 3 times deeper for ^{133}Cs than ^{87}Rb. This enables the sympathetic cooling of ^{133}Cs via ^{87}Rb during the precooling in the magnetic trap.

For the ^{87}Rb - ^{133}Cs mixture in the $|1,-1\rangle$ and $|3,-3\rangle$ states respectively the magnetic trap depth determined by the RF frequency is exactly 3 times deeper for ^{133}Cs than for ^{87}Rb, figure 2.7. Consider the RF photon energy required to induce a transition into an untrapped state

$$h\nu = g_F \mu_B \left|\frac{\partial B}{\partial z}\right| z, \tag{2.65}$$

so $z_{\mathrm{Rb}} = 2h\nu/(\mu_B \left|\frac{\partial B}{\partial z}\right|)$ and $z_{\mathrm{Cs}} = 4h\nu/(\mu_B \left|\frac{\partial B}{\partial z}\right|)$. The position of the 'RF knife' is then given by

$$E_{\mathrm{cut}} = m_F g_F \mu_B \left|\frac{\partial B}{\partial z}\right| z, \tag{2.66}$$

substituting for z for each species therefore gives $E_{\mathrm{cut}}^{\mathrm{Rb}} = h\nu$ and $E_{\mathrm{cut}}^{\mathrm{Cs}} = 3h\nu$. This allows the selective RF evaporation of ^{87}Rb while interspecies elastic collisions sympathetically cool ^{133}Cs. The sympathetic cooling of ^{133}Cs via ^{87}Rb in the magnetic trap is presented in section 6.1.

2.7 Optical Trapping

Optical dipole traps use the interaction of the induced dipole moment with the intensity gradient of the light field. Here the ac electric field of the

laser drives oscillations of the induced dipole moment. If the frequency of the electric field is red-detuned (blue-detuned) with respect to the atomic resonance the resulting optical potential is attractive (repulsive). For far-detuned light, photon scattering rates are low enough to consider the optical potential conservative. The optical potential U_{dip}, and the scattering rate Γ_{sc}, are given by [135]

$$U_{\mathrm{dip}}(r) = -\frac{1}{2\epsilon_0 c}\Re(\alpha)I(r) \approx \frac{3\pi c^2\Gamma}{2\omega_0^3}\frac{I(r)}{\Delta}, \tag{2.67}$$

$$\Gamma_{\mathrm{sc}} = \frac{1}{\hbar\epsilon_0 c}\Im(\alpha)I(r) \approx \frac{3\pi c^2}{2\hbar\omega_0^3}\left(\frac{\Gamma}{\Delta}\right)^2 I(r). \tag{2.68}$$

Here $\Re(\alpha)$ ($\Im(\alpha)$) is the real (imaginary) part of the complex polarisability α. The resonant transition frequency is ω_0, Γ is the decay rate from the excited state and $I(r)$ is the intensity of the light field. Equations 2.67 and 2.68 show that the dipole potential scales as I/Δ, whereas the scattering rate scales as I/Δ^2. This results in dipole traps typically using large detunings and high intensities to keep scattering rates low for a certain potential depth. An attractive feature of these traps is that the optical dipole force can confine atoms in all hyperfine states. This allows the high field seeking atomic ground states to be trapped therefore making inelastic two-body losses energetically forbidden.

In this experiment attractive optical potentials are used from two 1550 nm beams derived from a 30 W fibre laser (IPG ELR-30-LP-SF) and focussed to waists of $\simeq 60$ μm. Further details on the dipole trap setup are given in section 3.8.

Chapter 3

Experimental Apparatus: New Tools and Upgrades

The majority of the apparatus and techniques used in this experiment have been carefully documented in other sources [93, 94]. Only new features or modifications to the original apparatus and method are highlighted in this chapter. In brief these changes are:

- A new optical table setup using acousto-optic modulators (AOMs) for intensity and frequency control of the majority of the laser light.
- The laser locking scheme has been upgraded from the dichroic atomic vapour laser lock (DAVLL) to modulation transfer spectroscopy and frequency modulation (FM) spectroscopy and now offers greater frequency stability.
- A modified slave laser design offers greater temperature stability and the injection light alignment has been improved by using an optical fibre.
- A new magnetic field coil assembly has replaced the Ioffe-Pritchard 'baseball' trap and can provide tight magnetic confinement and bias fields in excess of 1150 G.
- A new double magneto-optical trap (MOT) alignment provides improved optical access to the east and west faces of the glass cell.

- An optical dipole trap has been integrated into the setup and combined with a magnetic component to form versatile 'hybrid' trapping potentials.
- Servomechanical control of the ^{133}Cs science MOT fluorescence voltage has been implemented to accurately tune and stabilise the number of ^{133}Cs atoms loaded.

The modified experimental setup was then used in the studies presented in chapters 4-8.

3.1 Overview

The ^{87}Rb - ^{133}Cs mixture experiment is divided between two independent optical tables. The first table contains the laser systems required to prepare the necessary light frequencies and intensities for laser cooling, repumping, optical pumping and imaging both species. Polarisation maintaining optical fibres couple this light to the second table which houses the vacuum system and the required cooling and trapping hardware. The heart of the experimental setup consists of a levitated crossed dipole trap located at the centre of a UHV glass cell. This simple and versatile trapping potential is comprised of two intersecting laser beams, a magnetic field gradient from an anti-Helmholtz coil pair and a uniform bias field from a Helmholtz coil pair.

The optical setup and locking scheme detailed in this chapter allows the Rb laser system to be locked to either the ^{87}Rb or ^{85}Rb cooling and repump transitions with minimal changes to the setup. This enables both ^{87}Rb - ^{133}Cs and ^{85}Rb - ^{133}Cs mixtures to be studied using this apparatus. At the time of writing initial experiments on a ^{85}Rb - ^{133}Cs mixture are underway.

3.2 Optical Frequencies

To continuously laser cool and trap atoms in a MOT a closed atomic transition is required. Here the D_2 ($S_{1/2} \rightarrow P_{3/2}$) lines for both ^{87}Rb and ^{133}Cs

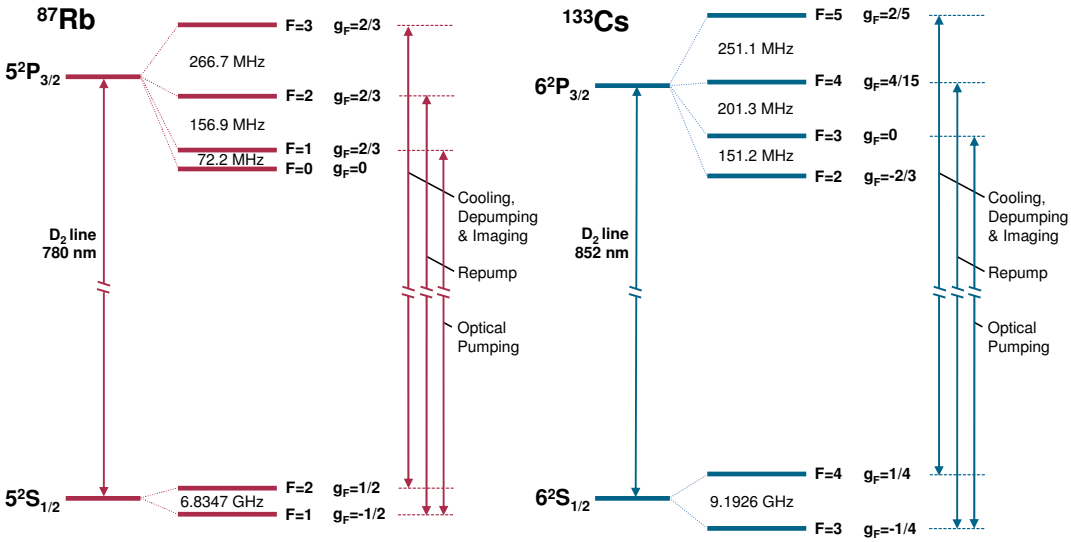

Figure 3.1: Energy level scheme for the D_2 lines in ^{87}Rb and ^{133}Cs (frequencies are not to scale). The arrows indicate the laser transitions used in this experiment for the MOT, optical pumping and imaging.

are used at 780 nm and 852 nm respectively. Figure 3.1 highlights the relevant hyperfine structure and optical transitions for both species used in this experiment. The successful laser cooling of atoms requires the absolute laser frequencies to be controlled to < 1 MHz, significantly below the natural linewidth of the cooling and repumping transitions. These transitions occur at $\simeq 385$ THz and $\simeq 352$ THz for ^{87}Rb and ^{133}Cs respectively and so each laser frequency must be stable to within one part in $\sim 10^8$. Such stability requires active frequency stabilisation or 'locking' of the laser using an error signal to act as a frequency discriminant. The methods used to produce error signals for laser locking in this experiment are discussed in section 3.4.

The specific laser frequencies used in this experiment are presented in table 3.1. Precise control of all detunings is provided by six AOMs for each species. The full optical setup is discussed in section 3.3.

3.3 Laser System Overview

A system of six laser diodes, three for each species, provides the necessary light for the experiment. A simple schematic diagram of the laser system for

	^{87}Rb		^{133}Cs	
	Transition	Detuning (MHz)	Transition	Detuning (MHz)
Pyramid	$F = 2 \rightarrow F' = 3$	-18.3(1)	$F = 4 \rightarrow F' = 5$	-16.8(1)
Spectroscopy	$F = 2 \rightarrow F' = 3$	0.0(1)	$F = 4 \rightarrow F' = 5$	0.0(1)
MOT	$F = 2 \rightarrow F' = 3$	-12.2(1)	$F = 4 \rightarrow F' = 5$	-10.3(1)
CMOT	$F = 2 \rightarrow F' = 3$	-30.9(1)	$F = 4 \rightarrow F' = 5$	-28.4(1)
Molasses	$F = 2 \rightarrow F' = 3$	-59.4(1)	$F = 4 \rightarrow F' = 5$	-53.7(1)
Depumping	$F = 2 \rightarrow F' = 3$	-96.2(1)	$F = 4 \rightarrow F' = 5$	-67.1(1)
Imaging (at 2.7(1) G)	$F = 2 \rightarrow F' = 3$	-3.6(1) σ^- 3.7(1) σ^+	$F = 4 \rightarrow F' = 5$	-4.0(1) σ^- 3.7(1) σ^+
Repump Laser	$F = 2 \rightarrow X_{1,2}$	-1.6(1)	$F = 4 \rightarrow X_{3,4}$	0.1(1)
Repumping	$F = 1 \rightarrow F' = 2$	0.0(1)	$F = 3 \rightarrow F' = 4$	0.0(1)
Optical Pumping	$F = 1 \rightarrow F' = 1$	+5.9(1)	$F = 3 \rightarrow F' = 3$	+11.9(1)

Table 3.1: Laser frequencies used for magneto-optical trapping, sub-Doppler cooling, optical pumping and imaging of ^{87}Rb and ^{133}Cs in the experiment.

^{133}Cs is presented in figure 3.2, the setup for ^{87}Rb is similar. Two commercial extended cavity 'master' lasers (Toptica DL100) in the Littrow configuration provide $\simeq$ 120 mW and $\simeq$ 150 mW of light at 780 nm and 852 nm respectively. This light is used for cooling in the science MOT, absorption imaging and injecting home-built 'slave' lasers for each species. The slave lasers provide $\simeq$ 70 mW of cooling light for each species in the two-species pyramid MOT. Other home-built extended cavity diode lasers are based on the design presented in [136] and provide $\simeq$ 40 mW of light for the repumping and optical pumping of each atomic species.

3.3.1 Optical Setup

The full optical setup implements the simplified scheme shown in figure 3.2 for both species and is presented in figure 3.3. This setup represents a significant improvement over the previous optical setup [93, 94]. In the previous setup AOMs offered intensity control of only the optical pumping and imaging light for both species. Frequency detunings were controlled either with AOMs or by adding specific voltage offsets to the lock-points of the mas-

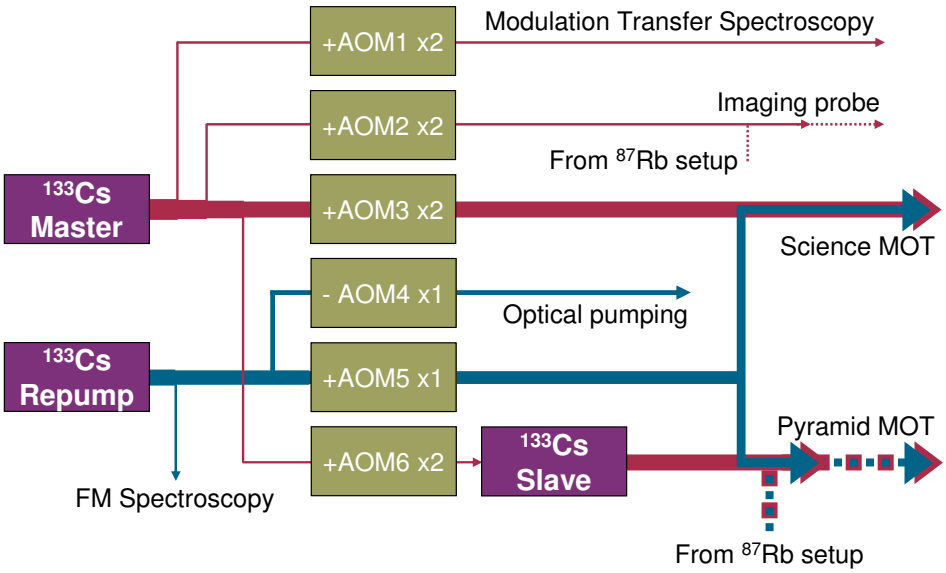

Figure 3.2: Schematic of the laser table optical setup for ^{133}Cs. Three lasers produce light for the cooling, repumping, optical pumping and imaging of each species in the double-MOT system. Line thickness indicates relative beam power. AOMs in single-pass (x1) and double pass (x2) configurations allow independent control of all intensities and frequency detunings. For the imaging light and pyramid MOT, dichroic optics are used to combine the 852 nm (solid lines) and 780 nm (dashed lines) beams before transmitting both wavelengths down single fibres. The optical setup for ^{87}Rb is similar.

ter and repump lasers. This was possible as the lasers were locked using a heated version of DAVLL [137]. This single beam technique has Doppler-broadened spectral features and consequently exhibits a large capture range of several hundred MHz. This feature enabled the laser lock-point to be tuned and switched rapidly over a large range of frequencies. However this relied on the error signal lineshape being fixed which was not always the case. The DAVLL signal is sensitive to changes in temperature, polarisation and magnetic field which result in unwanted drifts in frequency. In the new optical setup AOMs provide precise frequency and intensity control of all the laser light other than the intensity of the pyramid MOT cooling light. This greater versatility allows detunings and intensities to be independently optimised at each phase of the experiment, though at the expense of a slight reduction in the laser power available. To improve the laser locks and remove

the lock-point's dependence on temperature, polarisation and magnetic field the locking schemes have been changed from DAVLL to modulation transfer spectroscopy and FM spectroscopy.

3.4 Laser Frequency Stabilisation

To control the cooling and repump laser frequencies to < 1 MHz, significantly below the natural linewidth, the lasers must be actively stabilised or 'locked' using an error signal to act as a frequency discriminant. There are numerous methods to generate an error signal for laser locking including the dichroic atomic vapour laser lock (DAVLL) [138, 139], a combination of DAVLL and saturation absorption [140], polarisation spectroscopy [141], modulation transfer spectroscopy [142, 143] and FM spectroscopy [144]. In the new setup the master lasers are locked with modulation transfer spectroscopy and the repump lasers with FM spectroscopy. Both modulation transfer and FM spectroscopy are pump-probe schemes which achieve sub-Doppler resolution. This results in steeper signal gradients and enhanced frequency discrimination, though at the expense of a more limited capture range typically below one hundred MHz.

3.4.1 Modulation Transfer Spectroscopy

Modulation transfer spectroscopy uses two counter-propagating laser beams referred to as the pump and probe beams, as in saturation absorption/hyperfine pumping spectroscopy [145]; however, it should be noted that optimal signals are recorded when the beam powers are approximately equal. The underlying principle of this technique is as follows. An intense single frequency pump beam is passed through an electro-optic modulator (EOM), driven by an oscillator at frequency ω_m. The transmitted light is phase-modulated and can be represented by a carrier frequency ω_c and sidebands separated by the modulation frequency ω_m

$$E = E_0 \mathrm{sin}[\omega_\mathrm{c} \mathrm{t} + \delta \mathrm{sin} \omega_\mathrm{m} \mathrm{t}],$$

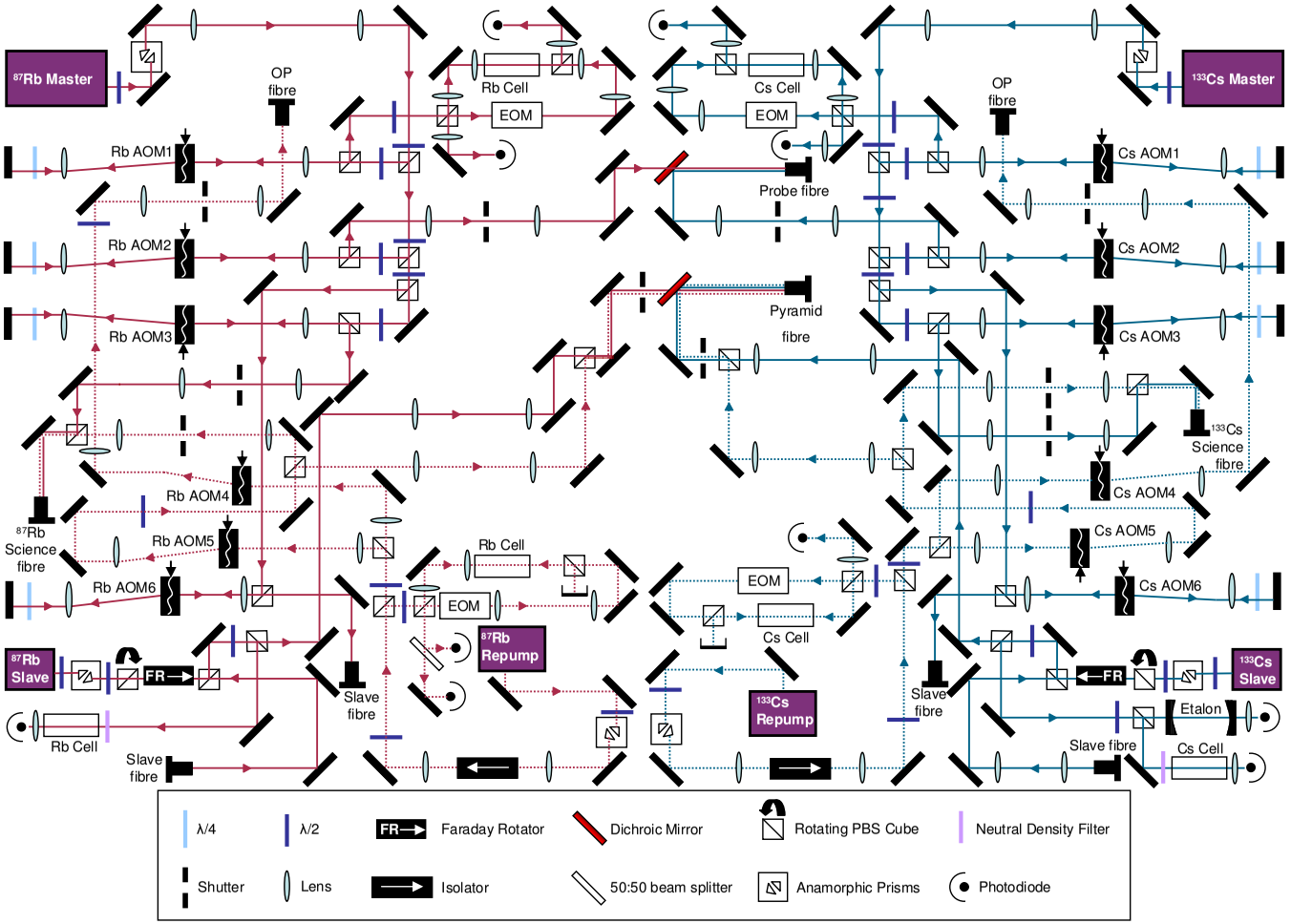

Figure 3.3: Optical setup of the laser table. Light for transitions from the upper and lower ground states are indicated with solid and dashed lines respectively for both ^{87}Rb (red) and ^{133}Cs (blue). Polarisation maintaining optical fibres couple the light from this table to the experiment.

$$E = E_0 \left[\sum_{n=0}^{\infty} J_n(\delta)\sin(\omega_c + n\omega_m)t + \sum_{n=1}^{\infty}(-1)^n J_n(\delta)\sin(\omega_c - n\omega_m)t \right], \quad (3.1)$$

where δ is the modulation index and $J_n(\delta)$ is the Bessel function of order n. Typically the modulation index $\delta < 1$, so the pump beam can be adequately described by a strong carrier wave at ω_c and two weak sidebands at $\omega_c \pm \omega_m$. The modulated pump and the counter-propagating, unmodulated probe beams are aligned collinearly through an atomic vapour cell. If interactions of both beams with the atomic vapour are sufficiently nonlinear, modulation appears on the unmodulated probe beam. This modulation transfer is an example of four-wave mixing [146]. Here two frequency components of the pump beam combine with the probe beam via the third order susceptibility, $\chi^{(3)}$, to generate a fourth wave - a sideband for the probe beam.

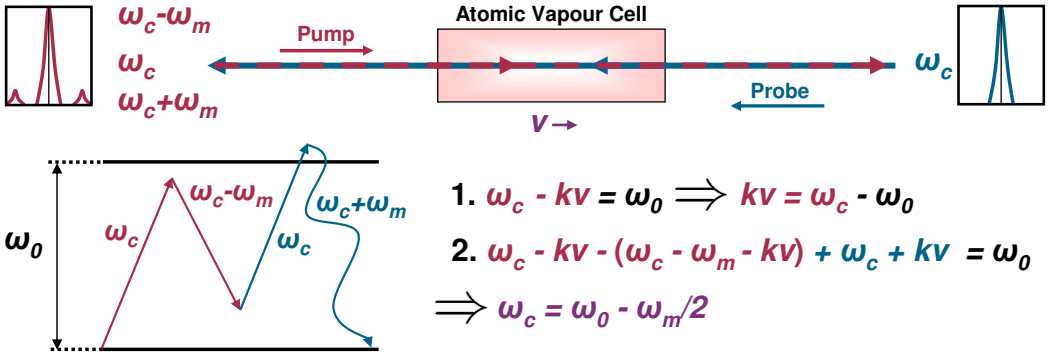

Figure 3.4: A simple setup for modulation transfer. A phase-modulated pump beam and a counter-propagating, unmodulated probe beam are aligned collinearly through a vapour cell. Four-wave mixing results in modulation transfer and generates a sideband on the probe beam. The four-wave mixing process is described in the text.

Four-wave mixing occurs only at specific laser frequencies. An example of how to calculate the specific laser frequencies is detailed in figure 3.4. The calculation assumes that both beams interact with an atom with velocity v in the direction of propagation of the pump beam. This results in a Doppler shift in frequency of kv, where k is the wave vector $2\pi/\lambda$. The first step considers the first transition only (here ω_c) which must equal the resonant frequency ω_0, this is rearranged to give an expression for kv. The second

step includes the first three transitions which also must be equal to ω_0. By substituting in for kv the expression simplifies to reveal that this process occurs at a laser frequency of $\omega_c = \omega_0 - \omega_m/2$. This process occurs for each sideband of the pump beam. The three constituent waves and order of mixing dictates which probe sideband is created. The phase of the generated probe sideband is the same as the pump sideband that created it. Assuming the pump beam has sidebands at $\omega_c \pm \omega_m$ only, four-wave mixing occurs at just four specific laser frequencies $\omega_0 \pm \omega_m$ and $\omega_0 \pm \omega_m/2$. These four specific cases of modulation transfer are presented in figure 3.5.

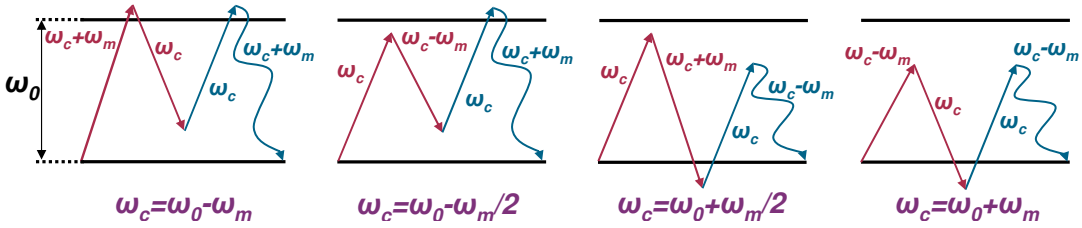

Figure 3.5: Transitions between two energy levels for the four cases of modulation transfer for a pump beam with sidebands at $\omega_c \pm \omega_m$. The three constituent waves and the order of mixing dictates which probe sideband is made. The phase of the generated sideband is the same as that of the pump sideband that formed it.

After passing through the vapour cell the probe beam is incident on a fast photodiode. The probe sidebands generated in the vapour beat with the probe beam carrier to produce alternating signals at the modulation frequency ω_m. This beat signal is of the form

$$S(\omega_m) = \frac{C_m}{\sqrt{\Gamma^2 + \omega_m^2}} \sum_{n=-\infty}^{\infty} J_n(\delta) J_{n-1}(\delta)$$
$$\times [(L_{(n+1)/2} + L_{(n-2)/2}) \cos(\omega_m t + \phi)$$
$$+ (D_{(n+1)/2} + D_{(n-2)/2}) \sin(\omega_m t + \phi)], \tag{3.2}$$

where

$$L_n = \frac{\Gamma^2}{\Gamma^2 + (\Delta - n\omega_m)^2}, \tag{3.3}$$

and

$$D_n = \frac{\Gamma(\Delta - n\omega_m)}{\Gamma^2 + (\Delta - n\omega_m)^2}. \tag{3.4}$$

Here Γ is the natural linewidth, Δ is the frequency detuning from line centre and ϕ is the detector phase with respect to the modulation field applied to the pump laser. The constant C_m represents all the other properties of the medium and the probe beam that are independent of the parameters described above. If we assume that $\delta < 1$ and consider only the first order sidebands then equation 3.2 is simplified to

$$S(\omega_m) = \frac{C_m}{\sqrt{\Gamma^2 + \omega_m^2}} J_0(\delta) J_1(\delta)$$
$$\times[(L_{-1} - L_{-1/2} + L_{1/2} - L_1)\cos(\omega_m t + \phi)$$
$$+(D_1 - D_{1/2} - D_{-1/2} + D_{-1})\sin(\omega_m t + \phi)]. \quad (3.5)$$

In equations 3.2 and 3.5 the sine term represents the quadrature component of the signal and the cosine term the in-phase component of the signal. Using a phase-sensitive detection scheme (figure 3.6), it is possible to recover the absorption and dispersion components of the sub-Doppler resonance by setting the phase of the reference signal to select either the in-phase or quadrature signal component, respectively [142]. For laser locking the maximum peak to peak amplitude is desired. This does not occur when the detector phase is set solely for the quadrature or in-phase signal components. In general a mix of the two components is required to produce the maximum signal [147].

The strongest modulation transfer signals are observed for closed transitions; here four-wave mixing is very efficient as atoms cannot relax into other ground states. Modulation transfer signals are observed for open transitions but here four-wave mixing is improbable. Typical peak to peak amplitudes of signals for open transitions are ~ 10 times smaller than those for closed transitions, see figure 3.10. This makes modulation transfer spectroscopy signals ideal for locking to the closed cooling transitions. To produce large error signals to lock to the open repump transitions the technique of frequency modulation (FM) spectroscopy is employed.

As modulation transfer only occurs when the sub-Doppler resonance condition is satisfied the lineshape baseline stability is almost independent of the residual linear-absorption effect. This leads to a flat, zero background signal and is one of the major advantages of this technique. The lineshape baseline stability is therefore independent of changes in absorption due to

fluctuations in temperature, polarisation and beam intensity. Another advantage is that the signal zero-crossing always falls on the centre of the sub-Doppler resonance and is not affected by, for example, magnetic field or wave plate angle-dependent shifts which upset both DAVLL and polarisation spectroscopy.

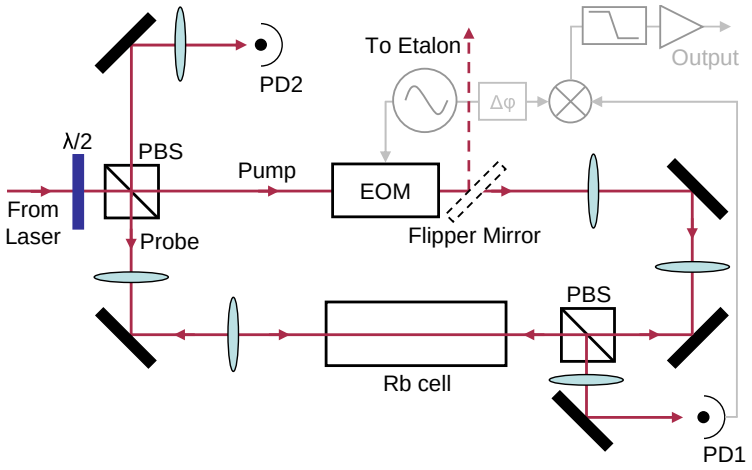

Figure 3.6: Schematic diagram of the modulation transfer experimental setup (PBS = polarising beam splitter, PD = photodiode, EOM = electro-optic modulator) including the phase sensitive detection scheme used to isolate and demodulate the beat signal. Telescopes were used to expand the pump and probe beams. The second photodiode (PD2) can be used to observe either a saturation absorption spectrum or an FM spectroscopy signal using the same setup. A flipper mirror was used to send the modulated light to an etalon to monitor the sidebands applied to the pump beam.

The experimental setup for modulation transfer spectroscopy is shown in figure 3.6. A low order half-wave plate was set to give the maximum signal amplitude. For ^{87}Rb this corresponded to a probe (pump) laser power of 1.55(5) mW (1.35(5) mW). Telescopes consisting of 25 mm and 100 mm lenses increased the size of both the ^{87}Rb pump and probe beams from $1/e^2$ radii of 0.53(1) mm to 2.16(6) mm. The probe beam was aligned collinearly with the counter-propagating pump beam through a 5 cm long room temperature vapour cell and then detected using a homemade transimpedance amplifier circuit and a fast photodiode (Hamamatsu S5972) with a responsivity of 2.8 V/mW. The signal from the photodiode was sent to a frequency mixer

(Mini-Circuits ZAD-1H+) before the output was amplified by a factor of $\simeq 200$ and sent through a 16 kHz low-pass active filter. The filter also served to remove the high frequency signal from the mixer. The modulation signal from the oscillator (TTi TG120) was set to 20 V peak to peak amplitude and split (Mini-Circuits ZSC-2-1+) with one part going to the EOM and the other to the mixer. At each modulation frequency the phase of the signal was optimised to give the maximum peak to peak amplitude of the output signal. This was done by altering the coaxial cable length between the function generator and mixer. A flipper mirror sent the modulated light into an etalon with a 300 MHz free-spectral range (Coherent 33-6230-001) and enabled the sideband/carrier ratio to be measured.

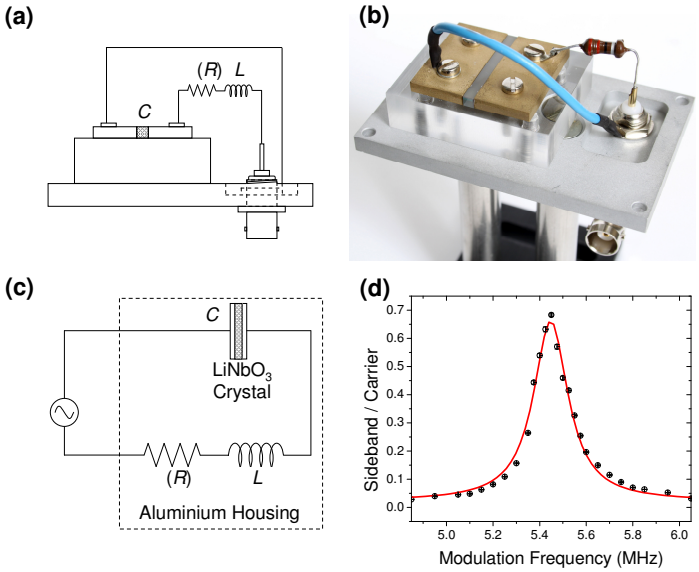

Figure 3.7: (a) Schematic diagram of the home-built EOM setup with (b) a photograph of the same setup. (c) A simple LCR circuit where L is the inductance of the inductor, R is the resistance of the inductor and C is the capacitance of the crystal. (d) By plotting the sideband height as a fraction of the carrier height it is possible to map out the resonance as a function of frequency, a Lorentzian fit gives a Q-Factor of 15(1).

The pump beam was phase-modulated using a home-built EOM assembly, figure 3.7(a). The device uses a lithium niobate ($LiNbO_3$) crystal (supplied by DÖHRER Elektrooptik). The crystal measures 3 mm wide, 3 mm deep and 30 mm long. Both 3×3 mm faces were optically polished to laser finish

and had a broadband (650-1000 nm) anti-reflection coating applied to them. The crystal sides (Z-faces) were coated with chrome-gold to form electrodes. The crystal was mounted between two brass electrodes, using silver paint to ensure good electrical contact, so that an electric field could be applied transverse to the optical axis. The crystal and electrodes were then mounted on a perspex block within an aluminium housing. The crystal was connected in a simple resonant LCR circuit, figure 3.7 (c), driven by an oscillator in order to enhance the amplitude of the ac voltage across the crystal. The resonant frequency of the circuit is $\omega = \frac{1}{\sqrt{LC}}$ [148], where L is the inductance of the inductor and C is the parallel plate capacitance of the crystal between the two electrodes. Figure 3.7 (d) shows a typical resonance at 5.45(1) MHz. On resonance, the voltage across the crystal is increased with respect to the voltage applied to the circuit by a factor equal to the Q-factor of the circuit. FM spectroscopy signals can also be observed using this setup by monitoring the modulated beam using a fast photodiode and a phase sensitive detection scheme at the position marked by PD2 in figure 3.6.

Optimisation of Modulation Transfer Lineshapes for Laser Locking

Modulation transfer lineshapes were studied to establish the experimental parameters that yield the optimum signals for laser locking [143]. As the frequency stability of any locked laser depends on many parameters, including the passive stability of the laser design and the performance of the servo electronics, this study was confined to the behaviour of the amplitude and gradient of the modulation transfer signal. To obtain the maximum signal amplitude for each modulation frequency before any optimisation a mix of the in-phase and quadrature components was used [147].

Figure 3.8 shows data for the ^{87}Rb $F = 2 \rightarrow F' = 3$ transition with beam waists of (a) 2.16(6) mm, and (b) 0.53(1) mm, using the telescopes shown in figure 3.6. Modulation frequencies of 5.45(1), 7.20(1), 10.50(1), 12.35(1), 14.90(1) and 19.80(1) MHz were investigated for both cases. These figures clearly show that, for the same beam powers, using telescopes to expand the beams to waists of 2.16(6) mm improves the signal for laser locking. This improvement follows from the narrower effective sub-Doppler linewidth,

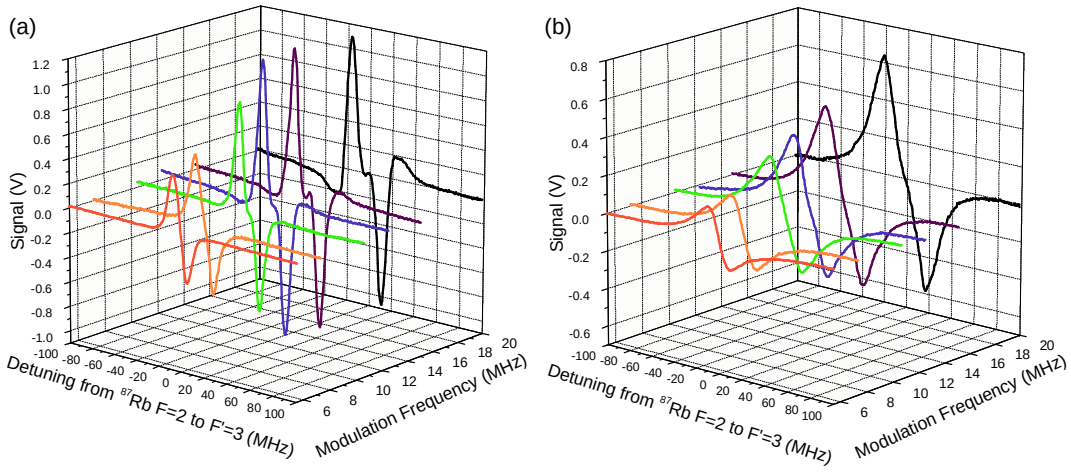

Figure 3.8: Modulation transfer spectroscopy signals for the ^{87}Rb $F = 2 \rightarrow F' = 3$ transition as a function of modulation frequency for beam waists of (a) 2.16(6) mm and (b) 0.53(1) mm. The modulation frequencies in MHz are 5.45(1) (red), 7.20(1) (orange), 10.50(1) (green), 12.35(1) (blue), 14.90(1) (purple) and 19.80(1) (black). The data were obtained with a sideband/carrier ratio of 13.2(2)%.

Γ', in the case where the beam intensity is reduced, which then results in sharper modulation transfer signals. As the signal also increases with the total amount of power in the beams, this improvement cannot be achieved by simply reducing the total power in the setup.

Figure 3.8 (a) shows that as the modulation frequency, ω_m, becomes greater than the effective sub-Doppler linewidth Γ', a 'kink' appears in the locking slope. If the modulation frequency is increased further this 'kink' becomes more pronounced until eventually the zero crossing gradient changes sign. Generally the signals shown in figure 3.8 (b), for beam waists of 0.53(1) mm, do not show this behavior as the effective sub-Doppler linewidth, Γ', has been increased due to power broadening. Despite this broadening, a small decrease in the zero crossing gradient can be seen for the 19.80 MHz signal as again the modulation frequency ω_m, becomes greater than the effective sub-Doppler linewidth Γ'.

The data of figure 3.9 show the evolution of the signal gradient and amplitude for the ^{87}Rb $F = 2 \rightarrow F' = 3$ transition, (a) and (c) respectively, and the ^{85}Rb $F = 3 \rightarrow F' = 4$ transition, (b) and (d) respectively, for dif-

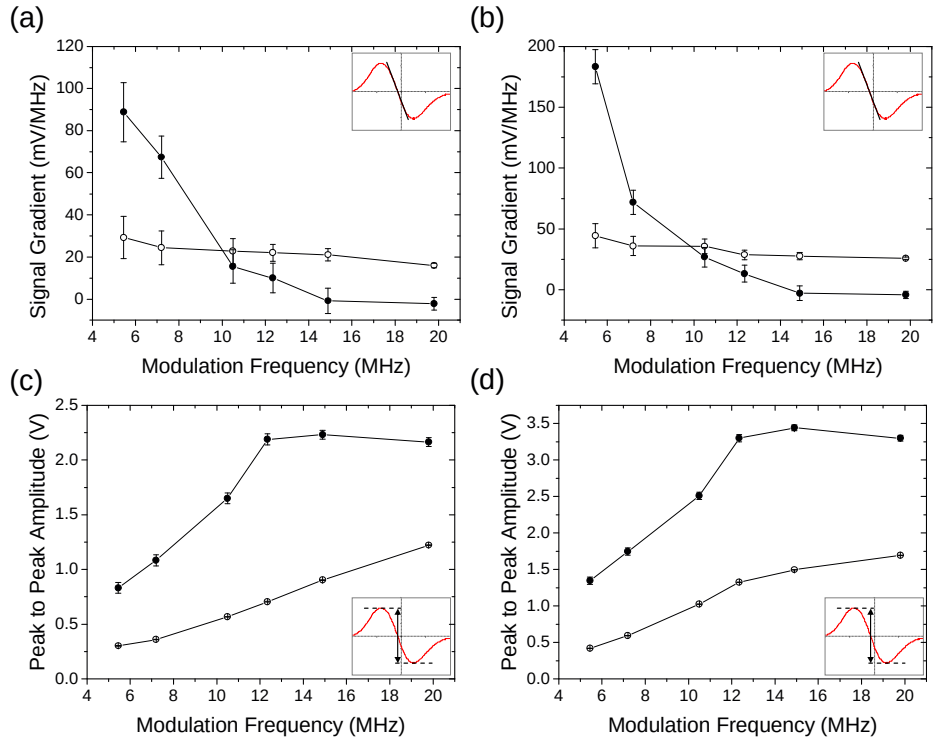

Figure 3.9: Zero crossing gradients of the modulation transfer signal as a function of modulation frequency for (a) the ^{87}Rb $F = 2 \rightarrow F' = 3$ and (b) the ^{85}Rb $F = 3 \rightarrow F' = 4$ transitions. Peak to Peak amplitudes of the modulation transfer signal as a function of the modulation frequency for (c) the ^{87}Rb $F = 2 \rightarrow F' = 3$ and (d) the ^{85}Rb $F = 3 \rightarrow F' = 4$ transitions. Closed and open symbols show data obtained using beam waists of 2.16(6) mm and 0.53(1) mm respectively.

ferent modulation frequencies. Data sets were taken using beam waists of 2.16(6) mm (closed symbols), and 0.53(1) mm (open symbols) in the setup. The data show that for beam waists of 0.53(1) mm, as the modulation frequency is increased, the signal gradient decreases and the signal amplitude increases monotonically. However for beam waists of 2.16(6) mm, as the modulation frequency increases the signal gradient decreases and reaches approximately zero when $\omega_m \simeq 15$ MHz for both the ^{87}Rb $F = 2 \rightarrow F' = 3$ and the ^{85}Rb $F = 3 \rightarrow F' = 4$ transitions. The data show that for increasing ω_m the signal peak to peak amplitude increases to a maximum value at $\omega_m \simeq 14$ MHz for both transitions and then begins to decrease.

Using a model based on equation 3.5, the mix of in-phase and quadrature components to give the signal with maximum amplitude was compared to the data as a function of the modulation frequency. This analysis gives the reasonable effective sub-Doppler linewidths of $\simeq 9$ MHz and $\simeq 14$ MHz for beam waists of 2.16(6) mm and 0.53(1) mm respectively. These linewidths are greater than the natural linewidth of $\Gamma = 2\pi \times 6.065(9)$ MHz [145], most probably due to power broadening. However, the intensity dependence of the effective sub-Doppler linewidth in modulation transfer spectroscopy is not trivial to calculate as the underlying four-wave mixing process cannot be treated as a simple two level system. For example, for the low modulation index δ used in this work, the intensity of the sidebands involved in the four-wave mixing process is greatly reduced compared to the carrier intensity. Additionally four-wave mixing only occurs at detunings of $\omega_0 \pm \omega_m/2$ and $\omega_0 \pm \omega_m$, where ω_0 is the frequency of the sub-Doppler resonance. This complexity becomes apparent if the effective sub-Doppler linewidth is calculated using [149]

$$\Gamma' = \Gamma\sqrt{1 + \frac{I}{I_{\text{sat}}}}, \tag{3.6}$$

where I is the beam intensity and I_{sat} is the saturation intensity for linearly polarized light on the D2 transition in rubidium.

For the intensities used in this experiment, equation 3.6 gives effective sub-Doppler linewidths of approximately 3Γ ($\approx 18\,\text{MHz}$) and 12Γ ($\approx 72\,\text{MHz}$) for beam waists of 2.16(6) mm and 0.53(1) mm respectively. Clearly these values are in strong disagreement with our observations and indicate that in practice large intensities can be used for modulation transfer spectroscopy without increasing the effective sub-Doppler linewidth. The relatively high intensities used in this investigation are in part an artifact of the low gain of the fast photodiode used. We should note that another modulation transfer setup in Durham uses a photodiode with much higher gain and observes comparable signals to those presented here with beam intensities of the order of I_{sat}. Interestingly, these signals still show the dominance of closed transitions as this is an artifact of the four-wave mixing process.

Optimum locking signals are produced when telescopes are used in the modulation transfer spectroscopy setups for both species. The modulation frequen-

cies are set to 5.17(1) MHz and 6.26(2) MHz for ^{87}Rb and ^{133}Cs respectively to provide locking signals with large gradients and large amplitudes. By expanding the beams the signal gradient can be increased by up to a factor of ~ 3 and the peak to peak amplitude increased by up to a factor of ~ 2 for both species.

3.4.2 Frequency Modulation Spectroscopy

In frequency modulation (FM) spectroscopy the roles of the probe and pump beams are reversed when compared to modulation transfer spectroscopy. In FM spectroscopy a weak probe beam is phase-modulated using an EOM and overlapped with an intense unmodulated counter-propagating pump beam in an atomic vapour cell before being detected. FM spectra can be observed by placing a phase-sensitive detection scheme at the position of PD2 in figure 3.6. When the modulated probe is incident on a fast photodiode each sideband beats with the carrier at the modulation frequency, ω_m. For pure FM light (equation 3.1) the two beat signals are equal but of opposite phase and therefore cancel exactly. However, the atomic medium can upset this perfect cancellation by altering the amplitude or phase of one of the sidebands as the light probes an atomic transition and give rise to an FM signal.

Consider an atomic sample with length L, a refractive index $n(\omega)$ and intensity absorption coefficient $\alpha(\omega)$. For the case of a small modulation index ($\delta < 1$) and weak absorption the intensity of the probe beam at the detector is given by

$$I(t) = \frac{cE_0^2}{8\pi} e^{-2\zeta_o} J_0(\delta) \times$$
$$\left[J_0(\delta) + J_1(\delta)(\zeta_{-1} - \zeta_1)\mathrm{cos}\omega_\mathrm{m}\mathrm{t} + \mathrm{J}_1(\delta)(\phi_1 - 2\phi_0 + \phi_{-1})\mathrm{sin}\omega_\mathrm{m}\mathrm{t}\right] \qquad (3.7)$$

where $\zeta_j = \alpha_j L/2$ defines the amplitude attenuation, $\phi_j = n_j L(\omega_c + j\omega_m)/c$ describes the optical phase shift experienced by each component and $j = 0, \pm 1$ denotes the components at ω_c and $\omega_c \pm \omega_m$ [150]. The electrical signal from the photodiode is proportional to the intensity $I(t)$ and will contain a beat signal at ω_m if $\zeta_{-1} - \zeta_1 \neq 0$ or $\phi_1 - 2\phi_0 + \phi_{-1} \neq 0$. Similar to equations 3.2 and 3.5 for modulation transfer spectroscopy the $\mathrm{cos}\omega_m t$ and $\mathrm{sin}\omega_m t$ components of the signal described by equation 3.7 are proportional to the absorption and dispersion induced by the spectral feature respectively.

The exact form of the FM spectroscopy signal depends on the lineshape of the absorption feature being probed. If the feature has a Lorentzian lineshape and we consider only the first order sidebands the resulting beat signal as the carrier frequency is scanned across the atomic resonance is given by

$$S(\omega_m) = \frac{A_m}{\sqrt{\Gamma^2 + \omega_m^2}} J_0(\delta) J_1(\delta)$$
$$\times[(L_{-1} - L_1)\cos(\omega_m t + \phi)$$
$$+(D_1 - 2D_0 + D_{-1})\sin(\omega_m t + \phi)]. \quad (3.8)$$

Here L_n and D_n are defined by equations 3.3 and 3.4 respectively and the constant A_m represents properties of the probe and medium independent of the other parameters in the equation. Similar to modulation transfer signals, the FM lineshapes described by equation 3.8 depend critically on the ratio of the modulation frequency to the linewidth of the spectral feature. By altering the signal phase at the frequency mixer, ϕ, the beat signal can be tailored to consist of only the absorption or dispersion component or a mixture of both signals.

3.4.3 Comparing modulation transfer spectroscopy with FM spectroscopy

Figures 3.10 (a), (b) and (c) show a modulation transfer signal, an FM signal and a saturated absorption/hyperfine pumping spectroscopy signal respectively for the ^{87}Rb $F = 2 \rightarrow F'$ and ^{85}Rb $F = 3 \rightarrow F'$ transitions. These figures highlight the differences between modulation transfer spectroscopy and FM spectroscopy. The modulation transfer signal has a very flat, zero background signal. This is due to modulation transfer only taking place when the sub-Doppler resonance condition is satisfied. In contrast to this, the FM signal is observed on a sloping background, approximating to the derivative of the Doppler-broadened absorption profile. Usually, a second stage of demodulation is employed in FM spectroscopy to remove this background by amplitude modulating the pump beam. The modulation transfer signal has only one strong zero crossing for each transition, with the strongest signal always corresponding to the closed transition. This can be advantageous,

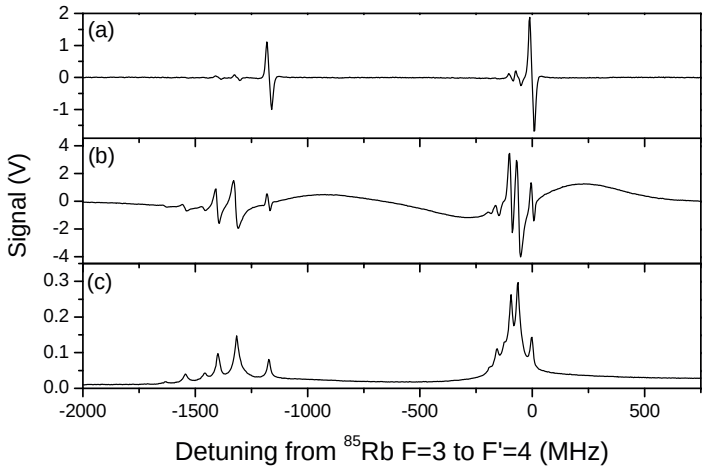

Figure 3.10: A comparison between (a) modulation transfer spectroscopy and (b) FM spectroscopy for the ^{87}Rb $F = 2 \rightarrow F'$ and ^{85}Rb $F = 3 \rightarrow F'$ transitions at a modulation frequency of 12.35 MHz. (c) The reference saturated absorption/hyperfine pumping spectroscopy signal with the Doppler background removed is included for completeness. A 10 point moving average has been applied to the data [143].

particularly in the case where there are many closely spaced hyperfine transitions, such as the ^{85}Rb $F = 2 \rightarrow F'$ transitions [143]. In contrast, the FM signal displays the same number of lines as the standard saturated absorption/hyperfine pumping spectroscopy signal. This can be an advantage when one wants to lock away from a closed transition such as when locking to a repump transition for laser cooling.

3.5 Slave Laser Setup

The simple design of the slave lasers consists of a laser diode in a collimation tube (Thorlabs LT230P-B) mounted in a temperature stabilised aluminium block. The temperature stability of these lasers was increased by approximately doubling the volume of this aluminium block compared to the old design used in [94]. Each slave laser is frequency stabilised by injecting the laser diode with $\simeq 200$ μW of light from the locked master laser. This injection light is double passed through an AOM to allow independent frequency

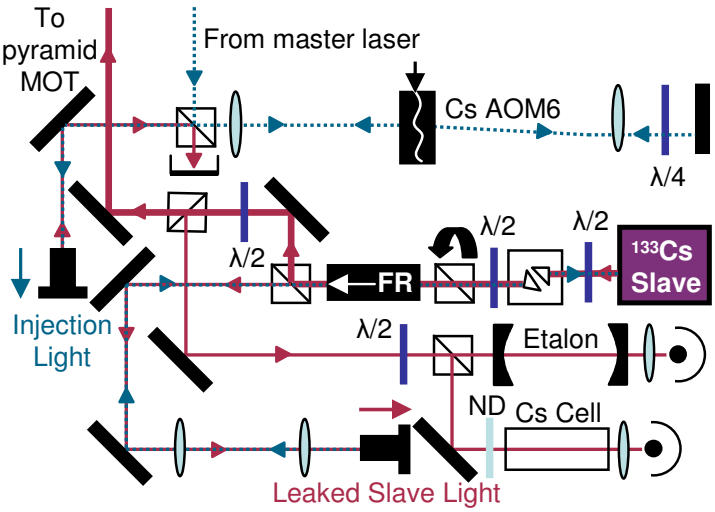

Figure 3.11: Schematic of the ^{133}Cs slave laser setup. Light from the master laser is double passed through AOM6 and aligned into one end of an optical fibre (dashed blue lines). The majority of light from the slave laser (solid red lines) is sent to the pyramid MOT, however $\simeq 3\%$ leaks through the PBS. By optimising the transmission of the leaked slave light through the fibre the alignment and beam size of the injection light from the master laser into the slave laser diode are automatically optimised. The ^{87}Rb slave laser setup is similar.

control of the pyramid cooling light (figure 3.2). In the previous optical setup the slave injection light was aligned by simply using two mirrors. In this setup a significant improvement of the slave laser stability and scan range was achieved by overlapping the injection light and leaked slave light in an optical fibre from opposite ends. This new setup is presented in figure 3.11. By simply optimising the transmission of the leaked slave light into the optical fibre using a telescope the alignment and beam size of the injection light into the slave laser diode is automatically optimised.

This setup decouples the slave injection and the pointing stability from the AOM. Changes in the beam pointing will vary the amount of injection light transmitted through the fibre, however this is easily corrected by changing the amount of RF power to AOM6. About 1 mW of the slave laser light is picked off and analysed using a home-made confocal etalon and Doppler spectroscopy. When the injection light alignment is optimised the slave lasers can scan up to $\simeq 4$ GHz.

3.6 Magnetic and RF Coils

Throughout the experimental sequence various types of copper coils are used to apply magnetic and RF fields to trap, cool and prepare the spin states of the atomic mixture. Homogeneous magnetic bias fields and magnetic field gradients are generated using a manifold of coils mounted in a coil assembly which has replaced the Ioffe-Pritchard 'baseball' magnetic trap [93, 94]. The necessary RF fields are applied from several smaller coils mounted at various positions around the cell.

3.6.1 Magnetic Field Coils

Magnetic field coil pairs were wound from square cross-section copper tubing using the method presented in [94]. These coils were secured with epoxy resin into a Tufnol epoxy glass mount (grade 10G/40) to form the coil assembly and centred around the glass cell. The coil assembly contains three coil pairs in the Helmholtz configuration and two pairs of coils in the anti-Helmholtz configuration. Coils in the Helmholtz configuration carry current in the same sense and produce the most uniform bias fields. This occurs when the coil pair axial separation equals the coil radius ($S = R$). Anti-Helmholtz coil pairs carry currents in the opposite sense and create the most uniform magnetic field gradients when $S = \sqrt{3}R$.

A cross-section through the coil assembly is presented in figure 3.12 (a). The dotted (dashed) lines in figure 3.12 mark the Helmholtz (anti-Helmholtz) condition. The coil dimensions are given in appendix C. The coils are water cooled using a barrier cooler which pumps distilled water through each individual coil. This allows currents exceeding 400 A to be applied with no adverse heating effects and enables tight magnetic confinement and large bias fields to be applied to the ultracold mixture. The coils Bias 1 and Bias 2 are connected in series to produce large bias fields. The largest bias field recorded using this setup is 1157(1) G for 425 A through Bias 1 and Bias 2 with 11.78(5) V across the coils. This field can only be applied for short times (< 10 s) to avoid excessive heating of the coils. Here the power dissipated in the coils is $\simeq 5$ kW while the maximum power dissipation of the barrier

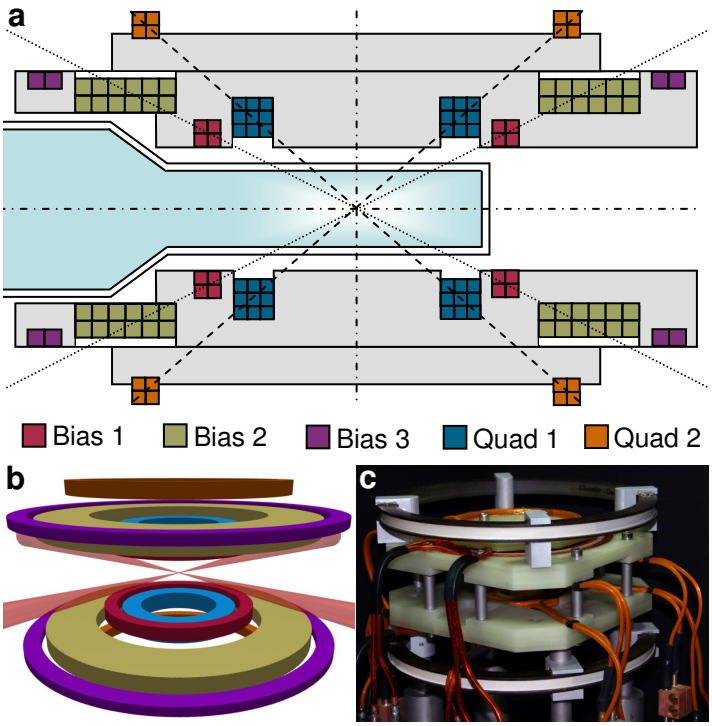

Figure 3.12: The coil assembly centred around the glass cell. (a) A cross-section through the assembly shows three Helmholtz coil pairs (Bias 1 - 3) and two anti-Helmholtz coil pairs (Quad 1, 2). The dotted (dashed) lines mark the Helmholtz (anti-Helmholtz) condition. The coil arrangement presented in (b) and (c) offers maximum optical access to the glass cell. Each coil consists of multiple turns of square cross-section copper tubing and is glued into a circular recess machined into the Tufnol mount.

cooler is just 2 kW! Bias 3 is used to make small fast ($\sim$ 1 ms) changes to the bias field as each coil consists of just two turns of wire. The Quad 1 coils produce the trapping magnetic quadrupole potential used in this experiment while Quad 2 provides the magnetic field gradient for the science MOT.

When designing the coils the field from each coil pair was modelled using a Mathematica code that summed the field contribution from each individual wire turn. Before centering the assembly around the glass cell the axial magnetic field for each coil pair was characterised for a 100 A current by axially translating a calibrated Hall probe. Tables 3.2 and 3.3 present the target design and measured magnetic field properties of the Helmholtz and anti-

	Bias Field (G/A)		Field Curvature (G/cm^2/A)	
Coil	Target Design	Measured	Target Design	Measured
Bias 1	0.913	0.913(2)	0.001	0.003(1)
Bias 2	1.830	1.848(3)	0.0005	0.0011(6)
Bias 3	0.245	0.261(2)	0.0028	0.0032(2)

Table 3.2: Theoretical and measured magnetic field properties for the Helmholtz coils in the assembly.

	Field Gradient (G/cm/A)		Third Derivative (G/cm^3/A)	
Coil	Target Design	Measured	Target Design	Measured
Quad 1	0.966	1.001(7)	0.001	0.005(8)
Quad 2	0.105	0.106(9)	0.001	0.003(2)

Table 3.3: Theoretical and measured magnetic field properties for the anti-Helmholtz coils in the assembly.

Helmholtz coils respectively. This good agreement between the desired and real properties of the coil pairs in these comparisons reveals that the results of our coil winding process can be accurately predicted. Figure 3.12 (a) shows that the Bias 3 coil pair does not lie in the optimum Helmholtz configuration. The Bias 3 coils were positioned closer to the cell to allow magnetic transport coils with an inner separation of 8.6 cm [151] to be used with this assembly in future experiments. If this change is implemented the Quad 2 coils and outer mount layers will be removed. Despite the non-optimal position the curvature of the Bias 3 magnetic field is just 0.0032(2) G/cm^2/A.

In addition to the coil assembly three pairs of magnetic shim coils described in [94] produce bias fields which allow fine tuning of the magnetic field zero position in three dimensions in the glass cell. Also a single coil consisting of 16 turns of 0.71 mm diameter wire was wound and secured on top of the assembly 46 mm away from the centre of the cell. The current in this coil can be switched on or off in just 600 μs and it is used to generate a $\sim$ 3 G field during the optical pumping stage.

3.6.2 RF Coils

To evaporatively cool and prepare the atomic mixture into specific magnetic spin states RF is applied to the ultracold mixture at various experimental phases via two new coils wound from 0.71 mm diameter copper wire. To evaporatively cool the atoms an oscillating voltage is applied to a 36×45 mm rectangular coil consisting of 2 turns positioned in the plane of the cell 20 mm from its south face (see the compass defined on figure 3.13). A 10 Ω high power (3 W) resistor is connected in series with this coil. The RF coil used for adiabatic rapid passage (section 5.6) is a 3 turn 26 mm square coil located in the plane of the cell 45 mm away from the east face of the cell. The coil was connected in parallel with a 22 nF capacitor to create an LCR circuit with a resonant frequency at a desired value of $\simeq$ 1.5 MHz. This allows a maximum RF power to be applied to the atoms for efficient transfer without the need for costly high power amplifiers.

3.7 Double MOT System

Ultracold atomic mixtures of ^{87}Rb and ^{133}Cs are collected in a UHV glass cell using a two-species 6 beam MOT. This is fed from a two-species pyramid MOT. The vacuum apparatus used in the double MOT system is described elsewhere [93, 94]. To integrate the optical dipole trap into the setup the alignment of the double MOT apparatus has changed significantly. The double MOT setup is shown in figure 3.13.

3.7.1 Pyramid MOT

The pyramid MOT provides a robust and compact ultracold atom source and has been used effectively in both single and two-species experiments [152, 153]. The inverted pyramid mirror is truncated at the apex to leave an aperture $\simeq 2.4 \times 3.0$ mm. By aligning a single circularly polarised beam onto the mirror assembly three orthogonal beam pairs with the polarisations of a standard 6 beam MOT are generated. This allows the two-species pyramid MOT to be operated by simply aligning a single beam comprised of cooling

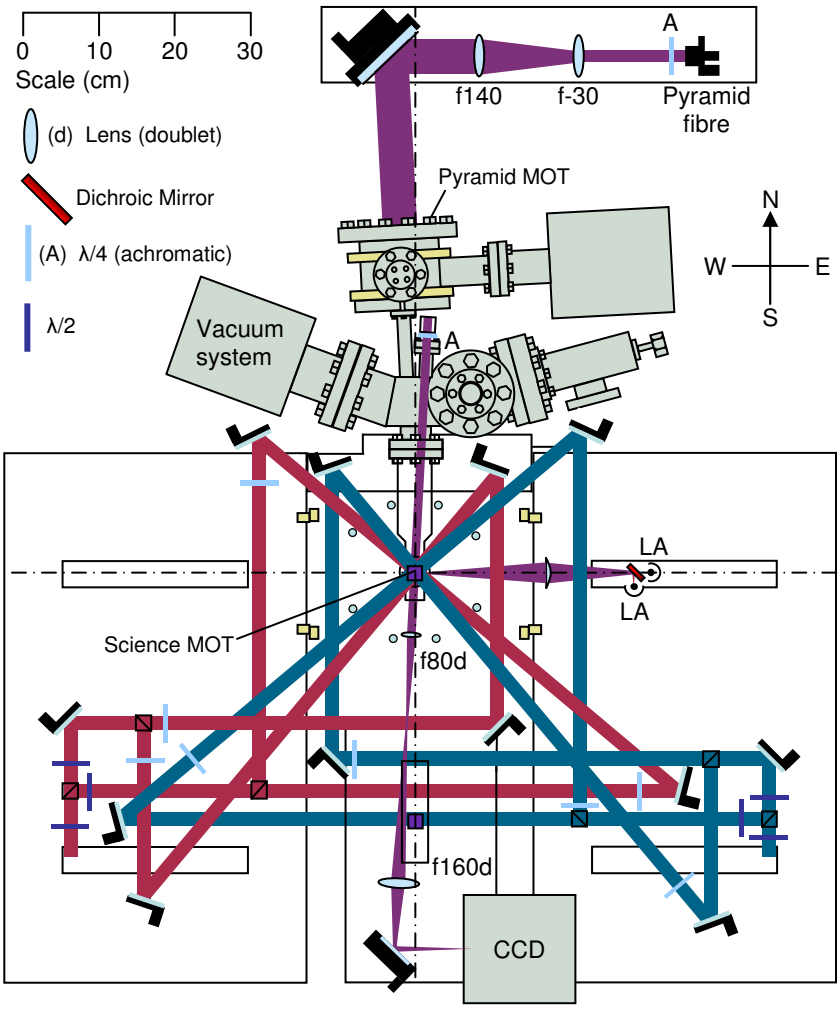

Figure 3.13: Schematic view of the double MOT system. The pyramid MOT uses a single beam containing cooling and repump light for both species and feeds the two-species science MOT in the UHV glass cell. Independent ^{87}Rb (red) and ^{133}Cs (blue) science MOT beams containing both cooling and repump light are brought up to the horizontal plane of the cell using periscopes. The purple squares show where the combined up/down MOT beams pass through this plane. The MOT fluorescence for both species is detected using a dichroic mirror and large area photodiodes. A probe beam containing light for both species is used for absorption imaging onto a CCD camera.

and repump light for both ^{87}Rb and ^{133}Cs.

Light from the pyramid MOT fibre contains 48.2(1) mW (34.0(1) mW) of

cooling light and 3.6(1) mW (3.4(1) mW) of repump light for ^{87}Rb (^{133}Cs). The light is collimated to a $1/e^2$ radius of 3.5(1) mm (using a Thorlabs F810APC-780 collimator) and passes through an achromatic $\lambda/4$ plate (Casix WPA1212-700-1000nm). A telescope consisting of lenses with -30 mm and 140 mm focal lengths expands the beam by a factor of $\simeq 5$ before the light is reflected by a 100 mm diameter mirror, through an AR coated viewport, and is incident on the pyramid. A pair of water-cooled anti-Helmholtz coils produce the required magnetic quadrupole field of 7.8(1) G/cm. Two shim coils are used to adjust the position of the B-field zero and hence the centre of the pyramid MOT in the N-S and E-W directions. By positioning the MOT centre directly over the hole in the pyramid apex the absence of a retro-reflected axial MOT beam results in an optical pressure imbalance. This radiation pressure causes atoms to be pushed from the pyramid chamber into the UHV glass cell to be collected by the science MOT. The optimisation of the pyramid MOT is presented in section 4.1.

The flux of ^{87}Rb and ^{133}Cs atoms from the pyramid MOT is controlled via the current sent to the alkali metal dispenser for each species. Typically the ^{87}Rb (^{133}Cs) dispenser was run at 3.2 A (2.5 A). The flux of atoms has a velocity of $\simeq 10$ m/s [152] and travels 36 cm to the science MOT. To maximise the flux and account for the atoms falling under gravity during this transit time the pyramid MOT beam is angled upwards at $\simeq 1^\circ$ to the horizontal. This was done by aligning the beam from the 100 mm diameter mirror such that the light passing through the pyramid aperture hit the south face of the cell 7 mm above the cell centre. This also ensured that the light transmitted through the pyramid aperture did not contribute optical pressure to the science MOT.

3.7.2 Science MOT

The two-species science MOT is located at the centre of the UHV glass cell and collects the flux of ultracold ^{87}Rb and ^{133}Cs atoms from the pyramid MOT. The output light from the ^{87}Rb (^{133}Cs) science MOT fibre contains 38.5 mW (31.0 mW) of cooling and 5.01 mW (3.2 mW) of repump light. The light from both fibres is collimated to $1/e^2$ radii of 3.5(1) mm using commercial collimators (Thorlabs F810APC-780 and F810APC-842 for ^{87}Rb

and ^{133}Cs respectively). Telescopes made of 80 mm and 125 mm focal length lenses expand the beams by a factor of $\simeq 1.6$. The light for both species is split using species specific cemented zero order half waveplates with 20 mm square polarising beam-splitter (PBS) cubes. One third of the light from each fibre is combined on a non-polarising beam splitter cube to produce two linearly polarised beams containing light at 780 nm and 852 nm. These combined beams form the up-down MOT beams and counter-propagate at 4° to the vertical axis. A true zero order quarter waveplate for ^{87}Rb (^{133}Cs) produces the required circular polarisation for the up (down) MOT beam. The remaining two thirds of the light is split into two pairs of counter-propagating beams for each species. These horizontal MOT beams for ^{87}Rb (^{133}Cs) are aligned with respect to the N-S axis at angles of $-46.9(5)°$ and $+43.1(5)°$ ($-41.3(5)°$ and $+48.7(5)°$). The separate horizontal MOT beams for each species allows both MOTs to be independently optimised via the polarisation, alignment and intensity of each beam.

The ^{133}Cs beam powers and polarisations were set to separate the ^{87}Rb and ^{133}Cs MOT centres by ~ 2 mm to avoid the light-assisted interspecies inelastic collisions observed between the two overlapped MOTs [154]. This allowed the unsuppressed loading of both MOTs without implementing the displaced MOT technique before overlapping both species in the CMOT phase. The anti-Helmholtz coil pair Quad 2 produced the 10.3(1) G/cm magnetic field gradient required for the MOT. The science MOT shim coils were used to locate both MOTs into an optimum loading position. The optimisation of the science MOT is presented in section 4.2. Typically up to 3×10^8 ^{87}Rb atoms are loaded into the science MOT in 30 s. The number of ^{133}Cs atoms loaded is controlled and stabilised to be between 5×10^5 and 3×10^8 by monitoring the science MOT fluorescence and actively controlling the ^{133}Cs repump light level via the RF amplitude sent to AOM5. The ^{133}Cs science MOT servo is presented and discussed in section 3.9.3.

3.8 The Hybrid Trap

The 'hybrid' trapping potentials used in this experiment consist of the sum of magnetic, optical and gravitational components. Hybrid traps have been suc-

cessfully demonstrated in several experiments [4, 83, 133, 155] and combine the advantages of quadrupole and optical traps while avoiding their individual weaknesses. The optical component of our trapping potentials consists of two 1550 nm beams derived from a 30 W fibre laser (IPG ELR-30-LP-SF).

3.8.1 Dipole Trap Setup

The beam output from the fibre laser head has a waist of 0.55(1) mm and a Rayleigh range of 650(20) mm. A telescope consisting of -50 mm and 100 mm singlet lenses (Thorlabs LA1509-C-BK7 and LC1715-C-N-BK7 respectively) increases the beam sizes at the AOMs to $1/e^2$ radii of 1.26(1) mm and 1.23(1) mm for beams 1 and 2 respectively to ensure high diffraction efficiencies. Half waveplates (Thorlabs WPH502) and PBS cubes (Linos G335756000) are used to clean the output polarisation and split the light into two beams of equal power. Typically each beam contains $\simeq$ 13 W before the AOM. Six steering mirrors (Linos G340773000) and used to guide the light around the setup. Home made beam dumps constructed from anodised stainless steel block the transmitted zero order beams from the AOMs and the dipole beams after they have passed through the glass cell, see figure 3.14. Operating with such high powers needs a clean environment as optical components are easily damaged by dust particles being burned onto them. Damaged optics can change the Gaussian beam profiles and modify the shape of the optical potential. To avoid these unwanted changes all optical surfaces exposed to the high power dipole beams are thoroughly cleaned at least once a week.

AOMs are used to servomechanically stabilise and vary the power in the dipole beams. Each beam passes through a water cooled Isomet AOM (M1135-T50L-3) driven by a water cooled 50 MHz 7 W Isomet fixed frequency driver-amplifier (531B-7-50) with a diffraction efficiency of 82(1) %. To protect the AOM driver a home-made circuit limits the maximum applied control voltage to 1 V. During the initial evaporative cooling stages in the dipole trap the amount of RF power to the AOMs is reduced to decrease the amount of light diffracted into the first order beams. This change causes some displacement of the first order beam from each AOM. Investigations of

the pointing stability after the AOMs reveal that for a $\Delta V_{\text{control}} = 1\,V$ change the deflection angle is 63(9) μrad which corresponds to a shift of 7(1) μm of each beam waist at the centre of the glass cell.

Pointing instabilities could be reduced by using the AOM in the 'double pass' configuration. Here single passed light is sent back through the AOM and receives a second deflection in the opposite direction resulting in zero total deflection. This method has been used in other experiments to reduce dipole trap beam deflections by a factor of 6 to 400 μrad [156]. A second method to improve the beam pointing stability during intensity ramps delivers a second RF frequency to the AOM. As the power of the first main RF frequency is reduced the power of a second frequency is increased to keep the total power delivered to the AOM crystal constant. This technique can reduce deflection angles from AOMs by a factor of 10 to 30 μrad [157].

The AOMs used in this work produce small deflection angles and total deflections of just $\simeq 11$ % of the beam waists at the trap centre. Due to this it was deemed unnecessary to implement a corrective technique to reduce the beam deflection further.

The servo circuit used to stabilise and control each dipole beam is shown in figure D.1 in appendix D. A photodiode (Thorlabs FGA10) monitors the power in each beam and provides feedback to the servo circuit ($\text{I}_{\text{I/P}}$ in figure D.1). To ensure that the photodiodes are not saturated at full power a beam sampler (Thorlabs BSF-10-C1) and neutral density filters (Comar 40 GN 12) are used. The servo photodiode for beam 1 is positioned after the glass cell whereas the servo photodiode for beam 2 is positioned before the glass cell. This configuration allows small adjustments to the alignment of beam 2 to be made when optimising the crossed dipole trap alignment without misaligning the beam 2 servo photodiode.

Dipole beams 1 and 2 are focussed using 200 mm focal length doublet lenses (Thorlabs AC254-200-C) to waists of 65(4) μm and 61(1) μm respectively. These lenses are mounted in translating mounts (Thorlabs LM05XY) which greatly facilitate the fine tuning of the alignment of each dipole beam in the y and z-directions (see figures 3.14 and 5.3).

Due to the difference in the polarisabilities of ^{87}Rb and ^{133}Cs at 1550 nm

[158], the optical potential is $\sim 1.4\times$ deeper for ^{133}Cs than ^{87}Rb and is therefore suitable for the sympathetic cooling of ^{133}Cs. The crossed dipole trap setup is shown in figure 3.14. To limit Majorana losses during and after the transfer into the hybrid potential both dipole beams were aligned to be $\simeq$ 80 μm below the centre of the unbiased quadrupole potential. The character of the hybrid potential depends on the position with respect to the trap centre, $\delta = \sqrt{x^2 + y^2 + z^2}$, and the vertical offset of the dipole beams below the centre of the unbiased quadrupole field, z_0 (in our setup $z_0 \simeq 80$ μm). When $\delta \ll z_0$ the potential is harmonic in nature, however when $\delta \gg z_0$ the potential is linear. The optimised alignment of the two dipole beams is crucial to the shape and performance of the hybrid potential and is discussed in section 3.8.3 and chapter 5. In this experiment the versatile hybrid trap

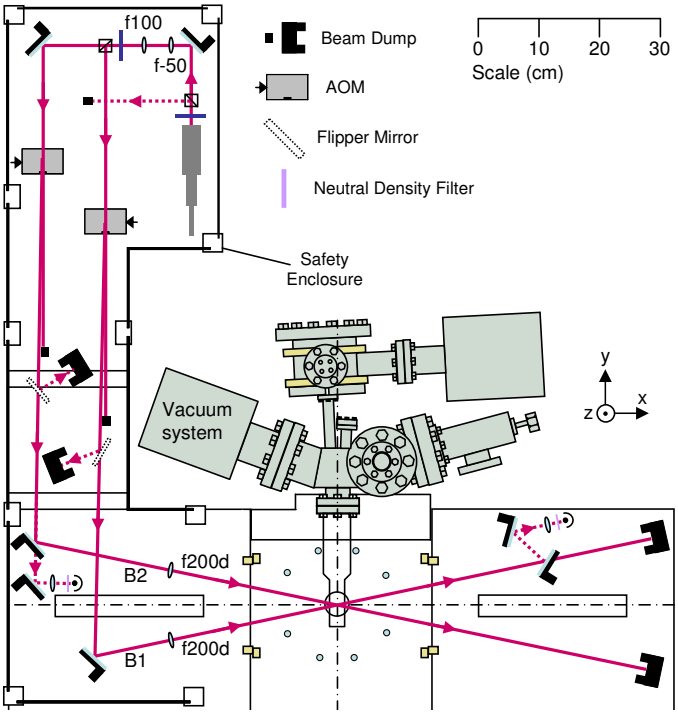

Figure 3.14: Schematic of the optical dipole trap setup. The fibre laser output is split into two beams labelled beam 1 (B1) and beam 2 (B2) which cross at an angle of 22°. The intensity of each beam is monitored on a photodiode and servomechanically controlled and stabilised using an AOM. Mechanical flipper mirrors (Thorlabs MFF001) act as shutters by redirecting both beams away from the cell. The entire setup is housed in an additional safety enclosure on the optical table.

is used in two configurations. The 'loading trap' is optimised to capture the ^{87}Rb and ^{133}Cs from the quadrupole trap at the highest possible phase-space densities while the 'levitated trap' is optimised for the final stages of evaporative cooling.

3.8.2 The Loading Trap

Once Majorana spin-flip losses start to limit the efficiency of any further cooling in the quadrupole trap the atomic mixture is transferred into the loading trap. The ^{87}Rb and ^{133}Cs atoms in the low field seeking $|1,-1\rangle$ and $|3,-3\rangle$ states respectively are loaded via elastic collisions by simply reducing the magnetic field gradient to 29.0 G/cm, just below the 30.5 G/cm (31.1 G/cm) required to exactly levitate ^{87}Rb (^{133}Cs). This transfer results in a large gain in phase-space density for both species and is analogous to the use of a dimple potential [12]. Adiabatic expansion of the trap volume cools the cloud in the quadrupole potential and elastic collisions transfer some atoms into the tighter harmonic optical potential. The remaining atoms are lost from the quadrupole trap reservoir, removing energy in the process. When the atomic mixture is in the $|1,-1\rangle$ and $|3,-3\rangle$ low field seeking states two hybrid potentials have been used to trap the mixture. One uses a single dipole beam trap and the other uses the crossed dipole trap.

Single Beam Trap

A single beam hybrid trap is realised by offsetting the centre of the dipole beam from the field zero of the quadrupole potential [133]. This alignment avoids Majorana losses in the hybrid potential while the offset quadrupole field provides axial confinement along the dipole beam. This approach realises three-dimensional confinement without a crossed dipole trap but is limited to low field seeking states only.

Crossed Dipole Trap

A second dipole beam aligned to cross the single beam trap at 22° forms a crossed dipole trap that can confine all spin-states and allows the magnetic

Loading	U (μK)	ν_x (Hz)	$\nu_{y,z}$ (Hz)
^{87}Rb	180	135	675
^{133}Cs	250	127	635

Table 3.4: Trap depths and axial and radial trap frequencies for the crossed loading trap. The parameters are for ^{87}Rb (^{133}Cs) atoms in the $|1,-1\rangle$ ($|3,-3\rangle$) state in a loading potential produced using 6 W in each dipole beam and a magnetic field gradient of 29 G/cm.

field to become a free parameter. The frequency of each dipole beam is shifted by $\pm$50 MHz respectively using AOMs to avoid standing wave effects.

When in the $|1,-1\rangle$ ($|3,-3\rangle$) state for ^{87}Rb (^{133}Cs) respectively the magnetic field gradient provides an attractive confining potential that adds to the existing optical confinement. The essential features of this trapping potential are presented in figure 3.15. Along each beam the hybrid potential is the sum of the harmonic trap obtained from the offset quadrupole field with the dimple optical potential superimposed at the centre. In the horizontal plane, away from the dimple region, the trap potential increases linearly in all directions to values > 1000 μK. The trap depth is therefore entirely determined by the potential in the vertical z-direction and is nearly constant on the lower side of the trap due to the near cancellation of gravity. On the upper side of the trap a potential gradient of $\sim 2g$ exists due to the addition of gravitational and magnetic potentials. Hot atoms are lost vertically downwards in the direction with the lowest trap depth. The trap depths and axial and radial trap frequencies for the crossed loading trap are summarised in table 3.4.

3.8.3 The Levitated Trap

At the heart of our experiment is the levitated crossed dipole trap, it is in this potential that the majority of our experiments are performed (figure 3.16). To transform the hybrid potential into the levitated trap a bias field of +22.4 G offsets the quadrupole field zero position to below the crossed dipole trap such that high field seeking states are levitated. In addition

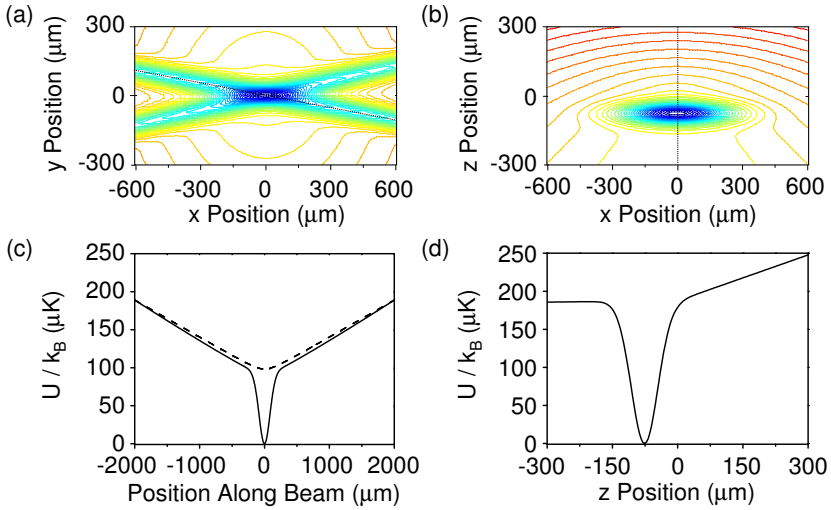

Figure 3.15: The loading trap potential shown for ^{87}Rb atoms in $|1,-1\rangle$. The power of both beams is 6 W and the magnetic field gradient is 29 G/cm. Contour plots of the trap potential in (a) $x-y$ plane intersecting the potential minimum and (b) the $x-z$ plane, see axes labels on figure 3.14. Cross-sections through the potential minimum along one of the beams (c) and vertically (d). The crossed dipole trap is positioned $\simeq$ 80 μm below the field zero of the quadrupole potential resulting in additional magnetic harmonic confinement along the beams. The purely magnetic contribution is shown as the dashed line in (c).

the ^{87}Rb and ^{133}Cs atoms are transferred into the high field seeking $|1,+1\rangle$ and $|3,+3\rangle$ states respectively via adiabatic rapid passage, see section 5.6. For these states the magnetic field is anti-trapping and opposes the optical confinement. This change allows atoms to be evaporated horizontally along the dipole beams and results in the trap depths decreasing by a factor of 2 for both species. The trap depths and axial and radial trap frequencies for the initial levitated dipole trap are presented in table 3.5.

It is in this potential that the atomic mixture is cooled to high phase-space densities via efficient evaporative and sympathetic cooling for ^{87}Rb and ^{133}Cs respectively. For dipole beam powers $\lesssim$ 100 mW the nature of the evaporation surface in the trap can be tuned using the applied magnetic field gradient. This is highlighted in figure 3.17 which shows how the horizontal and vertical trap depths vary with the applied magnetic gradient for ^{87}Rb in the $|1,+1\rangle$ state. Here the beam powers are 100 mW and the bias field is

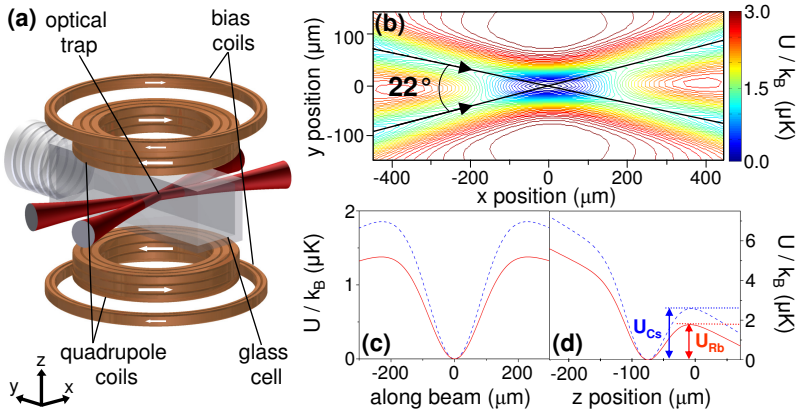

Figure 3.16: (a) Geometry of the levitated crossed dipole trap. (b-d) Typical trapping potential employed towards the end of the evaporation sequence (the power of both beams is $\simeq$ 100 mW, the magnetic field gradient is 35 G/cm and the bias field is 22.4 G). The contour plot in (b) shows the potential for ^{87}Rb in the $|1,+1\rangle$ state. The cut along z in (d) highlights the tilting of the trap.

+22.4 G. This figure shows that the trap depth along the beam, which is the shallowest part of the potential in the horizontal plane, is almost constant as the magnetic gradient is changed. In contrast, the vertical trap depth varies greatly and may be tuned to be greater or less than the horizontal trap depth using the magnetic field gradient. In this manner the figure is split into two regions with an approximate crossover gradient for this example at 37 G/cm. The practicality of the levitated trap stems from the existence of both regions.

For gradients less than the crossover gradient evaporation occurs horizon-

Levitated	U (μK)	ν_x (Hz)	$\nu_{y,z}$ (Hz)
^{87}Rb	90	132	675
^{133}Cs	125	124	635

Table 3.5: Trap depths and axial and radial trap frequencies for the initial levitated trap. The parameters are for ^{87}Rb (^{133}Cs) atoms in the $|1,+1\rangle$ ($|3,+3\rangle$) state in a levitated potential produced using 6 W in each dipole beam, a magnetic field gradient of 29 G/cm and a bias field of 22.4 G.

tally along the beams and can be achieved by decreasing the beam powers. This method also results in a decrease in the trap frequencies and hence the collision rate. This is detrimental to evaporative cooling although it is useful in circumstances where three-body loss rates are high, this is discussed in chapter 6. For gradients greater than the crossover gradient evaporation occurs in the vertical direction due to the lower trap depth (figure 3.17 (c)). This occurs because as the gradient is increased gravity is over compensated and the residual force (magnetic minus gravity) eventually overcomes the downwards confinement of the optical potential. The hot atoms then escape upwards; this effect is referred to as 'trap-tilting' [83] and allows the trap depth to be reduced while leaving the trap frequencies largely unchanged. In this region evaporation can be performed by either reducing the beam powers or by increasing the magnetic field gradient. Figure 3.16 (b) and (c) show horizontal and vertical cuts respectively through the levitated trap potential for ^{87}Rb in the $|1, +1\rangle$ state. Here two values of the gradient are plotted, one at 30.5 G/cm, exactly levitating the trap (dashed line) and the other at 38.0 G/cm, tilting the trap (solid line).

When perfectly aligned the untilted, levitated trap is almost symmetric about the potential minimum as the magnetic and gravitational forces cancel on either side of the dipole potential. However, if misalignment results in the crossed dipole trap not being directly below the unbiased field zero of the quadrupole trap the symmetry in the horizontal plane is broken. The resulting offset in the optical and magnetic potentials means that the levitated trap depth is now lowest along just two of the four beams. This significantly reduces the evaporation surface and is undesirable for efficient evaporative cooling. The alignment of the dipole beams is presented in chapter 5.

3.9 Diagnostics

To probe and measure the properties of ^{87}Rb and ^{133}Cs atoms this experiment employs various complementary methods described in detail below. Briefly, absorption imaging measures the atom number and provides information on the spatial distribution of the atomic cloud. However such probing destroys the atomic sample and requires many iterative experimental runs to be per-

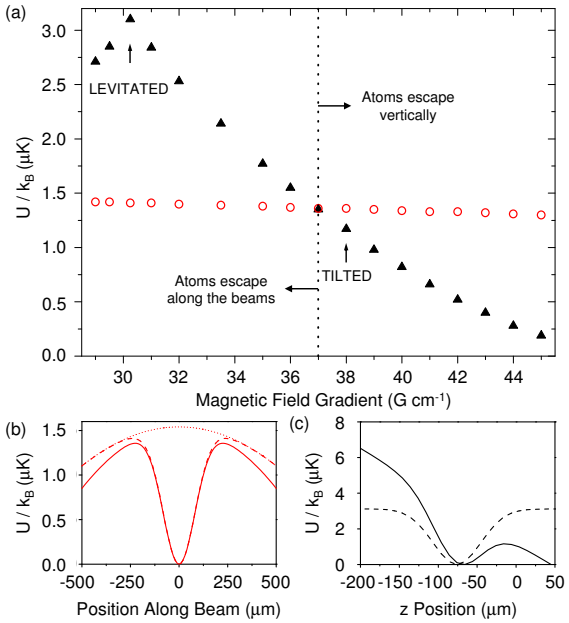

Figure 3.17: Tuning the depth of the levitated crossed dipole trap using the applied magnetic field gradient. (a) The trap depths for ^{87}Rb atoms in the $|1, +1\rangle$ state along the beams (open red circles) and in the z-direction (closed black triangles) as a function of the magnetic field gradient. Each beam contains 100 mW and the bias field is 22.4 G. Cross-sections through the potential minimum (b) along one of the beams and (c) vertically are shown for the levitated (dashed) and tilted (solid) potentials indicated.

formed. In contrast, fluorescence detection is a non-destructive technique which allows the atom number to be continuously monitored. In addition to these two methods a magnetic field gradient applied during a time-of-flight can be used to perform Stern-Gerlach separation of different magnetic sublevels.

3.9.1 Absorption Imaging

To probe the ^{87}Rb - ^{133}Cs mixture the trap is switched off and resonant absorption images are captured for both species in a single iteration of the experiment using a frame transfer CCD camera (Andor iXon 885) [154]. The two-species absorption imaging scheme is described in detail in [93].

In brief a $\pm 2.7(1)$ G field is switched on along the N-S axis such that the circularly polarised probe beam drives either σ^+ or σ^- transitions into a stretched state, *e.g.* σ^- transitions into $|1,-1\rangle$ for ^{87}Rb. Once in the stretched state the atoms continuously absorb the probe light creating a shadow in the imaged laser beam profile allowing properties such as atom number, temperature and density to be calculated. For each field direction the sign of the probe detuning must be reversed to account for the Zeeman shift and ensure that the probe light remains on resonance.

Absorption imaging can detect atoms in both hyperfine ground states by firing a 0.1 ms pulse of repump light before the probe pulse. An absence of the repump pulse results in just the upper hyperfine ground state being probed. The probe beam intensities are set to $I_{\text{probe}} \simeq 0.1 I_{\text{sat}}$ for both species to ensure that intensity fluctuations do not have a large effect on the measured peak absorption.

To measure the properties of an atom cloud via absorption imaging three 10 μs probe pulses are recorded in quick succession. The three images consist of

$$I_1 = \text{Probe beam + Atoms + Background},$$

$$I_2 = \text{Probe beam + Background},$$

$$I_3 = \text{Background only},$$

and are used to calculate the optical depth (OD) measured on each camera pixel according to

$$\text{OD} = \ln\left(\frac{I_2 - I_3}{I_1 - I_3}\right). \tag{3.9}$$

By fitting a Gaussian profile to the optical depth distribution the $e^{-1/2}$ widths of the cloud in the image plane (σ_x and σ_z) can be measured. The peak optical depth (OD_{pk}) occurs at the centre of the atom cloud ($x = z = 0$) and can be combined with the clouds widths in the image plane to calculate the atom number using

$$N = \frac{4\pi^2 \text{OD}_{\text{pk}} \sigma_x \sigma_z}{3\lambda^2}. \tag{3.10}$$

The derivation of this equation is presented in appendix B. From the total nuber of trapped atoms, the peak number density is calculated as

$$n_{\mathrm{pk}} = N\omega_x\omega_y\omega_z\left(\frac{m}{2\pi k_{\mathrm{B}}T}\right)^{3/2}. \tag{3.11}$$

As the optical depth distributions along the imaged axes are equal to the number density distributions (σ_x and σ_z) the temperature of the atom cloud along these imaged axes is given by

$$T_{x,z} = \frac{m\omega_{x,z}^2\sigma_{x,z}^2}{k_{\mathrm{B}}}, \tag{3.12}$$

This equation allows the axial and radial temperatures in the levitated crossed dipole trap to be measured by taking one absorption imaging sequence provided that the axial and radial trap frequencies are known. If the trap frequencies are unknown multiple absorption images recorded after different times-of-flight can measure the cloud expansion and be used to calculate the axial and radial temperatures using equation 2.48.

When imaging a stretched state with the 'wrong' polarisation of light, *e.g.* σ^- transitions for atoms initially in the $|1,+1\rangle$ state for ^{87}Rb, closed transitions are not initially driven. Here, after the repump pulse transfers the atoms into the $F = 2$ ground state, the probe light needs to pump the atoms across a maximum of five transitions into the closed transition of $|F = 2, m_F = -2\rangle \rightarrow |F' = 3, m_{F'} = -3\rangle$. In this case the relative strength of the weakest transition ($|2,+2\rangle \rightarrow |3,+1\rangle$) is 1/15 of the strongest transition ($|2,-2\rangle \rightarrow |3,-3\rangle$) [1]. In contrast to this case when imaging atoms in $|1,-1\rangle$ state the probe light only needs to drive a maximum of three σ^- transitions into the closed transition. Here the relative strength of the weakest transition ($|2,0\rangle \rightarrow |3,-1\rangle$) is 2/5 of the strongest transition ($|2,-2\rangle \rightarrow |3,-3\rangle$) [1]. This example shows that to accurately image atoms in a stretched state with the 'wrong' polarisation requires more numerous and less probable transitions. For identical 10 μs pulse lengths this results in a ~ 5 % lower optical depth being measured as shown in the absorption images of figure 5.8. In addition to the changing transition strengths the different Landé g-factors of the ground and excited states result in the resonance frequencies of neighboring transitions differing by 0.63(2) MHz (0.57(2) MHz) for ^{87}Rb (^{133}Cs) at a field of 2.7(1) G.

3.9.2 Fluorescence Detection

Fluorescence detection of the MOT light for each species allows the number of atoms loaded into the MOT to be monitored and calculated. This nondestructive diagnostic tool is useful during optimisation and in monitoring the performance of the apparatus. A 28 mm diameter 80 mm focal length lens captures a fraction of the solid angle of the MOT fluorescence and focuses the light onto a pair of large area photodiodes (Thorlabs DET36A). A dichroic beam splitter allows the fluorescence from the ^{87}Rb and ^{133}Cs MOTs to be measured simultaneously. The light induced current from each photodiode produces a voltage across a 1 MΩ oscilloscope input resistance which is directly proportional to the atom number. The constant of proportionality used to calculate the atom number from the fluorescence voltage is discussed in appendix B.

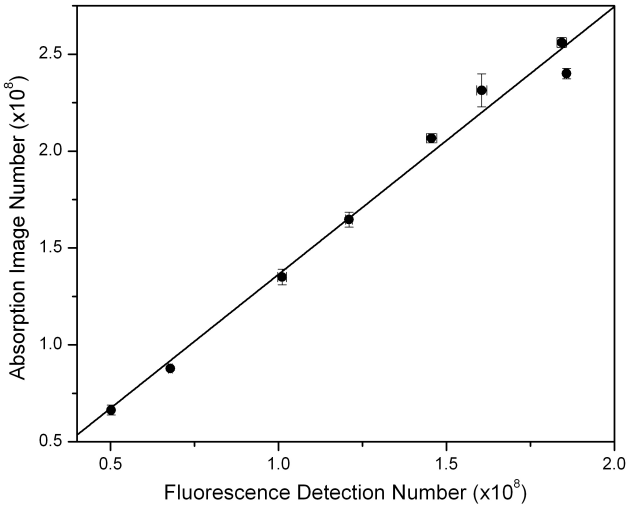

Figure 3.18: A comparison between the ^{87}Rb atom number measured in the magnetic trap via fluorescence detection and absorption imaging for identical fluorescence voltages loaded into the MOT. A linear fit to the data gives $N_{\mathrm{AI}} = 1.38(4) \times N_{\mathrm{Fluor.}} - 2(3) \times 10^6$.

Figure 3.18 shows a comparison between the ^{87}Rb atom number loaded into the magnetic trap measured via fluorescence detection and absorption imaging. The atom number was measured using fluorescence detection by recapturing the atoms from the magnetic trap into the MOT. This method assumes that the MOT recapture is 100% efficient. These data show that fluorescence

detection can approximate the real atom number to within $\simeq 40\%$ and is a useful nondestructive diagnostic tool. By using fluorescence detection and recapturing atoms in the science MOT after various stages of the experiment *relative* atom numbers can be accurately measured.

3.9.3 Selective control of the ^{133}Cs MOT number

The fluorescence signal from the ^{133}Cs science MOT is monitored using a large area photodiode and used to servo the number of ^{133}Cs atoms loaded. A PI servo circuit [159], shown in figure D.2, is used to stabilise the ^{133}Cs science MOT atom number and can selectively control the number between 5×10^5 and 3×10^8 atoms. The control output of the circuit is applied to the AOM attenuator which tunes the ^{133}Cs repump light intensity. In the absence of repump light atoms will decay into the dark lower hyperfine ground state and be lost from the MOT. Figure 3.19 shows shot-to-shot fluctuations in both the ^{133}Cs MOT fluorescence (open circles) and the ^{133}Cs atom number (closed circles) for both a timed MOT load and active control using the servo circuit. The ^{133}Cs atom number was measured after loading the magnetic trap, fluctuations introduced during the loading cannot be address by changing the MOT load. In figure 3.19 measurement numbers 1-20 are performed using a 2.5 s timed MOT load and give $6.5(2) \times 10^6$ atoms with a standard deviation of 8.3×10^5. Measurements 21-40 are performed using active control from the ^{133}Cs MOT servo and lead to $5.99(5) \times 10^6$ atoms being loaded with a standard deviation of 2.3×10^5. The inset to this figure shows a typical servomechanically controlled MOT load. These data show that active control of the ^{133}Cs MOT fluorescence signal significantly reduces shot-to-shot fluctuations in the ^{133}Cs atom number loaded into the magnetic trap.

3.9.4 Stern-Gerlach Separation

In order to spatially separate atoms in different magnetic sublevels the technique of Stern-Gerlach spectroscopy is employed. This technique is performed by switching off the confining potential and allowing the atoms to

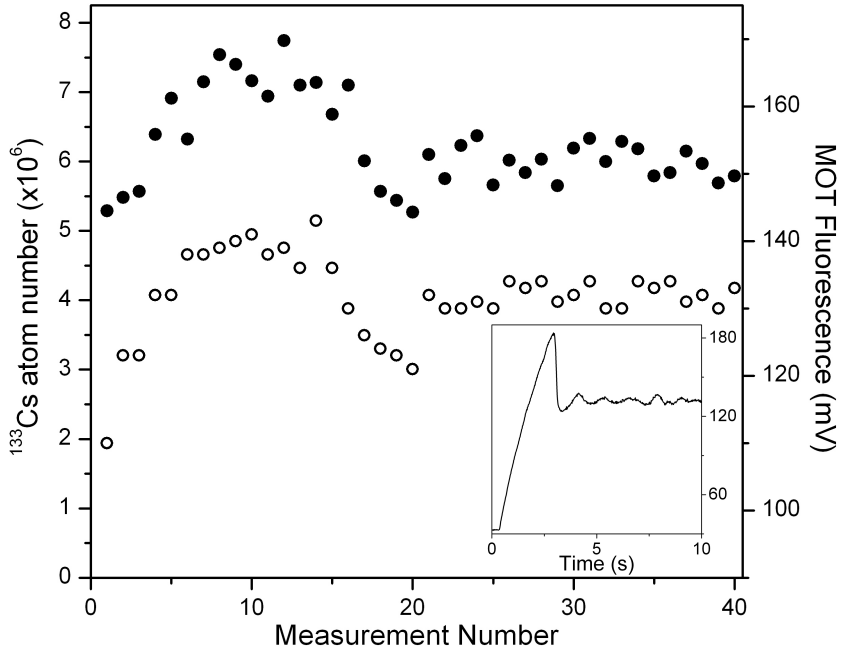

Figure 3.19: The full ^{133}Cs MOT fluorescence signal (open circles) and atom number (closed circles) loaded into the magnetic trap. Measurements 1-20 are for a 2.5 s timed load while measurements 21-40 use active control of the MOT fluorescence signal to selectively load and stabilise the atom number. The atom number was recorded after loading the magnetic trap, during which additional fluctuations limit the atom number stability. The inset shows a typical servomechanically controlled MOT load.

move freely in a 29 G/cm magnetic field gradient for 14 ms. The magnetic gradient is then switched off for a further 5 ms free time-of-flight before an absorption image is taken. Once the different magnetic sublevels have been separated a single absorption image can probe the individual clouds simultaneously. Images recorded using this method for ^{87}Rb in the $F = 1$ hyperfine ground state can been seen in section 5.6.

3.10 Experimental Control

To operate the experiment effectively precise control of the sequence and timing of experimental changes is critical. These control systems are described in detail elsewhere [93, 94]. Briefly this control is achieved using a 'LabVIEW'

computer program via three National Instruments interface boards:

- A combined 8 analogue, 8 digital TTL, channel input/output data acquisition board (PCI-6713) controls variable device drivers (*e.g.* the quadrupole trap current set-point) and monitors the Andor camera response.
- A 32 channel digital TTL input/output board (PCI-DIO-32-HS) switches discrete electronic devices (*e.g.* shutters).
- A GPIB board communicates directly with external devices (*e.g.* the arbitrary function generator used for RF evaporation).

In addition to these boards several electronic devices developed at the Oxford University Physics Department Electronics Workshop are also used. The 'Voltage Reference Switching Unit' allows a single TTL to switch between two analogue levels while the 'Voltage Level Multiplexer' allows two TTL inputs to switch between four analogue levels. Device delays were accounted for in the LabVIEW program to ensure that experimental parameters changed at the desired time.

At the time of writing the experimental control system is being upgraded to use a LabVIEW FPGA module in place of the PCI-6713 and PCI-DIO-32-HS boards. This will allow simultaneous control of analogue and digital channels throughout the experiment and offer greater freedom when running future experiments.

Chapter 4

Optimisation and Characterisation

This chapter describes the optimisation of all phases in the experiment up to and including the loading of the ultracold ^{87}Rb - ^{133}Cs mixture into the magnetic quadrupole trap. Details of experiments performed in the magnetic and hybrid potentials are presented in chapters 5-8.

4.1 Pyramid MOT

The pyramid MOT acts as a cold atom source for the two-species science MOT in the UHV glass cell. Initially both the pyramid and science MOTs were roughly optimised before the pyramid MOT was rigorously optimised with the science MOT fixed. Throughout this optimisation the atom number loaded into the science MOT in 10 seconds was monitored using fluorescence detection and maximised. The key parameters used to optimise the flux of atoms from the pyramid MOT were the achromatic $\lambda/4$ waveplate angle, the magnetic field gradient and field zero position, the detuning of the cooling light, the intensity of both the cooling and the repump light and the atomic vapour pressure (via the dispenser current).

The cooling light from the pyramid fibre was set to maximum peak intensities of 11.5(7) mW/cm^2 and 8.1(5) mW/cm^2 for ^{87}Rb and ^{133}Cs respectively. The total pyramid MOT cooling light intensity for each species is approximately

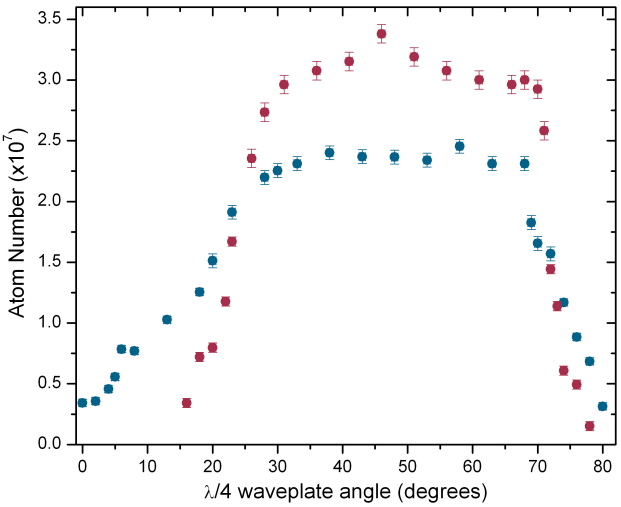

Figure 4.1: Pyramid $\lambda/4$ waveplate angle optimisation. The atom number captured in the science MOT after a 10 s load was measured using fluorescence detection for ^{87}Rb (red) and ^{133}Cs (blue). A broad window of optimal loading was observed for both species highlighting that, as expected, the achromatic $\lambda/4$ waveplates used in this experiment work well at both 780 nm and 852 nm.

six times these values. The repump light in the pyramid beam provides 0.86(5) mW/cm^2 and 0.81(5) mW/cm^2 of intensity for ^{87}Rb and ^{133}Cs respectively. These intensities were sufficient to keep the atoms in the cycling cooling transitions.

The science MOT load was investigated as a function of the $\lambda/4$ waveplate angle, figure 4.1. This shows a broad window of optimal loading for both species from 30° to 65°, the final angle was set to 48°. The optimum cooling light detuning was investigated for various magnetic field gradients from 5 to 15 G/cm. The optimum settings were located at a magnetic field gradient of 7.8(1) G/cm with detunings of -18.3(1) MHz and -16.8(1) MHz for ^{87}Rb and ^{133}Cs respectively. These optimum detunings were for the pyramid MOT acting as a cold atom source for the science MOT. When operated as a static MOT the optimum cooling light detunings were smaller by $\sim$ 6 MHz for both species for the same magnetic field gradient.

The alignment of the MOT centre dictates whether the pyramid MOT will

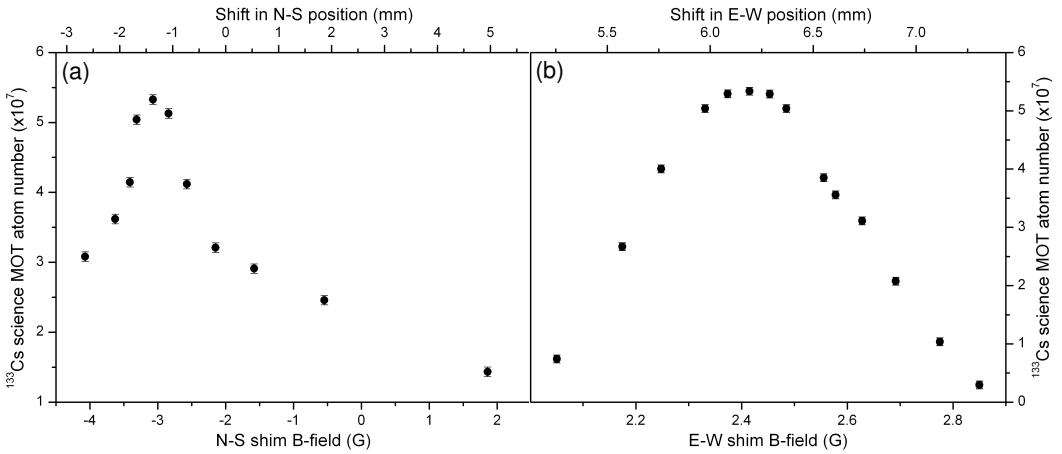

Figure 4.2: Pyramid shim field optimisation for ^{133}Cs in the (a) N-S and (b) E-W directions with an axial pyramid magnetic gradient of 7.8(1) G/cm. Changing the magnetic field translates the position of the B-field zero. The ^{133}Cs atom number loaded into the science MOT in 10 s was monitored using fluorescence detection. Similar data were obtained for ^{87}Rb.

act as a cold atom source or as a static MOT. This is controlled using the two pyramid shim coils to move the zero point of the magnetic gradient in the N-S and E-W directions (using the orientation defined by figure 3.13). By centering the field zero and therefore the MOT over the aperture at the pyramid apex the MOT acts as a cold atom source for the science MOT. By positioning the MOT away from the aperture the pyramid acts as a static MOT with no flux into the science MOT. The degree of movement of the MOT is proportional to the applied bias field from the shim coil and inversely proportional to the magnetic field gradient. The optimisation of the N-S and E-W shim fields is shown in figure 4.2 for a 7.8(1) G/cm gradient. The optimum pyramid shim settings are bias fields of -3.07(1) G and 2.42(1) G for the N-S and E-W shims respectively. When fully optimised the pyramid MOT loads $\simeq 1 \times 10^8$ ^{87}Rb and $\simeq 7 \times 10^7$ ^{133}Cs atoms into the science MOT in 10 s.

4.2 Science MOT

The role of the science MOT is to capture the maximum number of ^{87}Rb and ^{133}Cs atoms in the UHV glass cell for collective transfer into the magnetic quadrupole trap. Once the pyramid MOT was fully optimised a rigorous optimisation of the science MOT was performed by varying the magnetic field gradient and zero position, the cooling light detuning, and the cooling and repump light intensities. As some of these parameters are not independent for both species the initial optimisation was performed for ^{87}Rb only. The full parameter space was explored to give the maximum number of ^{87}Rb atoms in the science MOT. Once ^{87}Rb was optimised all independent ^{133}Cs parameters were optimised, while running the two species MOT, to maximise the number of ^{133}Cs atoms loaded whilst maintaining the maximum number of ^{87}Rb atoms.

All MOT beams were aligned to intersect within $\simeq$ 1 mm of the centre of the coil assembly. To avoid light assisted collisions between the two species in the MOT [154] small adjustments were made to the ^{133}Cs $\lambda/4$ waveplates in the plane of the cell to separate the MOT centres by $\simeq$ 2 mm in the N-S direction. The cooling light for both species was split into six laser beams with approximately equal peak intensities of 13.0(9) mW/cm^2 and 10.5(7) mW/cm^2 for ^{87}Rb and ^{133}Cs respectively. Repumping light for ^{87}Rb (^{133}Cs) with a peak intensity of 1.7(1) mW/cm^2 (1.1(1) mW/cm^2) ensured that all atoms remained cycling on the cooling transition. Similar to the pyramid MOT the optimum detuning of the science MOT cooling light for both species was investigated for various magnetic field gradients between 5 and 15 G/cm. The results for ^{87}Rb are presented in figure 4.3. The optimum settings for ^{87}Rb were found to be a detuning of -12.2(1) MHz at a magnetic field gradient of 10.3(1) G/cm. At this gradient the optimum detuning for ^{133}Cs is -10.8(1) MHz from resonance. Once optimised up to $\simeq 3.5 \times 10^8$ ^{87}Rb atoms and $\simeq 3.0 \times 10^8$ ^{133}Cs atoms could be simultaneously loaded into the science MOT in 30 s.

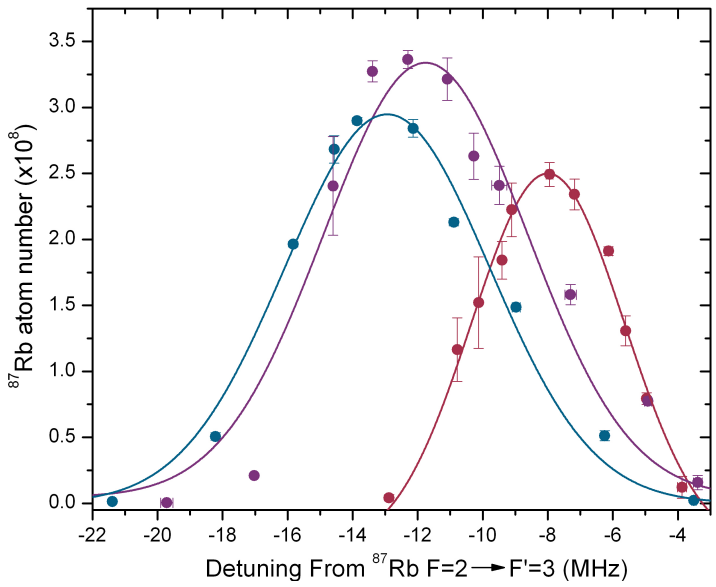

Figure 4.3: Optimisation of the science MOT cooling light detuning for ^{87}Rb. The cooling light detuning was varied for magnetic field gradients of 5.01(5) G/cm (red), 10.3(1) G/cm (purple) and 15.0(1) G/cm (blue). The maximum ^{87}Rb atom number in the science MOT at each detuning was measured using fluorescence detection. The lines plotted are to guide the eye only. The same behaviour was observed for ^{133}Cs.

4.3 Compressed MOT

During the compressed magneto-optical trap (CMOT) stage the MOT coil gradient is decreased to 8.3(1) G/cm and the detuning of the cooling light is increased to $-30.9(1)$ MHz ($-28.4(1)$ MHz) for ^{87}Rb (^{133}Cs) using AOM3 (figure 3.2). These changes increase the atomic density of both species by decreasing the number of scattered photons reabsorbed and also result in the ^{133}Cs MOT moving $\simeq 2$ mm to become overlapped with the ^{87}Rb MOT. Here the optimised CMOT acts as an intermediate step between the MOT and optical molasses stages. The optimum CMOT duration of 7 ms results in the atomic density increasing by a factor of ~ 2 for both species. Simultaneously, to efficiently transfer the overlapped ^{87}Rb and ^{133}Cs atoms from the optimum MOT loading position to the centre of the magnetic quadrupole trap the science MOT shim coil settings are changed to shift the MOT position. This magnetic trap loading position was optimised in three dimensions

to minimises the potential energy gained by the atoms and give the highest initial phase-space density in the magnetic quadrupole trap. This change in the MOT position results in the cloud moving 3.6(4) mm from the optimum MOT loading position. After the CMOT phase the $\simeq 3.5 \times 10^8$ ($\simeq 3.0 \times 10^8$) ^{87}Rb (^{133}Cs) atoms have a temperature of $\simeq$ 150 μK ($\simeq$ 130 μK) and a density of $\simeq 5 \times 10^9$ cm^{-3} ($\simeq 10^{10}$ cm^{-3}).

4.4 Optical Molasses

Once at the optimum magnetic trap loading position the ^{87}Rb - ^{133}Cs cloud is cooled prior to loading the quadrupole trap by the optical molasses stage [160]. This is implemented by simultaneously switching off the science MOT coils and increasing the detuning of the ^{87}Rb (^{133}Cs) cooling light to $-59.4(1)$ MHz ($-53.7(1)$ MHz). The science MOT shim coils are set to null the magnetic field in the glass cell by measuring the field on all sides of the glass cell using a calibrated Hall probe. The polarisation gradient cooling [161] driven at this stage allows temperatures well below the Doppler limit [162] (146 μK for ^{87}Rb and 125 μK for ^{133}Cs) to be reached. The optimised optical molasses stage has a 12 ms duration and cools the ^{87}Rb and ^{133}Cs atoms to 19(4) μK and 15(3) μK respectively. These temperatures were calculated by measuring the widths of the cloud as a function of the time-of-flight via absorption imaging and fitting equation 2.48.

4.5 Optical Pumping

Before loading the magnetic trap the optical pumping stage polarises the ^{87}Rb and ^{133}Cs atoms into the $|1, -1\rangle$ and $|3, -3\rangle$ states respectively without significantly heating the mixture. Polarising the atoms into these magnetically trappable states ensures efficient transfer into the magnetic trap and avoids inelastic collisions between atoms in different m_F sublevels.

To depump the atoms into the lower hyperfine ground state a 2 ms pulse of far detuned MOT cooling light is used. The optimum detunings for the MOT cooling light were measured to be -96.2(1) MHz and -67.1(1) MHz for ^{87}Rb

and ^{133}Cs respectively. At these detunings the maximum peak intensity of each MOT beam is 3.0(2) mW/cm^2 for ^{87}Rb and 7.8(5) mW/cm^2 for ^{133}Cs. Absorption images of the upper hyperfine ground state only allowed the effect of this depump light to be measured. Effective depumping resulted in a complete absence of atoms imaged in the upper hyperfine ground state, in contrast to the case with no depump pulse.

The optical pumping light for both species is aligned down separate fibres and combined on a breadboard above the glass cell using a dichroic mirror. The combined optical pumping beam is circularly polarised using an achromatic quarter waveplate (Casix WPA1212-700-1000 nm) and aligned along the vertical axis of the cell. A second optical pumping beam is added by retro-reflecting the first beam after transmission through the cell. The optical pumping shim coil produces a 2.7(1) G quantization field in the vertical direction such that σ^- transitions are driven. The science MOT shim coils remained in the molasses settings. When the depump and optical pumping pulses are combined atoms are pumped towards and accumulate in the $|1,-1\rangle$ and $|3,-3\rangle$ dark states for ^{87}Rb and ^{133}Cs respectively.

To optimise the optical pumping the intensity, detuning, polarisation and pulse duration were all varied. The effect of the optical pumping light was initially measured by switching on the magnetic quadrupole trap at 50 G/cm for 1 s after the optical pumping pulse before the magnetically trapped atoms were recaptured in the science MOT. An initial crude optimisation was performed by maximising the number of atoms of each species in the magnetic trap. A more refined optimisation then followed using absorption imaging to measure the temperatures of the ^{87}Rb and ^{133}Cs atoms to allow the phase-space density of each species in the magnetic trap to be maximised.

The effect of the optical pumping and depumping light is presented in figure 4.4. Here the fraction of ^{133}Cs atoms loaded into the magnetic trap for a 1 s hold and then recaptured in the MOT is plotted as a function of the magnetic field gradient. The closed symbols show the fraction recaptured with depump light only and the open symbols show data for depump and optical pumping light. The dashed lines mark the four gradients that exactly levitate each of the non-zero ^{133}Cs magnetic sublevels, see table 2.2. Above these thresholds each low field seeking state can be confined in the magnetic trap. For both

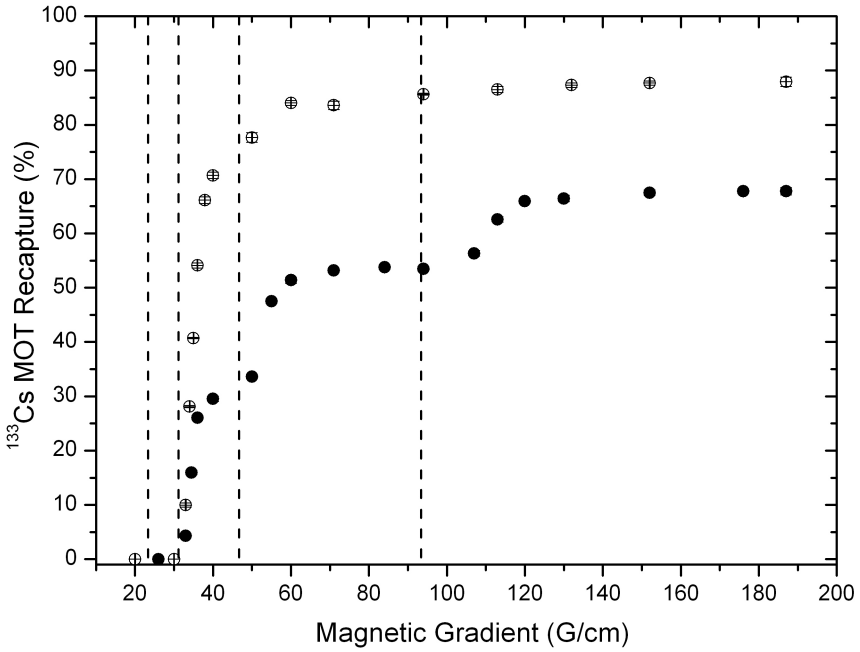

Figure 4.4: Percentage of ^{133}Cs atoms recaptured in the MOT after a 1 s hold in the magnetic trap as a function of the magnetic field gradient. Closed symbols show data for the depump only case and open symbols show data for the depump and optical pumping case. The dashed lines indicate the magnetic field gradients that exactly levitate each non-zero magnetic sublevel for ^{133}Cs (table 2.2).

cases the depump light ensures no atoms populate the $F = 4$ ground state and so no atoms are recaptured for gradients less than 31.1 G/cm. With depump light only (closed symbols) the atoms populate all seven magnetic sublevels in the $F = 3$ ground state. This results in more ^{133}Cs atoms being recaptured as the gradient is increased to levitate the $m_F = -3$ atoms from 31.1 G/cm, with $m_F = -2$ atoms from 46.7 G/cm and $m_F = -1$ atoms from 93.4 G/cm. In contrast, when the optical pumping light is combined with the depump light (open symbols) all of the ^{133}Cs atoms populate the $|3, -3\rangle$ state leading to a recapture of up to 85 % for gradients greater than 31.1 G/cm.

To test the direction of the quantisation axis defined by the 2.7(1) G bias field the science MOT shim coils in the N-S and E-W directions were used to create small additional bias fields during the optical pumping phase. The

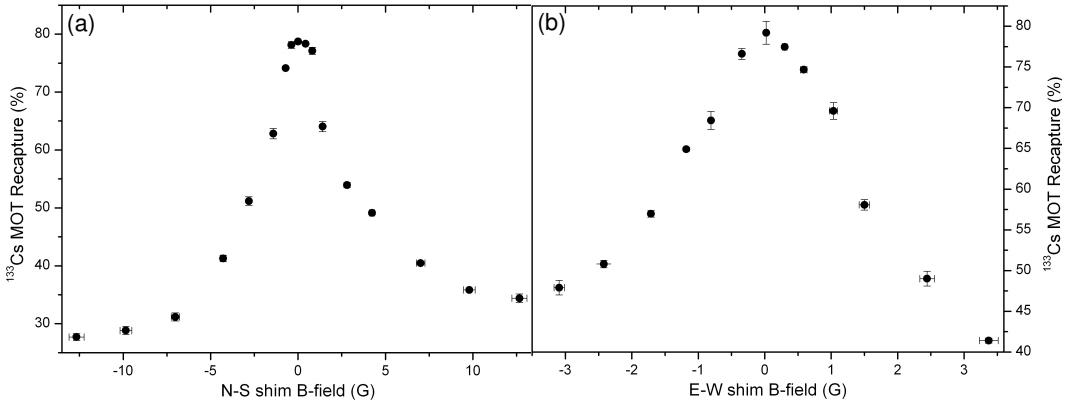

Figure 4.5: Percentage of ^{133}Cs atoms recaptured in the MOT after a 1 s hold in the magnetic trap at 50 G/cm as a function of (a) the N-S and (b) the E-W shim coil bias fields. As the bias field in the horizontal direction is increased the optical pumping quantisation axis is progressively tilted from its original vertical direction. This reduces the efficiency of the optical pumping as fewer σ^- and more π and σ^+ transitions are driven.

percentage of ^{133}Cs atoms recaptured in the MOT after a 1 s hold at 50 G/cm was then investigated as a function of the additional shim field. The results of this investigation are presented in figure 4.5. As expected, these data show that the optical pumping works best for a vertical bias field with no additional field in a horizontal direction. This confirms that the previous nulling of the stray field was accurate and indicates that the polarisation of the circularly polarised optical pumping light is very pure. If the sign of the bias field is reversed (or the handedness of the circular polarisation is flipped) σ^+ transitions are driven and the atoms are pumped into $|1, +1\rangle$ and $|3, +3\rangle$ for ^{87}Rb and ^{133}Cs respectively. As these states are high field seekers this results in no atoms being confined by the magnetic trap.

After the refined optimisation the optical pumping peak intensities were 11.0(6) μW/cm^2 for ^{87}Rb and 46(2) μW/cm^2 for ^{133}Cs at detunings of +5.9(1) MHz and +11.9(1) MHz respectively. All optical pumping and depump pulses were set to be 5 ms long. This allowed up to $2.14(2) \times 10^8$ ^{87}Rb and $1.90(2) \times 10^8$ ^{133}Cs atoms to be loaded into the magnetic trap at 50 G/cm.

4.6 Magnetic Trap Loading

After the atomic mixture was compressed and positioned at the magnetic trap centre, cooled and then pumped into the appropriate low field seeking states, the magnetic trap turn on sequence was optimised. This was done by maximising the phase-space density of the ^{87}Rb and ^{133}Cs atoms transferred into the trap. Maximum phase-space densities were obtained when the trap was switched on to 40 G/cm in 0.50(1) ms and immediately ramped to 60 G/cm in 100 ms, the mixture was then held at 60 G/cm for a further 100 ms before the gradient was increased adiabatically to 187 G/cm in 1 s. This adiabatic compression is performed to increase the elastic collision rates in the magnetic trap in order to increase the efficiency of the RF evaporation of ^{87}Rb and the sympathetic cooling of ^{133}Cs.

By switching the magnetic trap on in this manner up to $2.5(1)\times10^8$ ^{87}Rb and $2.0(1)\times10^8$ ^{133}Cs atoms are loaded into the magnetic trap. Immediately after the adiabatic ramp to 187 G/cm the ^{87}Rb and ^{133}Cs atoms have temperatures of 184(3) μK and 167(3) μK respectively. This corresponds to initial phase space densities of $2.4(2)\times10^{-7}$ for ^{87}Rb and $5.8(5)\times10^{-7}$ for ^{133}Cs.

4.7 Hybrid Trap Characterisation

To characterise the behaviour of the hybrid trap several single species measurements were performed in both the loading and levitated crossed dipole potentials. The precooling and loading of the hybrid potential are discussed in chapter 5. Once the parameters of the hybrid trap were measured and understood it was possible to quickly and accurately model all configurations of hybrid potential using a MATLAB code. These simulations allowed accurate hybrid trap depths and frequencies to be calculated and avoided numerous experimental measurements similar to those detailed in this section.

4.7.1 Trap Depth

To determine the trap depth the equilibrium temperature in the potential was measured using a 'long dipole hold' (LDH). Once the levitated crossed

dipole trap was loaded the atoms were held for long times ($t \geq 30$ s) and the atom number and temperature were measured. Figure 4.6 shows an LDH measurement for ^{87}Rb atoms in the levitated crossed dipole trap with 6 W in each dipole beam, a magnetic field gradient of 29 G/cm and a bias field of 22.4 G. After the initial plain evaporation from the trap the measured

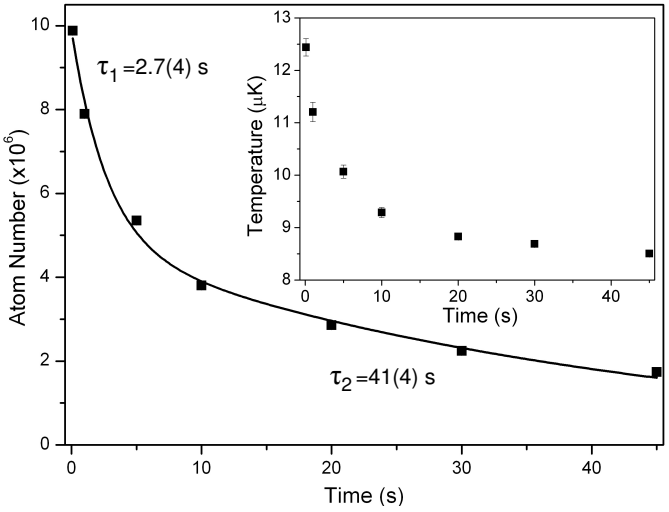

Figure 4.6: A long dipole hold measurement on ^{87}Rb atoms in the levitated crossed dipole trap with 6 W in each dipole beam, a 29 G/cm gradient and a 22.4 G bias field. In the main plot the atom number in the trap is shown as a function of time. The data are fit with a double exponential function to determine trap lifetimes. The inset shows the evolution of the atom temperature over the same time period. Initially plain evaporation limits the ^{87}Rb lifetime to 2.7(4) s and results in the atom temperature decreasing from ~ 13 μK to ~ 9 μK. After this plain evaporation the trap lifetime increases to 41(4) s and the ^{87}Rb atoms reach an equilibrium temperature of 8.8(2) μK. This corresponds to a ^{87}Rb trap depth of 90 μK.

equilibrium temperature, $T_{\rm eq}$, is 8.8(2) μK. Using the empirical rule for dipole traps $T_{\rm eq} \simeq 0.1 U_0/k_{\rm B}$ [133] this implies a trap depth, U_0, for ^{87}Rb of 90 μK in good agreement with simulations. For these levitated dipole trap parameters this depth corresponds to dipole trap beam waists of 63 μm and is in good agreement with the measured values of 65(4) μm and 61(1) μm.

4.7.2 Trap Frequencies

To directly measure the trap frequencies there are two possible methods available. Firstly a magnetic field can be applied for several milliseconds to excite a centre of mass motion of the cloud in a specific direction. Oscillations of the cloud around the trap centre can then be observed as a function of the hold time to measure the trap frequency in that specific direction. This measurement was performed in the axial direction of the single beam hybrid trap for a beam power of 3.7 W and a magnetic gradient of 29 G/cm. A 0.20(1) G bias field applied in the E-W direction for 10 ms offsets the cloud by 138(7) μm before the cloud was allowed to oscillate freely in the axial direction. The data for this measurement are displayed in figure 4.7 (a). The period of this oscillation was measured to be 38.7(1) ms which corresponds to an axial trap frequency of $\omega_z = 25.8(1)$ Hz. This result corresponds to a theoretical beam waist of 64(2) μm in excellent agreement with the measured value of 65(4) μm.

The second method used to measure the trap frequencies involves modulating one of the dipole trap beam powers, and hence the potential depth, at a specific frequency using the AOM. In practice this is done by summing a small additional sinusoidal voltage onto the main control voltage sent to the AOM RF driver. This sinusoidal burst causes the atoms to oscillate in the trap at the modulation frequency. If the modulation frequency equals twice the axial or radial trap frequency of the potential ($\omega_{\mathrm{mod}} = 2\omega_{\rho,z}$) atoms are parametrically heated and are lost from the trap. Parametric resonances can also be excited at subharmonic frequencies where $\omega_{\mathrm{mod}} = 2\omega_{\rho,z}/n$, where n is an integer [163].

Figure 4.7 (b) shows the atom number as a function of the modulation frequency for this measurement performed on ^{133}Cs in a levitated crossed dipole trap. Here the dipole beam powers were 50 mW, the magnetic gradient was 29 G/cm and the bias field was 22.4 G. For each data point beam 1 was modulated at a specific frequency by ± 8 mW for 1 s before absorption imaging probed the number and temperature of the atoms remaining in the trap. These data show that five parametric resonances were observed corresponding to $\frac{2}{3}\omega_z = 3.90(1)$ Hz, $\omega_z = 5.33(5)$ Hz, $2\omega_z = 11.1(2)$ Hz, $\omega_\rho = 40.0(4)$ Hz and

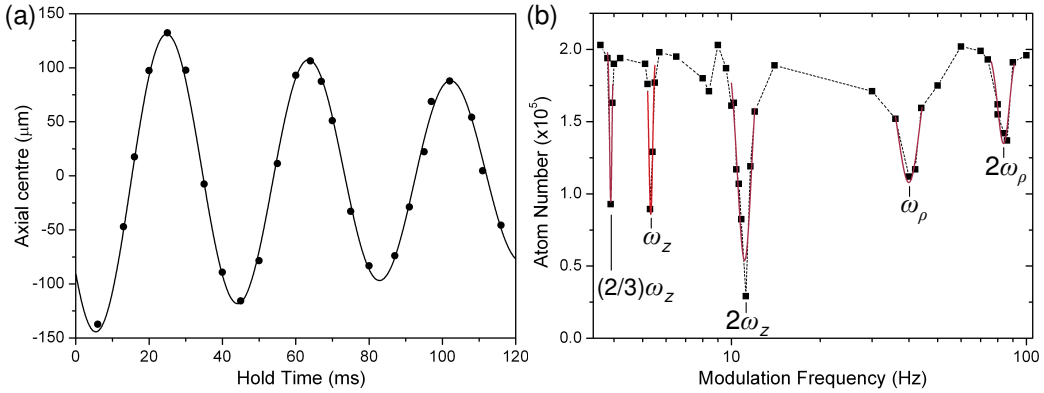

Figure 4.7: (a) Single beam trap axial frequency measurement performed by measuring the oscillation period in the trap. The plot shows the axial position of the cloud vs the hold time in the hybrid trap. Here a period of 38.7(1) ms is measured corresponding to an axial trap frequency of 25.8(1) Hz. This method is limited by the time resolution during the hold and is typically not used to measure trap frequencies > 100 Hz. (b) Levitated crossed dipole trap frequencies measured using the beam power modulation technique. Gaussian fits to the data give measured resonance positions of 3.90(1), 5.33(5), 11.1(2), 40.0(4) and 84(3) Hz which correspond to the labelled harmonic and subharmonic frequencies.

$2\omega_\rho = 84(3)$ Hz. For the beam powers and magnetic field parameters used these trap frequencies correspond to theoretical beam waists of 64(1) μm, again in good agreement with the measured values.

The trap frequencies can also be inferred from measuring the expansion of the cloud as a function of the time-of-flight after the potential has been removed. By plotting the square of the cloud width $\sigma_{x,z}^2$ as a function of the square of the time-of-flight equation 2.48 can be applied to the data. The slope of this fit reveals the clouds temperature and the intercept can be used to calculate the trap frequency in that direction from the initial cloud size. However it should be noted that this method is not applicable for large trap frequencies as the initial cloud size is too small and dominated by random errors from the cloud fitting process.

Chapter 5

^{87}Rb BEC in a Hybrid Trap

Initial work loading and cooling in the hybrid trap used ^{87}Rb alone. Previous work with a similar hybrid potential used ^{87}Rb and provided a useful reference for comparison [133]. The large ratio of elastic to inelastic collisions in ^{87}Rb makes this species relatively easy to condense and its properties have been studied by many groups around the world. Finally, it was important to fully optimise the cooling of the ^{87}Rb refrigerant before the ^{133}Cs refrigeree was introduced for effective sympathetic cooling to occur. The route to ^{87}Rb BEC combines several elements irrespective of the specific hybrid trap configuration used:

1. A large recapture from the MOT into the magnetic quadrupole trap.
2. Efficient forced RF evaporation in the quadrupole trap.
3. A large gain in phase-space density when loading the magnetically trapped atoms into the hybrid potential.
4. Efficient evaporation to BEC within the hybrid potential.

5.1 RF Evaporation in the Quadrupole Trap

Once loaded into the magnetic quadrupole trap the ^{87}Rb atoms were pre-cooled with forced RF evaporation. To increase the elastic collision rate the magnetic trap was adiabatically compressed to 187 G/cm. The RF was

Stage	t_{stage} (s)	t_{total} (s)	f_{start} (MHz)	f_{stop} (MHz)	RF amp. (dBm)
1	20.0	20.0	60.0	20.5	-0.5
2	7.5	27.5	20.5	12.3	-0.5
3	5.0	32.5	12.3	7.0	-0.5
4	2.0	34.5	7.0	3.8	-0.5

Table 5.1: Optimised RF evaporation parameters for the four RF stages investigated with ^{87}Rb alone in the magnetic trap. All RF cuts follow linear ramps in the frequency.

produced by an arbitrary function generator (Textronix AFG3252) and amplified (Mini-Circuits ZHL-3A) before being broadcast by a two turn RF coil 25 mm to the south of the glass cell. Each linear RF cut was optimised to give the maximum evaporation efficiency, defined by equation 2.64. This represents the biggest gain in phase-space density per fraction of atoms removed from the trap. The optimisation was performed by varying the ramp duration t_{stage}, the final RF frequency f_{stop}, and the RF amplitude. In total four stages of evaporation were optimised for the ^{87}Rb alone case and are summarised in table 5.1. The results of this optimised forced RF evaporation on the trapped ^{87}Rb cloud are presented in table 5.2. This table shows the atom number, temperature and phase-space density of the ^{87}Rb atoms after the magnetic trap has been loaded and adiabatically compressed and after each optimised RF cut. The table also presents the evaporation efficiency for each stage.

As the RF evaporation in the quadrupole trap proceeds the trapped cloud becomes colder and denser resulting in more atoms residing near the trap centre and the magnetic zero field. This causes the Majorana loss rate from the trap to increase as the cloud becomes colder and results in a shorter trap lifetime, see equation 2.60. These Majorana losses limit the maximum phase-space density attainable in the magnetic quadrupole trap. The relationship between the ^{87}Rb temperature and the trap lifetime was investigated to characterise the Majorana losses from the quadrupole trap. During the lifetime measurements the final frequency of the RF knife was applied to maintain a

Stage	$N(\times 10^7)$	$T(\mu\text{K})$	Phase-Space Density	Efficiency γ
MT Loaded	25(1)	184(3)	$2.4(2) \times 10^{-7}$	-
1	12.1(1)	120(1)	$8.7(4) \times 10^{-7}$	1.8(2)
2	6.4(2)	62(2)	$9.0(7) \times 10^{-6}$	3.7(4)
3	2.64(2)	28.8(3)	$1.2(1) \times 10^{-4}$	2.9(3)
4	0.78(2)	10.3(2)	$3.5(3) \times 10^{-3}$	2.8(3)

Table 5.2: Forced RF evaporation results for ^{87}Rb alone in the magnetic trap at 187 G/cm. Data are presented for ^{87}Rb after loading and adiabatic compression in the magnetic trap and after each optimised RF ramp.

constant temperature and avoid heating from the Majorana spin flips. Although this led to more atoms being removed from the trap via evaporation as the Majorana losses heated the cloud. As a result the measured trap lifetimes are not purely due to Majorana losses but should be treated as lower limits. The data are presented in figure 5.1. The closed circles show the trap lifetime vs the temperature and clearly show that as the atom temperature decreases the trap lifetime becomes shorter. The open circles show the calculated elastic collision time in the trap as a function of the temperature. The fit applied to the lifetime data in figure 5.1 has the form $\tau = 1/(AT^p + B)$, where AT^p is the Majorana loss rate and B is the background loss rate. The calculated background lifetime from this fit is 300(20) s which compares well to the measured value of 290(10) s. The fit also gives $p = -2.3(3)$ and $A = 510(40)$ s$^{-1}\mu$K^2 which are in excellent agreement with the values predicted by equation 2.60. Throughout the evaporative cooling the elastic collision time decreases from 2.5(6) s to $1.1(1) \times 10^{-2}$ s. At all stages during this evaporation the elastic collision time is least 50 times shorter than the trap lifetime. This confirms that the assumption of thermal equilibrium made in section 2.5.1 is valid.

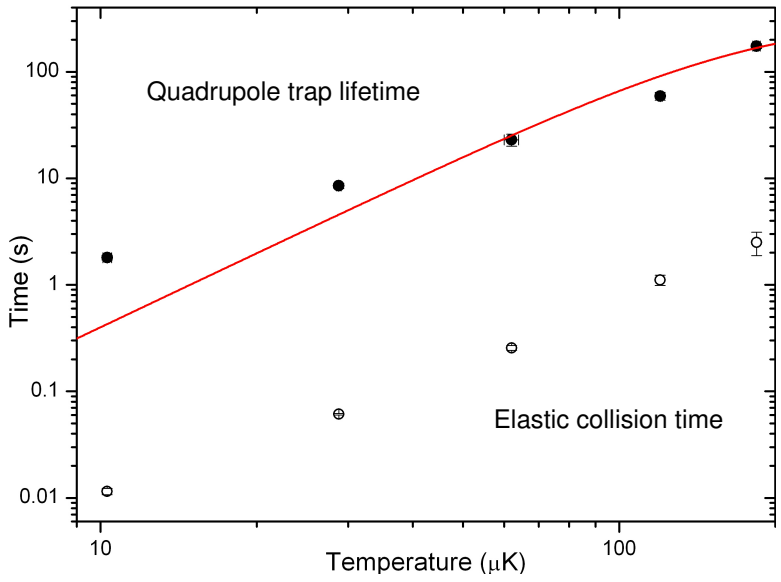

Figure 5.1: Lifetime and elastic collision time ($\Gamma_{\mathrm{El.}}^{-1}$) as a function of temperature for ^{87}Rb atoms in the quadrupole trap at 187 G/cm. Closed circles show data for the trap lifetime while open symbols present the elastic collision time. The fit applied to the lifetime data is based on equation 2.60 and discussed in the text.

5.2 Aligning and Loading a Single Beam Hybrid Potential

To align the single beam dipole trap the optimum beam position was found independently in all three dimensions. Firstly the beam waist was aligned to occur at the same axial position as the magnetic field zero. If this alignment is not done the beam size at the hybrid trap centre may be bigger than expected resulting in a reduced trap depth and weaker radial confinement. In practice this was done by translating the the 200 mm focal length lens axially along the beam to change the position of the beam waist while measuring the temperature of the atoms loaded into the hybrid potential. Each temperature measurement was made after a 4 s hold to ensure that the cloud had come into thermal equilibrium with the potential. As discussed in section 4.7 for dipole traps the equilibrium temperature $T_{\mathrm{eq}} \simeq 0.1U_0/k_{\mathrm{B}}$, where U_0 is the trap depth. When the waist is at the optimum position a maximum atom

temperature is measured. These data are shown in figure 5.2. The Gaussian beam propagation fit gives the optimum position as 46.7(4) mm from a fixed arbitrary reference point.

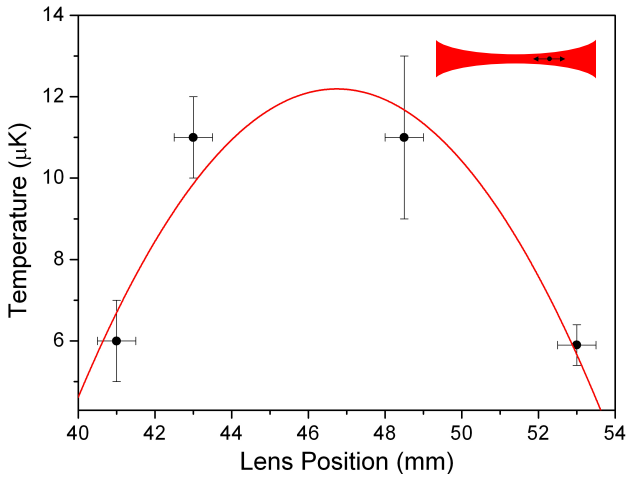

Figure 5.2: Aligning the single beam axially with respect to the magnetic field zero. The beam waist position was varied by translating the final lens axially along the beam. The atom temperature at each position indicated the trap depth. The fit to the data (solid red line) reveals that the optimum lens position is at 46.7(4) mm.

To align the single dipole beam in the y-direction (see scale on figure 3.14) the beam was fixed at the vertical position of the magnetic field zero. This vertical position was determined from absorption imaging of the magnetically trapped atoms. The beam was then scanned horizontally along the y-axis. A reduction in the loaded atom number was observed at the location of the field zero due to Majorana losses, see inset of figure 5.3. The beam was aligned horizontally to be at the position of the magnetic field zero.

To optimise the vertical position of each beam the transfer efficiency and subsequent evaporation efficiency were investigated as a function of the displacement from the quadrupole field zero. As the radial confinement is provided by the dipole beam the radial trap frequency is largely independent of the vertical position. In contrast the axial trap frequency is very sensitive to the vertical position as the axial confinement is provided by the magnetic quadrupole field. The dipole trap can be positioned above or below the mag-

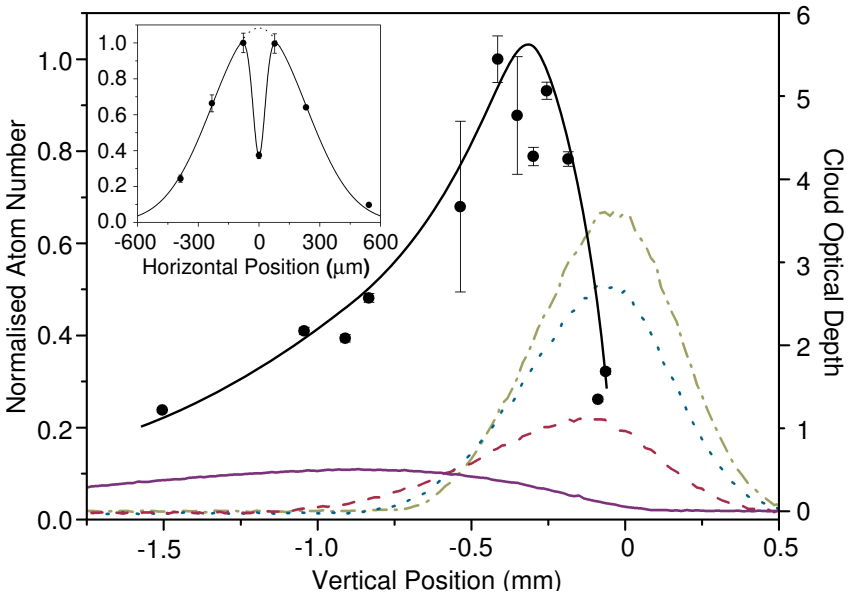

Figure 5.3: Aligning the single beam hybrid trap. Atom number (black circles) is measured as a function of the vertical and horizontal (inset) beam position with respect to the unbiased field zero of the quadrupole potential. The fits to these data (black lines) are to guide the eye. The beam power was 3.7 W, the waist was $\simeq$ 110 μm and the gradient was 29 G/cm. The coloured lines show the evolution of the cloud density profile during the loading as the magnetic gradient is reduced from 187 G/cm (dashed-dotted green line) through 135 G/cm (dotted blue line) and 80 G/cm (dashed red line) to 30 G/cm (solid purple line). The solid and dotted black lines are to guide the eye only. The data in the inset were taken with no vertical offset of the dipole trap and reveal the position of the field zero through the reduction in the trapped atom number due to Majorana spin flip losses.

netic field zero, however the combined trap is significantly deeper below the field zero and hence the beams are positioned there.

Figure 5.3 shows the number of atoms loaded into a single beam hybrid trap with a $\simeq$ 110 μm beam waist as a function of vertical position with respect to the magnetic field zero. The maximum number of atoms loaded into the dipole trap is observed at $\sim$ 3 beam waists below the field zero. However, experiments have revealed that the evaporation is more efficient when the beam waist is positioned approximately one beam waist below the

field zero, in agreement with previous measurements [133]. This is due to the increase in the axial trap frequency closer to the magnetic trap centre. For the current beam waists of $\simeq 60$ μm the optimum positions for the single beam traps are $\simeq 80$ μm below the field zero. With 3.7 W in the dipole beam the optimised single beam potential for ^{87}Rb has a trap depth of $\simeq 70$ μk and measured axial (ν_z) and radial (ν_ρ) trap frequencies of 25.8(1) Hz and 370(20) Hz respectively.

Once the single beam hybrid potential was aligned the loading of the trap was addressed. To transfer atoms into the optimally aligned single beam potential the magnetic field gradient and RF frequency are simultaneously decreased in 4 s to 29 G/cm and 3 MHz respectively. During the ramp the optical potential is loaded through elastic collisions in a similar manner to a dimple trap [12]. This transfer is similar to evaporation, here the 'evaporated' atoms during the loading are contained in the low density tails of the weakly confining quadrupole trap. Optimum results were obtained when only the first three RF ramps from table 5.1 were applied in the quadrupole trap before the hybrid trap was loaded. This is due to the trap lifetime after all four RF ramps being just 1.8(2) s, this is too short for efficient transfer to occur via elastic collisions. Immediately after the single beam trap is loaded there are $4.9(1) \times 10^6$ ^{87}Rb atoms at 9.2(1) μK, this corresponds to a phase-space density of $2.3(1) \times 10^{-3}$.

5.3 Evaporation in the Hybrid Trap to BEC

Once the single beam hybrid trap has been loaded the atoms are held in the potential for 5 s to take advantage of plain evaporation from the trap. After this hold $4.1(1) \times 10^6$ ^{87}Rb atoms remain in the trap at 7.0(1) μK, corresponding to roughly $U_0/10$. Forced evaporation is then performed by linearly reducing the trap depth to $\simeq 12$ μK in 7 s. In practice this is done by linearly reducing the beam power from the initial 3.7 W to 925 mW. This change also relaxes the radial trap frequency from 370 Hz to 150 Hz and results in an effective reduction of the trap depth by a factor of ~ 4. After a further 3 s hold $2.10(5) \times 10^6$ atoms at 1.16(7) μK remain, this corresponds to a phase-space density of $1.2(1) \times 10^{-1}$. The final stage of evaporation reduces

the trap depth to a variable U in 10 s by linearly reducing the beam power further. For $U = 4.6(2)$ μK (381 mW) a bimodal distribution is observed after a 25 ms time-of-flight, see figure 5.4. This image shows a $\sim$ 15 % condensate fraction of the total number $7.0(1) \times 10^5$ at $0.25(4)$ μK; for this potential the calculated $T_c = 0.3$ μK. At $U = 3.2(1)$ μK (251 mW) the condensate is pure and contains up to $9.1(2) \times 10^5$ ^{87}Rb atoms in the $|1, -1\rangle$ state. The complete trajectory to ^{87}Rb BEC in a single beam hybrid trap is presented in figure 5.4.

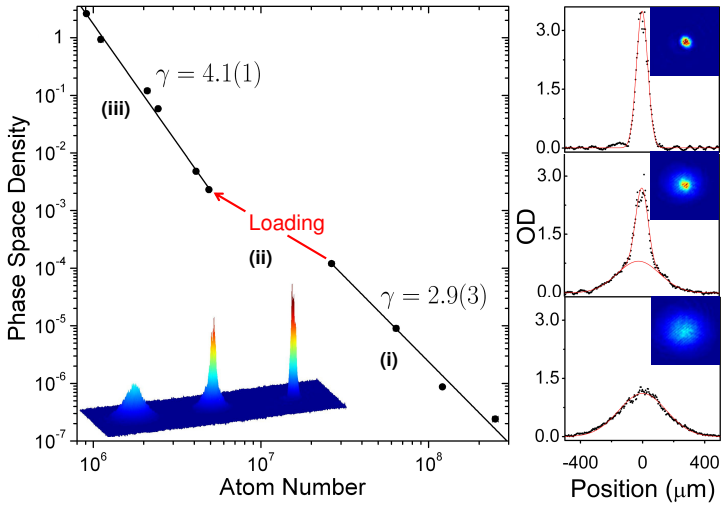

Figure 5.4: Trajectory to ^{87}Rb BEC in a single beam hybrid potential. The different regions show: (i) RF evaporation in the quadrupole trap. (ii) Loading the single beam hybrid trap. (iii) Evaporation by reducing the hybrid trap beam power. The trajectory gradient indicates the evaporation efficiency, γ. Inset: 3D rendering of the density distribution as the cloud is condensed. Right: absorption images (400×400 μm) and cross sections of the ^{87}Rb cloud near the BEC transition.

5.4 Condensate Properties

Once ^{87}Rb condensates could be made in the single beam hybrid trap some of the characteristic signatures of the BEC transition were measured. As discussed in section 2, theoretically the critical temperature T_c is defined

by equation 2.22 and below T_c the condensate fraction varies according to equation 2.26 [117].

In figure 5.5 the measured condensate fraction from a double Gaussian fit is plotted as a function of the normalised temperature T/T_c and compared to the theoretical prediction of equation 2.26. In general these data show reasonable agreement with the theoretical prediction. It was not possible to accurately measure condensate fractions greater than ~ 0.8 using absorption imaging.

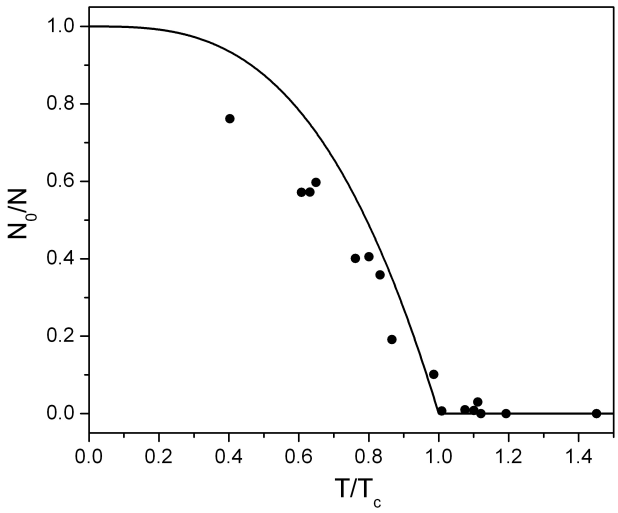

Figure 5.5: ^{87}Rb condensate fraction vs the scaled temperature T/T_c. The experimental data were determined from double Gaussian fits applied to density profiles recorded via absorption imaging. The solid line is the theoretical curve from equation 2.26. At the transition the cloud consists of $1.2(1) \times 10^6$ atoms at 0.37(3) μK.

As discussed in section 2.3.5 the aspect ratio of a thermal cloud dropped from a harmonic trap

$$\frac{\sigma_\rho}{\sigma_z} \rightarrow 1 \tag{5.1}$$

for long times-of-flight, where σ_ρ and σ_z are the radial and axial cloud widths respectively. In contrast to this a condensate will be anisotropic after its expansion during free-fall from an anisotropic confining potential. After the hybrid potential is switched off the internal energy (mean-field energy) in the condensate is converted into kinetic energy in an anisotropic way and

the accelerating force due to the internal mean field energy is proportional to the density gradient. For our initially cigar shaped condensates, the acceleration in the radial direction is larger than that in the axial direction. This results in the aspect ratio of a freely expanding condensate inverting and is an important signature of BEC [127]. Expansion data for the thermal atom and BEC cases dropped from identical potentials are presented in figure 5.6. The fit applied to the thermal atom expansion data in this figure is derived

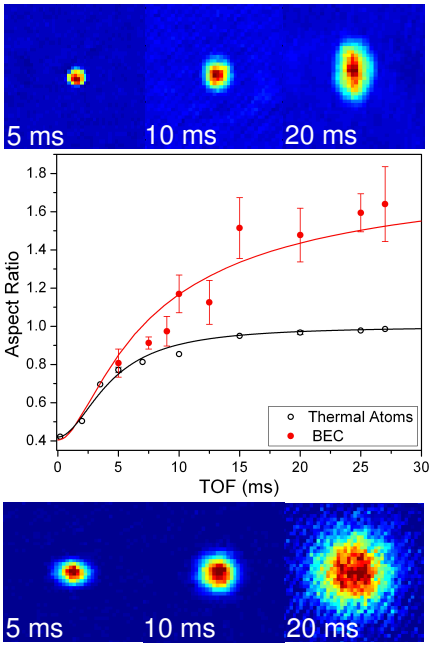

Figure 5.6: Aspect ratios of thermal and condensed atom clouds as a function of the time of flight (TOF). Both clouds were dropped from identical hybrid potentials. Absorption images (400×400 μm) show the cloud shape at various TOFs for condensed (top) and thermal (bottom) atoms. These images clearly show the anisotropic expansion of the BEC while the thermal cloud aspect ratio tends to 1 for long expansion times. The fits applied to the data are described in the text.

from equation 2.48 and has the form

$$\frac{\sigma_\rho}{\sigma_z} = \sqrt{\frac{\omega_\rho^{-2} + t^2}{\omega_z^{-2} + t^2}}. \tag{5.2}$$

The fit gives $\nu_\rho = 71(8)$ Hz and $\nu_z = 30(2)$ Hz and is in reasonable agreement with the predicted trap frequencies of $\nu_\rho = 82$ Hz and $\nu_z = 28$ Hz from a

MATLAB simulation of the potential. As expected these data show that the aspect ratio tends to 1 for long expansion times.

The data measured for the condensate clearly show the anisotropic expansion of the cloud. The fit applied to these data uses the calculated frequencies from the fit to the thermal atoms and numerically solves equations 2.47 to calculate the aspect ratio at each TOF.

5.5 The Crossed Dipole Trap

To align the crossed dipole trap the position of each single beam hybrid trap was independently optimised at separate times to locate the position at which the loading and evaporation were most efficient. When each beam was at the optimum position pure ^{87}Rb condensates containing $\simeq 9 \times 10^5$ atoms could be made in either single beam. These results can be thought of as the ultimate diagnostic for evaporative cooling. This method also allowed the intensity servo-mechanical circuits to be tested individually.

The crossed dipole loading trap contains 6 W in each beam and can be loaded with $6.9(1) \times 10^6$ ^{87}Rb atoms by reducing the magnetic field gradient and final RF frequency to 3 G/cm and 3 MHz respectively over 5 s. The gradient is not switched off completely to ensure that the atoms remain polarised in the $|1, -1\rangle$ state. By linearly reducing the beam powers to 240(6) mW in 5 s pure ^{87}Rb condensates containing $1.9(1) \times 10^6$ atoms can be produced in the crossed dipole trap. The final stage of evaporation in this mostly optical potential has an efficiency of 5.8(3). The open circles in figure 6.3 show the complete trajectory to BEC for ^{87}Rb in the crossed dipole loading trap.

After the transfer into the crossed dipole trap all magnetic sublevels can be confined. At this stage we transfer the atoms into the absolute internal ground states, $|1, +1\rangle$ for ^{87}Rb and $|3, +3\rangle$ for ^{133}Cs. This stage is crucial once we begin to work with ^{133}Cs since this transfer eliminates inelastic two-body losses which have plagued previous attempts to cool ^{133}Cs to degeneracy in magnetic traps [164]. The transfer is achieved using the technique of RF adiabatic rapid passage [75].

5.6 Adiabatic Rapid Passage

The technique of adiabatic rapid passage inverts the atomic spin population by sweeping the system through a resonance. Either the frequency of a coupling RF field or the transition frequency (by changing the applied magnetic field) is varied. To understand this process consider the splitting of the magnetic sublevels of an atom in the presence of a bias field (section 2.5). When an RF field is also applied the energy states of the atom are dressed by the energy of the photon interaction and coupling between different energy states gives rise to a Landau-Zener avoided crossing. Figure 5.7 shows a schematic of a Landau-Zener avoided crossing for the ^{87}Rb $F = 1$ hyperfine ground state with an RF frequency of 1.5 MHz and a Rabi frequency (Ω_{R}) of $2\pi \times 500$ kHz.

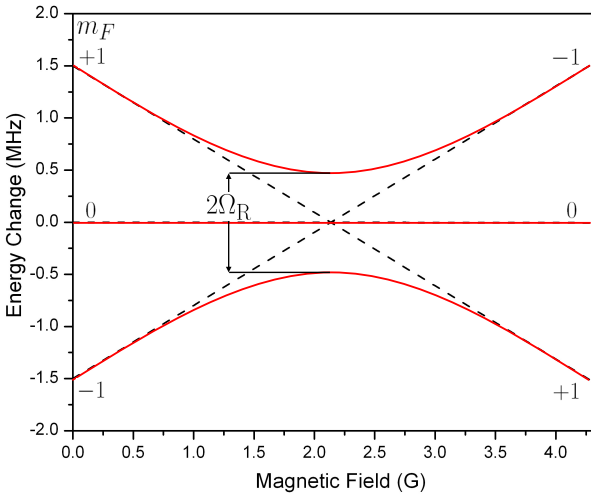

Figure 5.7: Schematic of a Landau-Zener avoided crossing for ^{87}Rb $F = 1$, the Rabi frequency is $2\pi \times 500$ kHz. A 1.5 MHz RF field couples different energy states (red lines) and allows an adiabatic magnetic field ramp to flip the atomic spin from $m_F = -1$ to $+1$ or vice versa.

When crossing the resonance whether the system follows an energy level adiabatically or not depends on how rapidly the energy is changed compared to the minimum energy separation. This can be expressed in terms of the Rabi frequency

$$\Omega_{\mathrm{R}} = \frac{1}{\hbar} g_F \mu_{\mathrm{B}} B_{\mathrm{RF}}, \tag{5.3}$$

which dictates the coupling strength. This must be compared to the rate of change of ω_{Larmor} (equation 2.59) with time

$$\frac{d\omega_{\text{Larmor}}}{dt} = \frac{1}{\hbar} g_F \mu_{\text{B}} \frac{dB}{dt}. \tag{5.4}$$

Note that here the m_F term from equation 2.56 becomes $\Delta m_F = 1$. The probability of non-adiabatic behaviour, *i.e.* that the system will 'jump' from one adiabatic level to another when passing through the avoided crossing is [165]

$$P_{\text{na}} = \exp\left[-\frac{\pi}{2} \frac{\Omega_{\text{R}}^2}{d\omega_{\text{Larmor}}/dt} \right]. \tag{5.5}$$

For efficient transfer a large Rabi frequency (high RF power) and a slow scan of the magnetic field are desirable. Indeed the term 'rapid' is a misnomer from when this technique was developed in nuclear magnetic resonance where relaxation effects destroy spin polarisation.

In practice the technique is performed by switching on an RF field at 1.5 MHz with a power of +24 dBm. This field is transmitted through a homemade coil in an LCR circuit designed to have a resonance at $\simeq$ 1.5 MHz. To perform the simultaneous transfer of both ^{87}Rb and ^{133}Cs a -22.4 G bias field is switched on in 18.0(4) ms and the RF field is then switched off [166]. The bias field has reversed sign compared to section 3.8.3 to shift the field zero upwards. For 1.5 MHz the avoided crossing is located at 2.1 G for ^{87}Rb and 4.3 G for ^{133}Cs. At these points in the field switch on $dB/dt = 1.7$ T/s, which corresponds to $d\omega_{\text{Larmor}}/dt = 2\pi(1.2 \times 10^{10})$ Hz^2.

Figure 5.8 shows a series of absorption images for $F = 1$ ^{87}Rb atoms released from the crossed dipole trap after adiabatic rapid passage as the RF power is increased in steps from 4 to 24 dBm. This effectively increases Ω_{R} from $2\pi \times 8.5$ kHz to $2\pi \times 84.9$ kHz. Stern Gerlach spectroscopy is used to spatially separate atoms in different magnetic sublevels. For these data the 22.4 G field direction was set to move the magnetic field zero above the trap such that atoms in the $m_F = -1$ sublevel are levitated. The measured transfer efficiency from $m_F = -1$ into $m_F = +1$ is 95(2) %. These data compare well to the results predicted by equation 5.5. Qualitatively, these results are strikingly similar to numerical analysis of adiabatic rapid passage in a three-level system [167].

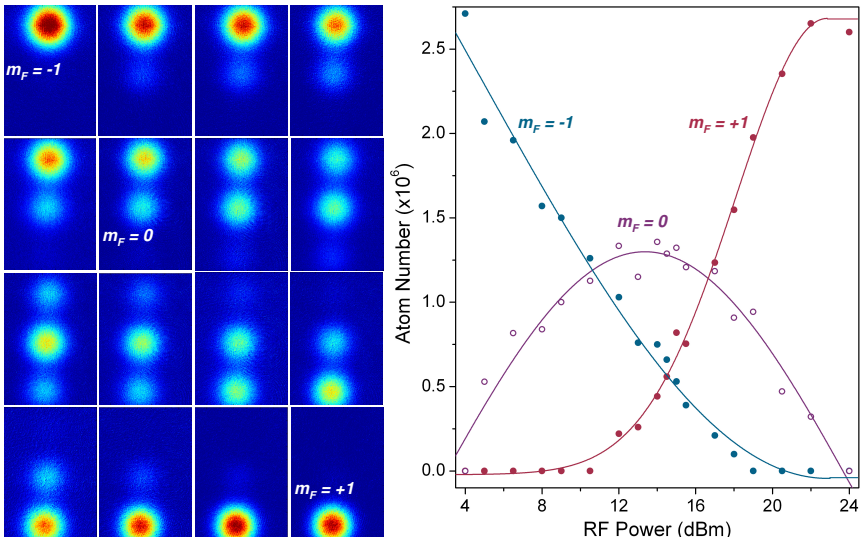

Figure 5.8: Spin transfer by rapid adiabatic passage. Absorption images (3.0×4.5 mm) show the transfer of ^{87}Rb atoms from $m_F = -1$ via $m_F = 0$ into $m_F = +1$. Reading across from top left, progress is seen as the RF power is increased in steps from 4 to 24 dBm. For each image Stern Gerlach spectroscopy spatially separates the different magnetic sublevels prior to the probe pulse driving σ^- transitions in each cloud. The plot shows the measured atom number in each magnetic sublevel as a function of the RF power. The lines are plotted to guide the eye only.

The absorption images in figure 5.8 were recorded by driving σ^- transitions in the atomic clouds. As discussed in section 3.9.1, for a 10 μs probe pulse this results in the final measured optical depth of the $|1, +1\rangle$ atom cloud being ~ 5 % less than that of the initial $|1, -1\rangle$ atom cloud as more numerous and less probable σ^- transitions are required to reach the cycling transition.

5.7 Sympathetic Cooling in ^{87}Rb

To measure the spin purity of the ^{87}Rb atoms after adiabatic rapid passage into the $|1, +1\rangle$ state the crossed dipole trap was loaded with 3.7 W in each beam. The trap depth due to the purely optical potential is equal for each m_F state, however a magnetic field gradient of 13 G/cm and a bias field of -22.4 G (field zero above the trap) were also applied. This modifies the trap-

ping potential as follows. The offset quadrupole potential now only partially levitates the $|1,-1\rangle$ atoms whilst the $|1,+1\rangle$ atoms experience a downwards force equivalent to an acceleration of $\simeq 1.5\ g$ and this modifies the trap depth for each state. The gradient of 13 G/cm was chosen to allow tilting of the trap for the $|1,+1\rangle$ atoms. This behaviour is illustrated in figure 5.9(a) which shows how the trap depths for each m_F state vary as a function of the power in each beam. The dotted line shows the trap depth for the $|1,+1\rangle$ state along the beams. The ratio of trap depths for the $|1,+1\rangle$, $|1,0\rangle$, and $|1,-1\rangle$ states varies from $1.0:1.1:1.9$ to $1.0:1.6:2.3$ for beam powers of 3.7 W and 0.45 W respectively. When the beam powers are reduced this results in the preferential evaporation of the more numerous $|1,+1\rangle$ atoms, the ensemble will then cool via rethermalisation. This evaporation sympathetically cools the $|1,0\rangle$ and $|1,+1\rangle$ atoms with little loss in atom number. As the beam powers are reduced below 0.8 W, the evaporation surface changes from horizontally along the beams to a tilting evaporation in the z-direction. As more $|1,+1\rangle$ atoms are removed the temperature of the other two hyperfine states begins to decrease, as shown in figure 5.9(a). The corresponding changes in atom number are presented in figure 5.9(b) where the false colour absorption images show how the atoms in the less populated states become more visible as the clouds cool and the optical depths increase. This cooling allows the atom number present in each spin state to be accurately measured. After the RF adiabatic transfer, of the remaining trapped atoms, 95.8(7) % are in the $|1,+1\rangle$ state, 3.8(2) % are in the $|1,0\rangle$ state, and 0.4(1) % are in the $|1,-1\rangle$ state.

During the evaporation the $|1,+1\rangle$ atoms form a pure condensate containing $1.4(1)\times10^5$ atoms at a beam power of 0.48 W. All $|1,+1\rangle$ atoms are lost at a beam power of $\simeq$ 0.4 W when the trap depths are 2.6 μK, 4.8 μK and 7.4 μK for the $|1,+1\rangle$ $|1,0\rangle$ and $|1,-1\rangle$ states respectively. At this point the $|1,0\rangle$ atoms are evaporatively cooled and sympathetically cool the $|1,-1\rangle$ atoms, again via tilting evaporation as the beam powers are reduced further. At beam powers of 0.3 W a BEC is produced in the $|1,0\rangle$ state containing $3.0(3)\times10^4$ atoms and the temperature of the thermal $|1,-1\rangle$ atoms is 90(2) nK. Evaporation of the remaining atoms in $|1,-1\rangle$ leads to further cooling of this state, close to degeneracy with a phase-space density

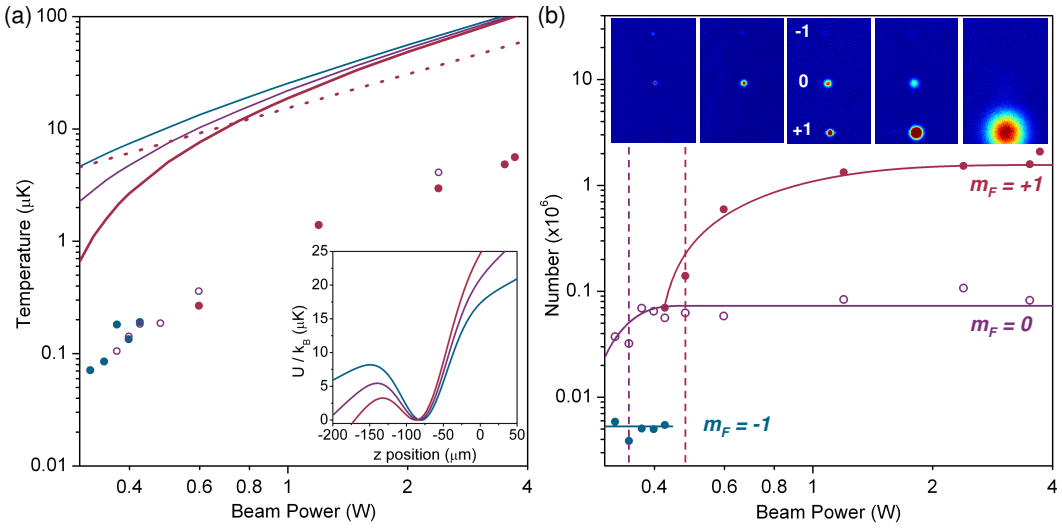

Figure 5.9: Sympathetic cooling of different spin states in the dipole trap. (a) Trap depth and temperatures for each m_F state and (b) atom numbers as a function of the power in each beam. Data are presented for the $|1,+1\rangle$ (red), $|1,0\rangle$ (purple), and $|1,-1\rangle$ (blue) states. In (a) the solid lines indicate the trap depth along z, the dashed line indicates the trap depth along the beams and allows identification of the beam powers at which the evaporation surface switches from horizontal to vertical: these powers are 0.8 W and 0.45 W for $|1,+1\rangle$ and $|1,0\rangle$ respectively. The inset shows the vertical cross-section through the potential minimum for a beam power of 0.45 W and a magnetic field gradient of 13 G/cm. The solid lines in (b) are only to guide the eye and the dashed lines mark the onset of Bose-Einstein condensation. The absorption images in (b) (3.0×4.5 mm) are taken after a Stern-Gerlach time-of-flight and highlight the sympathetic cooling of the $|1,0\rangle$, and $|1,-1\rangle$ states.

of ~ 0.5, after which there are too few atoms to image reliably.

In contrast to this experiment in the main experimental routine the applied +22.4 G bias field shifts the magnetic field zero to below the crossed dipole trap. Now when a magnetic field gradient is applied the $|1,+1\rangle$ atoms are partially levitated while the $|1,-1\rangle$ atoms experience a downwards force. This reverses the order of the preferential evaporation detailed in the above experiment. The reversal of the bias field results in evaporation not only

cooling but also purifying the spin composition by selectively removing the $|1,-1\rangle$ and $|1,0\rangle$ atoms before the direct evaporation of the $|1,+1\rangle$ atoms. The same effect is also observed for ^{133}Cs, leaving just the $|3,+3\rangle$ atoms in the crossed dipole trap.

5.8 A Spinor Condensate in ^{87}Rb

As a final experiment using ^{87}Rb alone in the crossed dipole trap adiabatic rapid passage was performed using a power of 14 dBm. This gave $\simeq 7 \times 10^5$ ^{87}Rb atoms in both the $|1,+1\rangle$ and $|1,-1\rangle$ states and $\simeq 1.3 \times 10^6$ in the $|1,0\rangle$ state, see figure 5.8. After the transfer the 13 G/cm gradient was switched off and the all optical trap depth was identical for all spin states. The dipole trap beam powers were then linearly reduced from 3.7 W to 256 mW in 5 s, this reduced the trap depth to 1.2 μK. The atoms were then held for 1 s in this final potential. During the simultaneous evaporation of all three spin states the $|1,0\rangle$ atoms first formed a condensate of $1.0(2) \times 10^5$ atoms when the trap depth was 3.0 μK, here the beam powers were 330 mW. After the ramp in beam powers and hold all three spin states were degenerate in the same potential. The spinor BEC contained $4.8(2) \times 10^4$ atoms in $|1,+1\rangle$, $7.6(5) \times 10^4$ atoms in $|1,0\rangle$, and $5.4(4) \times 10^4$ atoms in $|1,-1\rangle$. Absorption images taken at various stages along this evaporation trajectory to a ^{87}Rb spinor BEC are presented in figure 5.10. Here Stern-Gerlach spectroscopy is used to spatially separate the different magnetic sublevels, however, note that now the magnetic field zero is positioned below the crossed dipole trap. This results in the $m_F = +1$ atoms being levitated against gravity while the $m_F = 0$ and $m_F = -1$ atoms accelerate downwards at $\simeq g$ and $\simeq 2g$ respectively.

Although sympathetic cooling in ^{87}Rb and spinor condensates have previously been demonstrated over 10 years ago [27, 28] the experiments detailed in sections 5.7 and 5.8 (similar to the data presented in section 4.7) ensure that the character of the crossed dipole hybrid potential can be accurately manipulated and that the potential is very well understood.

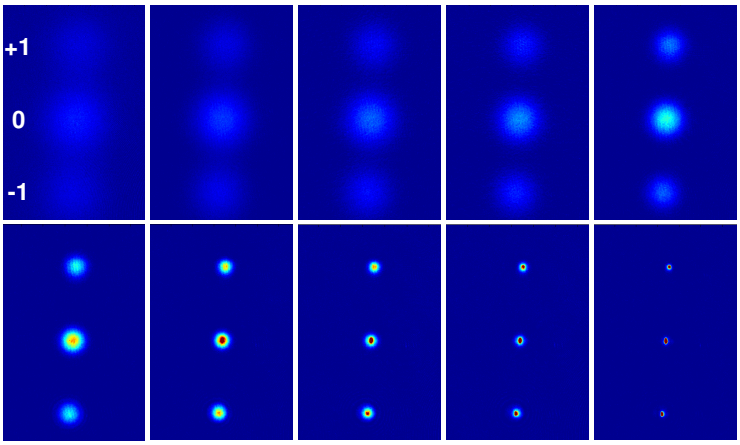

Figure 5.10: Evaporation to degeneracy in a mixture of the $|1,+1\rangle$, $|1,0\rangle$ and $|1,-1\rangle$ spin states in ^{87}Rb . Absorption images (3.0×4.5 mm) show various stages of the evaporation trajectory to a ^{87}Rb spinor BEC. Here the trap depth is reduced from 57 μK to 1.2 μK in 5 s. After a 1 s hold a degenerate mixture is produced containing $4.8(2) \times 10^4$, $7.6(5) \times 10^4$ and $5.4(4) \times 10^4$ atoms in the $|1,+1\rangle$, $|1,0\rangle$ and $|1,-1\rangle$ states respectively.

Chapter 6

An Ultracold Mixture of ^{87}Rb and ^{133}Cs

Once a large number of ^{87}Rb atoms could be efficiently cooled to BEC studies of a mixture of ^{87}Rb and ^{133}Cs could begin by initially adding a small number of ^{133}Cs atoms to the established ^{87}Rb evaporation sequence. By optimising ^{87}Rb alone in the hybrid potential an excellent 'refrigerator' has been constructed for sympathetically cooling ^{133}Cs. In this chapter results from the studies of an ultracold mixture of ^{87}Rb and ^{133}Cs are presented and discussed.

6.1 Precooling and Loading the Dipole Trap

To load the levitated crossed dipole trap, ultracold mixtures of ^{87}Rb and ^{133}Cs are initially collected in the two-species science MOT and transferred to the magnetic quadrupole trap in the ^{87}Rb $|1,-1\rangle$ and ^{133}Cs $|3,-3\rangle$ states. After adiabatic compression to 187 G/cm the magnetic trap initially contains $2.14(5) \times 10^8$ ^{87}Rb atoms at 152(6) μK and $2.0(1) \times 10^7$ ^{133}Cs atoms at 200(8) μK. These parameters correspond to phase space densities of $5(1) \times 10^{-7}$ and $2.6(7) \times 10^{-8}$ for ^{87}Rb and ^{133}Cs respectively. As discussed in section 2.6 when using forced RF evaporation to cool the mixture in the magnetic quadrupole trap the trap depth defined by the RF frequency is three times deeper for ^{133}Cs than for ^{87}Rb. This allows the selective RF

Stage	t_{stage} (s)	t_{total} (s)	f_{start} (MHz)	f_{stop} (MHz)	RF amp. (dBm)
1	30.0	30.0	60.0	20.5	-0.5
2	12.5	42.5	20.5	12.3	-0.5

Table 6.1: Optimised parameters for the two RF stages applied to the ^{87}Rb - ^{133}Cs mixture to evaporatively cool ^{87}Rb and sympathetically cool ^{133}Cs in the magnetic trap. Both RF cuts follow linear ramps in frequency.

evaporation of ^{87}Rb while interspecies elastic collisions sympathetically cool ^{133}Cs. The two optimised RF stages used for the sympathetic cooling of ^{133}Cs via ^{87}Rb in the magnetic quadrupole trap are summarised in table 6.1. The results of this evaporative and sympathetic cooling in the magnetic trap for both species are presented in table 6.2 and plotted in figure 6.1.

In the magnetic trap the evaporation efficiency of ^{87}Rb alone is 2.6(2) (circular points in figure 6.1). For the two-species sympathetic cooling case (square data points in figure 6.1) the cooling efficiencies are 0.43(3) and 5.2(4) for ^{87}Rb and ^{133}Cs respectively. The ^{133}Cs efficiency ranges from 5.2(4) to 11.3(4) depending on the initial number of ^{133}Cs atoms. As expected the efficiency of the ^{87}Rb cooling has decreased during the sympathetic cooling compared to the single species case due to the additional heat load from the ^{133}Cs atoms. In contrast, the ^{133}Cs cooling efficiency is very high in accord with

	N ($\times 10^7$)		T (μK)		PSD ($\times 10^{-7}$)		Efficiency γ	
Stage	^{87}Rb	^{133}Cs	^{87}Rb	^{133}Cs	^{87}Rb	^{133}Cs	^{87}Rb	^{133}Cs
MT loaded	21.4(5)	2.0(1)	152(6)	200(8)	2.0(2)	0.26(1)	-	-
1	5.0(2)	1.3(2)	103(5)	109(4)	7.1(3)	2.7(1)	0.20(1)	5.4(9)
2	1.7(1)	0.91(3)	68(2)	68(3)	15.7(5)	15.0(6)	0.7(1)	4.9(8)

Table 6.2: Forced RF evaporation and sympathetic cooling results for ^{87}Rb and ^{133}Cs in the magnetic trap at 187 G/cm. Atom number, temperature, phase-space density (PSD) and evaporation efficiency data are presented for both species after adiabatic compression in the magnetic trap and after each optimised RF ramp.

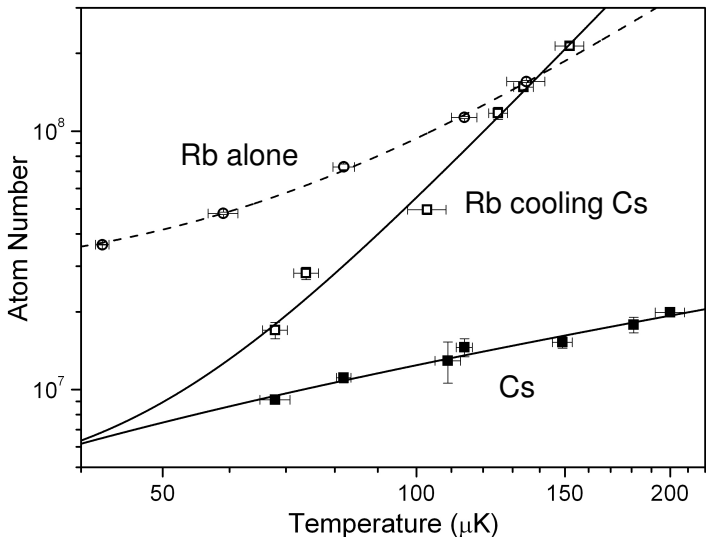

Figure 6.1: Sympathetic cooling of ^{133}Cs by ^{87}Rb in the magnetic trap. Forced RF evaporation is used to cool ^{87}Rb while interspecies elastic collisions cool ^{133}Cs sympathetically. Open (closed) symbols show data for ^{87}Rb (^{133}Cs). Circular symbols show the evaporative cooling of ^{87}Rb alone. Square symbols show the two species sympathetic cooling case. The lines fit to the data are to guide the eye only.

the successful demonstration of sympathetic cooling. During the sympathetic cooling the ^{133}Cs temperature is always observed to be in excellent agreement with the ^{87}Rb temperature and indicates rapid cross thermalisation between the two species. This observation, and the high efficiency of the sympathetic cooling imply a large interspecies elastic collision rate. This implication is consistent with the latest theoretical refinement of the interspecies collision potential [92] which shows excellent agreement with the published Feshbach spectrum [88, 90] and indicates a background interspecies scattering length of $\simeq 650\ a_0$ for the states used in this work.

The evaporative and sympathetic cooling is performed until Majorana losses begin to limit the lifetime of the mixture. This limit occurs at a temperature of 68(3) μK when the ^{133}Cs lifetime is 10(3) s. For the two-species case in figure 6.1 there are $1.7(1) \times 10^7$ ^{87}Rb and $9.1(3) \times 10^6$ ^{133}Cs atoms remaining in the magnetic trap. At this point the crossed dipole trap is loaded via elastic collisions by simply reducing the magnetic field gradient over 12 s to 29 G/cm.

This final magnetic gradient is just below the 30.5 G/cm (31.1 G/cm) required to levitate ^{87}Rb (^{133}Cs) and ensures that only atoms loaded into the hybrid potential remain. At the same time the final RF frequency is reduced to a value between 2.3 - 3.0 MHz to control the composition of the mixture loaded into the dipole trap. The resulting loading is highly efficient with up to 50 % of the ^{133}Cs atoms transferred into the dipole trap. Once the mixture is loaded into the levitated crossed dipole trap the initial phase-space densities are typically $\simeq 10^{-3}$ for ^{87}Rb and $\simeq 5 \times 10^{-4}$ for ^{133}Cs. These values represent more than a factor of 200 (400) increase for ^{87}Rb (^{133}Cs) compared to the final phase-space densities in the magnetic trap. This large increase results from an effect analogous to the use of a dimple potential [12]. As the trap volume expands the shape of the trap is modified and leads to a change in the phase-space density, even at constant entropy [104]. In this case the effect is pronounced as the transfer both decreases the temperature and increases the phase-space density.

Immediately after loading the dipole trap the atomic spins of the mixture are flipped into $|1, +1\rangle$ for ^{87}Rb and $|3, +3\rangle$ for ^{133}Cs via adiabatic rapid passage as a +22.4 G bias field is turned on in 18 ms. This transfer into the absolute ground state means that inelastic two-body losses are suppressed due to energetic reasons [104]. At 22.4 G the ratio of elastic to inelastic three-body collisions in ^{133}Cs is favourable for efficient evaporation [80].

6.2 Interspecies Three-Body Loss

Once loaded into the levitated crossed dipole trap the mixture rapidly comes into thermal equilibrium with the potential at $k_{\mathrm{B}}T \approx U_{\mathrm{Rb}}/10$, where U_{Rb} is the dipole trap depth for ^{87}Rb. Here the initial peak atomic densities for both species are typically $\gtrsim 10^{13}$ cm^{-3}. When both ^{87}Rb and ^{133}Cs are present in the trap at these high densities very strong interspecies inelastic losses are observed, figure 6.2. The fast loss of the minority species from the trap shown in figure 6.2 is purely due to inelastic three-body collisions. The initial decrease of the majority species includes a significant contribution from plain evaporation from the trap.

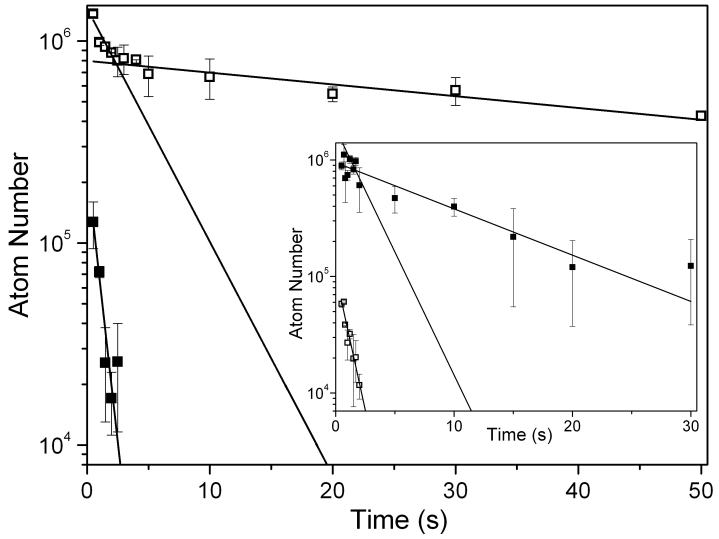

Figure 6.2: Interspecies three-body loss in the crossed dipole trap. Open (closed) symbols show data for ^{87}Rb (^{133}Cs) in the $|1,+1\rangle$ ($|3,+3\rangle$) state. The data are fit with a double exponential function to determine trap lifetimes. In the main plot ^{133}Cs is the minority species and the lifetimes are ^{133}Cs $\tau = 0.8(1)$ s, ^{87}Rb $\tau_1 = 4(1)$ s, and ^{87}Rb $\tau_2 = 70(10)$ s. In the inset ^{87}Rb is the minority species and the lifetimes are ^{87}Rb $\tau = 0.9(2)$ s, ^{133}Cs $\tau_1 = 2(1)$ s, and ^{133}Cs $\tau_2 = 10(3)$ s.

Three-body losses scale with the mean squared density, $\langle n^2 \rangle$, therefore these collisions are most prevalent at the trap centre causing the coldest atoms to be lost predominantly. This 'anti-evaporation' leads to both atom loss and heating and is a major hurdle when trying to achieve a high phase-space density mixture. The heating leads to further loss from the trap through evaporation and contaminates the measurement of the three-body loss rate. A full analysis of the evolving densities, n_{Rb} and n_{Cs}, using two coupled differential rate equations [168]

$$\frac{dn_{\mathrm{Rb}}}{dt} = -\beta_{\mathrm{Rb}} n_{\mathrm{Rb}} - 2L_3^{\mathrm{RbRbCs}} n_{\mathrm{Rb}}^2 n_{\mathrm{Cs}} - L_3^{\mathrm{RbCsCs}} n_{\mathrm{Rb}} n_{\mathrm{Cs}}^2, \tag{6.1}$$

$$\frac{dn_{\mathrm{Cs}}}{dt} = -\beta_{\mathrm{Cs}} n_{\mathrm{Cs}} - L_3^{\mathrm{RbRbCs}} n_{\mathrm{Rb}}^2 n_{\mathrm{Cs}} - 2L_3^{\mathrm{RbCsCs}} n_{\mathrm{Rb}} n_{\mathrm{Cs}}^2, \tag{6.2}$$

is therefore not performed. Here β governs the change in density due to collisions with the background gas. For a two-species mixture there are two interspecies three-body loss rate coefficients, for example the coefficient

L_3^{RbRbCs} dictates the loss rate due to three-body collisions between two ^{87}Rb atoms and one ^{133}Cs atom.

A calculation is performed in place of this full analysis that uses the mean atomic density for each species, assumes the trap lifetime is due exclusively to three-body losses and does not account for any evaporation from the trap. This makes the calculated loss rate coefficients upper limits but is useful in obtaining an order of magnitude estimate. These assumptions allow the three-body loss rate coefficients to be estimated using

$$L_3\langle n^2\rangle = \frac{1}{\tau}. \tag{6.3}$$

To test this method the single species ^{133}Cs case was first investigated, inset of figure 6.2 for $t \geq 5$ s. Here from $t = 5$ s to $t = 30$ s the ^{133}Cs peak density, n_0, decreases from $2.7(6) \times 10^{13}$ cm^{-3} to $8(2) \times 10^{12}$ cm^{-3}, this gives a mean peak density of $1.7(3) \times 10^{13}$ cm^{-3}. The mean density, $\langle n\rangle = n_0/\sqrt{8}$, is $6(1) \times 10^{12}$ cm^{-3} and so the mean squared density, $\langle n^2\rangle = \frac{8}{\sqrt{27}}\langle n\rangle^2$, is $6(1) \times 10^{25}$ cm^{-6}. Using the measured lifetime of 10(3) s equation 6.3 gives $L_3 = 1.8(6) \times 10^{-27}$cm^6/s, in agreement with previous measurements [12]. It is this three-body loss in ^{133}Cs that results in the single species trap lifetime (for $t \geq 5$ s) being a factor of seven shorter than that for ^{87}Rb.

Similar calculations for the two species cases use the minority species trap lifetimes and yield upper limits for the interspecies three-body loss rate coefficients of $\sim 10^{-25} - 10^{-26}$ cm^6/s. The three-body loss rate coefficients scale as $L_3 = 3C\frac{\hbar}{m}a^4$, where C is a dimensionless factor between 0 and ~70, m is the reduced mass and a is the scattering length [169]. The current best estimate [90, 92] of the interspecies scattering length, $a_{\mathrm{RbCs}} \approx 650\ a_0$, would lead to a *maximum* three-body loss rate of $L_3 \sim 3 \times 10^{-25}$ cm^6/s in reasonable agreement with our simple estimates.

6.3 ^{133}Cs Bose-Einstein Condensation

Similar to ^{87}Rb, initial experiments using ^{133}Cs involved simply loading ^{133}Cs alone into the magnetic quadrupole trap. The $1.29(5) \times 10^8$ ^{133}Cs atoms loaded into the magnetic trap were first precooled using forced RF evaporation before transferring the coldest atoms into the levitated crossed dipole

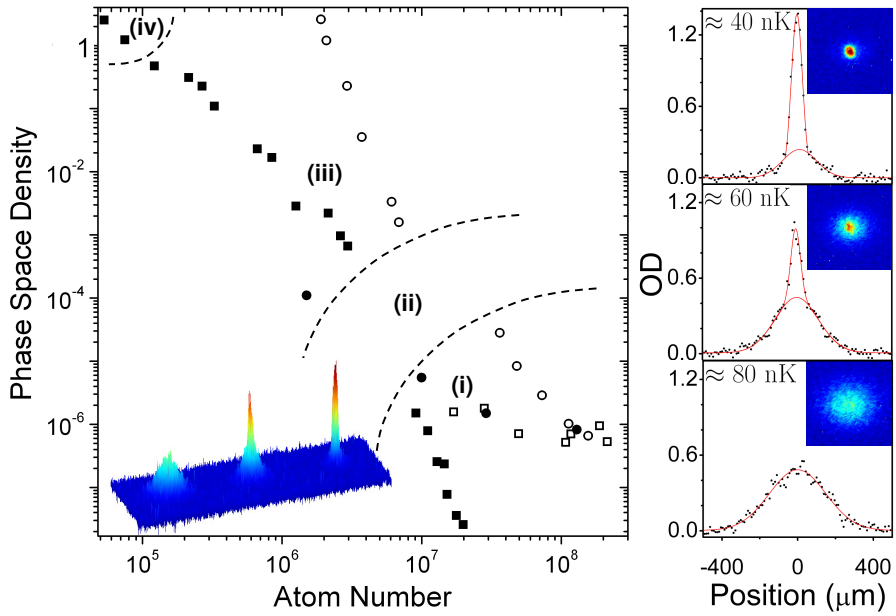

Figure 6.3: Trajectory to ^{133}Cs BEC via sympathetic cooling with ^{87}Rb (squares). Open (closed) symbols show ^{87}Rb (^{133}Cs) data. Circles show single species data for comparison. The trajectory gradient indicates the cooling efficiency. The different regions show: (i) RF evaporation in the magnetic quadrupole trap. (ii) Dipole trap loading and internal state transfer. (iii) Evaporation by reducing the dipole trap beam powers. (iv) Evaporation by trap tilting. Inset: 3D rendering of the density distribution as the cloud is condensed. Right: absorption images (350 × 350 μm) and cross sections of the ^{133}Cs cloud near the BEC phase transition.

trap. Preliminary data show that the evaporation of ^{133}Cs alone in the quadrupole trap has an efficiency of 1.1(2) and 15% of the remaining atoms are transferred into the loading dipole trap (● in figure 6.3). This gives 1.5(3) × 10^6 ^{133}Cs atoms in the loading hybrid trap at 35(4) μK. At present it is not possible to produce ^{133}Cs condensates by loading only ^{133}Cs into the magnetic trap due to the poor transfer into the crossed dipole trap. In contrast, by loading only ^{87}Rb initially it is possible to form condensates of up to 1.9(1) × 10^6 atoms (○ in figure 6.3) [166]. For this trajectory the evaporation efficiencies of ^{87}Rb are 2.6(2) in the magnetic trap and 5.8(3) in the levitated crossed dipole trap.

To create ^{133}Cs condensates a mixture containing 2.1(1) × 10^8 ^{87}Rb and

$2.0(2) \times 10^7$ ^{133}Cs atoms is loaded into the quadrupole trap. For this two-species case the evaporation efficiencies in the magnetic trap are 0.42(3) and 5.2(4) for ^{87}Rb and ^{133}Cs respectively, as we sacrifice ^{87}Rb to sympathetically cool ^{133}Cs (□ and ■ in figures 6.1 and 6.3 (i) respectively). As the magnetic gradient is reduced to load the dipole trap the RF frequency is simultaneously reduced to 2.3 MHz to optimise the transfer of ^{133}Cs whilst at the same time removing all of the ^{87}Rb. The resulting loading is highly efficient with up to $\sim$ 50 % of the ^{133}Cs atoms transferred into the dipole trap at an initial temperature of 28(3) μK with a phase-space density of $6.6(2) \times 10^{-4}$. By loading ^{133}Cs alone into the crossed dipole trap the strong interspecies three-body losses presented in section 6.2 are avoided. The enhanced loading of ^{133}Cs in the presence of ^{87}Rb compared to the ^{133}Cs alone case (● in figure 6.3) is again consistent with the existence of a large interspecies scattering length [90, 92].

To proceed the ^{133}Cs atoms are transferred into the $|3, +3\rangle$ state with $\sim$ 95 % efficiency using RF adiabatic rapid passage. This transfer eliminates inelastic two-body losses which have plagued previous attempts to cool ^{133}Cs to degeneracy in magnetic traps [164]. Operating in the vicinity of the broad zero-crossing in the scattering length near 17 G gives precise control of the elastic collision rate. We observe efficient evaporation and can produce condensates for fields between 21 and 24 G, and typically operate at 22.4 G where $a_{\mathrm{Cs}} = 280\ a_0$. The majority of the evaporation is performed by logarithmically reducing the beam powers from 6 W to 48(3) mW over 9.5 s. This stage reduces the ^{133}Cs levitated crossed dipole trap depth to 850 nK and weakens the trap by reducing the axial and radial trap frequencies to 10.8 Hz and 55.7 Hz respectively. The final stage of evaporation to degeneracy is implemented by increasing the magnetic field gradient to 35.4(1) G/cm over 2.0 s. This tilts the trapping potential, thereby lowering the trap depth to 530 nK whilst leaving the trap frequencies largely unchanged [83]. With this approach we achieve an evaporation efficiency of 2.1(1) for ^{133}Cs alone in the dipole trap and produce pure single species condensates of up to $6.2(1) \times 10^4$ atoms. Figure 6.3 summarises the trajectory to ^{133}Cs BEC and shows both absorption images and cross-sections as the ^{133}Cs cloud is cooled through the BEC transition.

6.4 A Tunable Quantum Gas

In a quantum degenerate mixture it is ultimately desirable to have control of either the interspecies or intraspecies interactions. As discussed in section 1.3 the scattering length of the $|3,+3\rangle$ state in ^{133}Cs has a rich structure with many broad and narrow Feshbach resonances which are readily accessible at low magnetic fields. These offer precise control of the scattering length and hence the atomic scattering properties. This unique tunability can be exploited by dynamically changing the scattering length to vary the mean field interaction of a ^{133}Cs condensate (equation 2.44).

In ^{133}Cs there exists a broad Feshbach resonance in collisions between two atoms in the $|3,-3\rangle$ state at a bias field of $\simeq 8$ G, see figure 1.1. This resonance originates from a large avoided crossing due to a $6(s)$ molecular bound state. The $6(s)$ notation refers to the $F=6$, $l=0$ molecular state, where F is the total internal angular momentum and l is the rotational angular momentum. For ^{133}Cs atoms in $|3,+3\rangle$, this molecular state becomes the last bound state for magnetic fields greater than 20 G and proceeds just below the dissociation limit. This has a profound effect on the scattering length of ^{133}Cs atoms in the $|3,+3\rangle$ state [77]. The slowly approaching molecular state just below threshold results in a slowly increasing scattering length at and above the zero crossing near 17 G. The strength of this resonance, bridging the Feshbach resonance at $\simeq 8$ G for atoms in $|3,-3\rangle$ to the Ramsauer-Townsend transmission [170] near 17 G for $|3,+3\rangle$ atoms is effectively as wide as 25 G.

Here we demonstrate the ability to tune the intraspecies interactions in a ^{133}Cs BEC containing $3.7(3)\times 10^4$ atoms using this zero crossing in the scattering length. It was crucial that for each scattering length the ^{133}Cs BEC atom number remained constant as $E_{\rm rel}\propto (N)^{2/5}$ (equations 2.37 and 2.44), where N is the atom number. For each data point a ^{133}Cs BEC was initially made at a bias field of 22.4 G. The field was then non-adiabatically jumped to a value between 15 G and 26 G in 400 μs as the levitated crossed dipole trap was simultaneously switched off. The ^{133}Cs cloud was then levitated at each bias field for 45 ms plus a 5 ms free time of flight prior to an absorption image probing the cloud. By measuring the time of flight expansion of the ^{133}Cs condensate as the magnetic field was varied in the vicinity of the zero

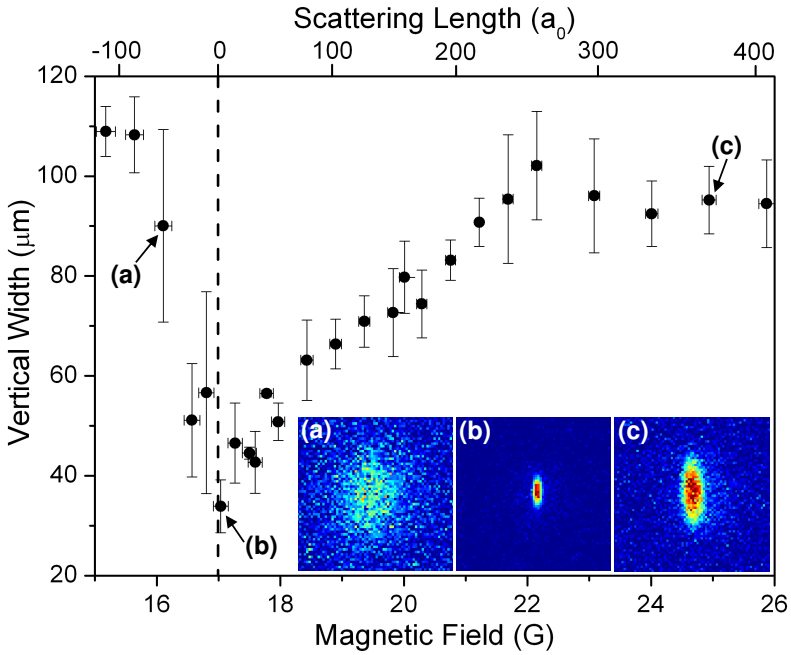

Figure 6.4: Vertical width ($1/\sqrt{e}$ half width of a Gaussian fit) of the ^{133}Cs condensate containing $3.7(3) \times 10^4$ atoms as a function of the magnetic field applied during a 50 ms time of flight expansion. For the first 45 ms the atoms are levitated. The absorption images (600×600 μm) correspond to the labelled data points and highlight three scattering length regimes: (a) negative, (b) zero (dashed line) and (c) positive.

crossing three different regions of self-interaction were demonstrated and are presented in figure 6.4 [12].

As expected below 17 G the scattering length is negative, here strong attractive interactions cause the condensate to collapse [126] resulting in a substantial loss of atoms and a large momentum spread. At 17 G the condensate is essentially non-interacting and behaves like an ideal Bose gas. The near-zero interaction energy results in minimal expansion of the cloud and the condensate is referred to as 'frozen'. For the positive scattering lengths above 17 G, the condensate is stable and repulsive interactions lead to a strong mean-field expansion where $E_{\rm rel} \propto a'$.

6.5 An Ultracold Molecular Gas

To develop experimental protocols and detection methods the magneto-association of Cs_2 dimers was explored using a well characterised ^{133}Cs Feshbach resonance [79]. The starting point of this experiment was a two component ^{133}Cs cloud of $6.3(7) \times 10^4$ atoms in the $|3, +3\rangle$ state at a temperature of 56(5) nK. This was produced using the experimental procedure detailed in section 6.3 but with a final tilt gradient of 34.6(1) G/cm.

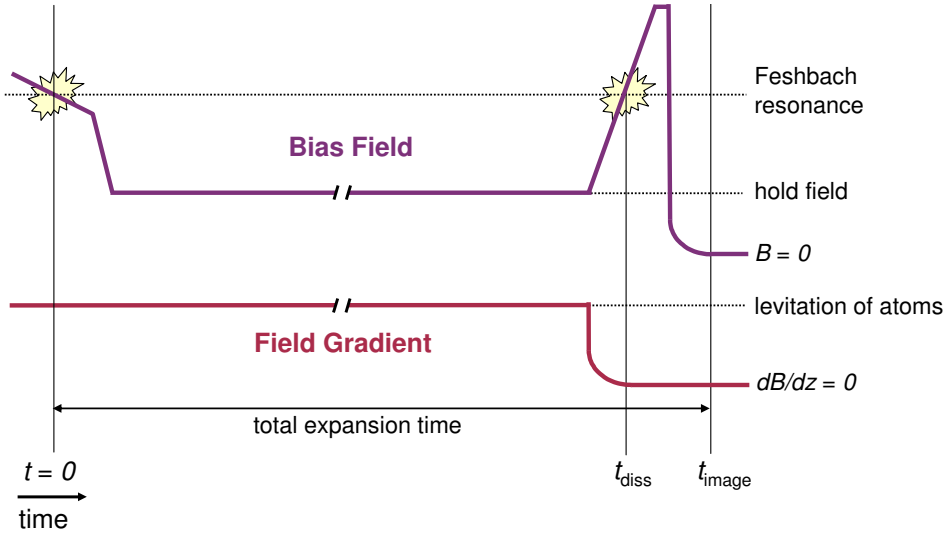

Figure 6.5: Schematic of the magnetic bias field (top) and magnetic gradient (bottom) ramps performed to magneto-associate and spatially separate $^{133}Cs_2$ dimers from an ultracold ^{133}Cs atomic cloud before dissociating the molecules back into atoms for imaging. Here the magnetic gradient was set to levitate the ^{133}Cs atoms during a variable hold time. In a separate experiment the gradient was jumped immediately after magneto-association (t= 0) to a value to levitate the molecules.

The $|3, +3\rangle$ state used has a $4(g)4$ Feshbach resonance at 19.8 G [171] that is estimated to be 5 mG wide [79]. The $4(g)4$ notation refers to the $F = 4, l = 4$ and $m_F = 4$ molecular state, where F is the total internal angular momentum, l is the rotational angular momentum, and m_F is the projection along the quantization axis. ^{133}Cs atoms are magneto-associated into $^{133}Cs_2$ Feshbach molecules by sweeping the magnetic field across this resonance from 19.90(2) G at a rate of 47 G/s to 19.70(2) G. The dipole trap is then switched

off and the field is rapidly jumped to 17 G to null atomic interactions. Stern-Gerlach separation is immediately applied to spatially separate the atomic and molecular samples. The magnetic field gradient is fixed at 31.1 G/cm to levitate the atomic cloud. During this variable hold time the molecules fall away from the levitated atoms due to their smaller magnetic moment to mass ratio. Before absorption imaging can be used to simultaneously probe both clouds the $^{133}Cs_2$ Feshbach molecules must be converted back into ^{133}Cs atoms. To dissociate the molecules the magnetic field is jumped back across the resonance to 21 G in 130 μs. This non-adiabatic reverse sweep brings the molecules above the scattering continuum, from here they rapidly dissociate into free atoms. Finally the magnetic gradient is switched off for a 2 ms free expansion before an absorption image reveals the distribution of the dissociated molecules and the free atoms. The ramps of the magnetic field and magnetic gradient during this experiment are illustrated in figure 6.5.

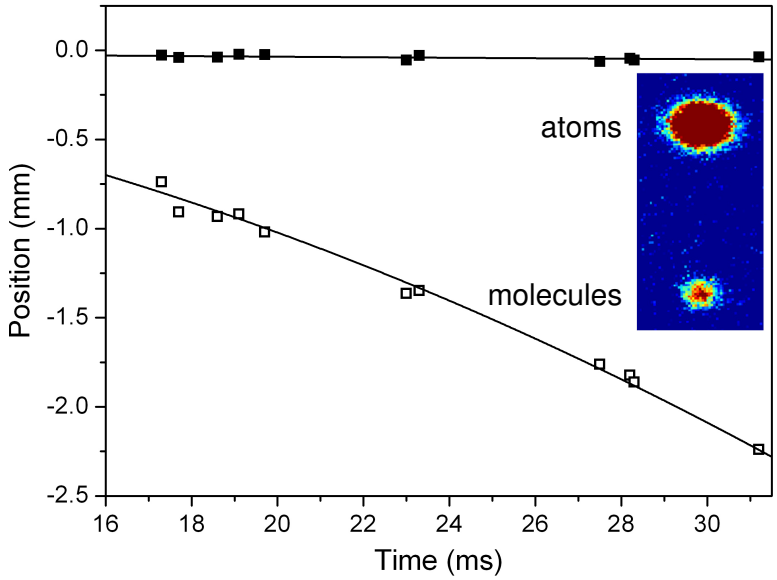

Figure 6.6: The production of Cs_2 molecules using a Feshbach resonance. Open (closed) symbols mark the molecular (atomic) clouds position as a function of the levitation time at a bias field of 17 G (at z=0). From these data a molecular acceleration of 3.86(4) m/s^2 is calculated, this corresponds to $\mu = 0.92(1)\mu_B$. Inset: A typical absorption image taken after the molecules have been dissociated back into atoms. At the top the levitated atomic cloud contains 5.1(3) $\times$ 10^4 atoms, the smaller molecular sample below contains 7.5(4) $\times$ 10^3 Cs_2 Feshbach molecules.

The atomic and molecular clouds' positions as a function of the levitation time are presented in figure 6.6. The inset of this figure shows a typical absorption image; at the top a large atom cloud is levitated while a smaller molecular cloud falls away. Typical magneto-association efficiencies are ∼12% and samples containing 7,000 molecules at 2.4(9) nK are produced from the high phase-space density ^{133}Cs cloud. The molecular acceleration can be measured from the data presented in figure 6.6 and this allows the magnetic moment of the Cs_2 molecules to be calculated. The molecular acceleration, a_{mol}, at 31.1 G/cm is measured to be 3.86(4) m/s^2, using

$$\mu = \frac{m(g - a_{\mathrm{mol}})}{\partial B/\partial z} \tag{6.4}$$

where g is the acceleration due to gravity and m is the molecular mass, this corresponds to a magnetic moment $\mu = 0.92(1)\mu_{\mathrm{B}}$. This value concurs with another measurement performed by levitating the molecular cloud at 51.4(2) G/cm. These results are in good agreement with previous work and theoretical calculations [79].

6.6 A Dual-Species BEC of ^{87}Rb and ^{133}Cs

By making several minor changes to the ^{133}Cs BEC experimental procedure (section 6.3) it is possible to create a degenerate mixture of ^{87}Rb and ^{133}Cs. Firstly the number of ^{133}Cs atoms loaded into the magnetic trap is reduced to $2.7(1) \times 10^6$. This reduces the heat load on the ^{87}Rb during the sympathetic cooling and improves the cooling efficiencies in the magnetic trap to 1.7(2) for ^{87}Rb and 11.3(4) for ^{133}Cs. Loading the dipole trap results in a mixture of $2.8(2) \times 10^6$ ^{87}Rb and $5.1(3) \times 10^5$ ^{133}Cs atoms at a temperature of 9.6(1) μK following the spin flip into the ^{87}Rb $|1, +1\rangle$ and ^{133}Cs $|3, +3\rangle$ states. Here the initial peak densities are $7.4(6) \times 10^{12}$ cm^{-3} for ^{87}Rb and $1.2(1) \times 10^{13}$ cm^{-3} for ^{133}Cs. As discussed in section 6.2 at these high densities we observe very strong interspecies inelastic losses with an upper limit of $\sim 10^{-25} - 10^{-26}$ cm^6/s for the interspecies three-body loss rate coefficients.

To combat the strong interspecies inelastic losses fast evaporative cooling is performed by reducing the beam powers logarithmically to 120 mW in just 1.0 s, corresponding to a final trap depth of 2 μK for ^{87}Rb. Taking

into account the adiabatic expansion of the cloud resulting from the commensurate relaxation of the trap frequencies, this corresponds to an effective reduction in the trap depth by a factor of 7. The result is a factor of ~ 3 reduction in the density and consequently an order of magnitude increase in the lifetime of ^{133}Cs against interspecies three-body collisions. Overall the conditions for evaporative cooling are improved by this fast reduction in the dipole trap power, despite the associated decrease in the elastic collision rate from 180(10) s^{-1} (690(40) s^{-1}) to 6.4(4) s^{-1} (17(2) s^{-1}) for ^{87}Rb (^{133}Cs). After this stage of evaporation the hybrid potential contains $4.7(1) \times 10^5$ ^{87}Rb atoms and $1.5(1) \times 10^5$ ^{133}Cs atoms at phase-space densities of $5.3(1) \times 10^{-2}$ and $2.1(1) \times 10^{-2}$ respectively.

Further evaporation is then performed by linearly reducing the beam powers to 48 mW in 2.5 s. Finally, by tilting the trap by increasing the applied magnetic field gradient to 32.7(1) G/cm over 1.0 s dual-species condensates are produced in the same trapping potential containing up to $\sim 2.0 \times 10^4$ atoms of each species. The complete trajectory to a dual-species BEC of ^{87}Rb and ^{133}Cs is presented in figure 6.7. The efficiencies of the evaporative and sympathetic cooling in the dipole trap are 1.8(2) and 2.8(5) for ^{87}Rb and ^{133}Cs respectively. The data show that despite strong interspecies inelastic losses the sympathetic cooling of ^{133}Cs via ^{87}Rb in the dipole trap is still more efficient than the direct evaporation of ^{133}Cs alone (figure 6.3).

6.7 Immiscibility in a Degenerate Mixture

Once the dual-species BEC is made a dramatic spatial separation of the two condensates in the trap is observed, revealing the mixture to be immiscible at 22.4 G, figure 6.8. The resulting density profile for each species is a stark contrast to the symmetry of the potential and the density profiles observed for each single species condensate, figure 6.3. As discussed in section 2.4 for an immiscible quantum degenerate mixture, the relative strength of the atomic interactions [129]

$$\Delta = \frac{g_{\mathrm{RbCs}}}{\sqrt{g_{\mathrm{Rb}} g_{\mathrm{Cs}}}} \simeq \frac{a_{\mathrm{RbCs}}}{\sqrt{a_{\mathrm{Rb}} a_{\mathrm{Cs}}}} > 1. \tag{6.5}$$

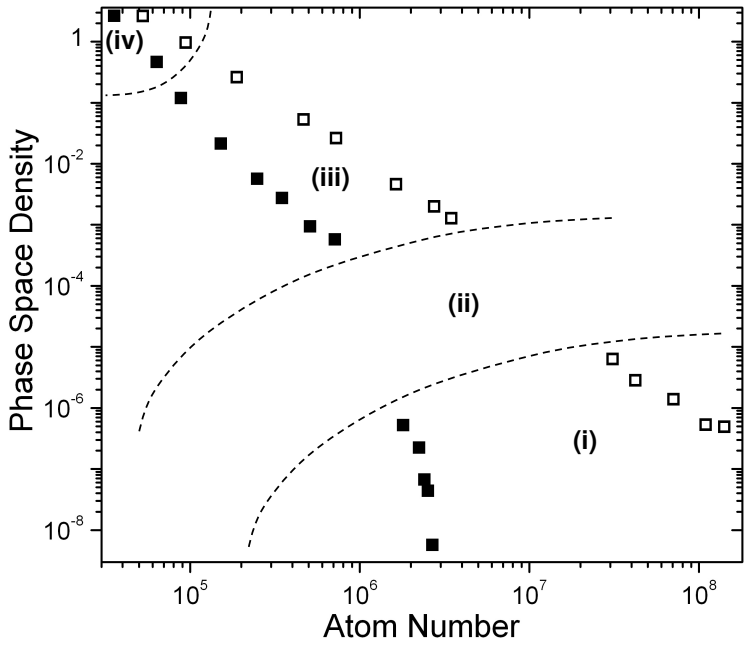

Figure 6.7: Trajectory to a dual-species BEC of ^{87}Rb and ^{133}Cs in the levitated crossed dipole trap. The trajectory is divided into four sections: (i) RF evaporation in the magnetic quadrupole trap. (ii) Dipole trap loading and internal state transfer. (iii) Evaporation by reducing the dipole trap beam powers. (iv) Evaporation by trap tilting. Open (closed) symbols show data for ^{87}Rb (^{133}Cs).

At 22.4 G $a_{\mathrm{Rb}} = 100\ a_0$ and $a_{\mathrm{Cs}} = 280\ a_0$, so that the observation of immiscibility implies $a_{\mathrm{RbCs}} > 165\ a_0$; again consistent with the current best estimate, $a_{\mathrm{RbCs}} \approx 650\ a_0$ [90, 92].

The bimodal distributions in figure 6.8 show that the immiscible behavior is exclusive to the condensed atoms. The immiscible condensates always form one of three structures, either one of two possible symmetric cases (▲ and ● in figure 6.8) or an asymmetric case (□ in figure 6.8). Qualitatively, these observations are strikingly similar to the symmetric and asymmetric structures predicted for an immiscible binary condensate based upon numerical simulations of two coupled Gross-Pitaevskii equations [172]. Experimentally, the structures are correlated with the number of atoms in each condensate. Altering the number of ^{133}Cs atoms loaded into the trap, allows navigation between the three structures. These structures may be related to the order in which the condensates form in the trap. Here the first condensate to

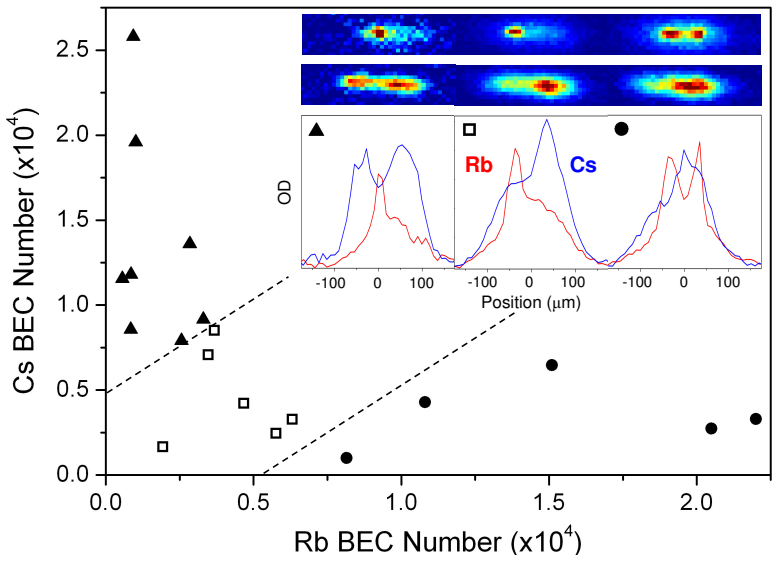

Figure 6.8: Immiscibility in a quantum degenerate mixture of ^{87}Rb and ^{133}Cs. Three distinct structures are observed (▲, □ and •) correlated with the number of atoms in each condensate. Absorption images and cross-sections of ^{87}Rb (red) and ^{133}Cs (blue) highlight these structures. The optical depth scales of the cross-sections are 0–1.0 (▲) and 0–2.6 (□ and •). Each image is 350 × 100 μm.

form would be expected to occupy the centre of the trap before the second species condensed around it leading to the symmetric cases. If both species condensed at the same time both would be displaced from the trap centre resulting in the asymmetric case. To test this theory more data is required during the final moments of evaporation. The strong interspecies losses currently make the formation of a dual-species condensate with $N_{\mathrm{Rb}} + N_{\mathrm{Cs}} > 2.5 \times 10^4$ atoms a challenge and lead to the asymptotic nature of the data in figure 6.8.

The immiscible nature of the mixture may aid the formation of the dual-species condensate by suppressing the interspecies inelastic losses as the mixture condenses. In the future, the miscibility will be explored by Feshbach tuning both a_{Cs} and a_{RbCs} in order to test this assertion [36]. Crucially, thermal clouds very close to degeneracy remain miscible, enabling the efficient magneto-association [74] of RbCs molecules in future experiments, as the first step towards the creation of a dipolar molecular quantum gas.

6.8 An Interspecies Feshbach Resonance

Once a high phase-space density ^{87}Rb - ^{133}Cs mixture could be readily made in the levitated crossed dipole trap the search for interspecies Feshbach resonances began. Feshbach resonances are most easily detected through an enhancement of trap loss [13]. This is due to the divergence of the scattering length at a Feshbach resonance and the a^4 scaling of the three-body loss rate [107]. To increase the sensitivity of heteronuclear Feshbach spectroscopy a significant imbalance between the two-species atom numbers is useful [173]. Here the majority species acts as a collisional bath for the minority species which is used as a probe. If the atom number imbalance is large the probe species will be significantly depleted when a resonance is encountered, leaving the majority species largely unchanged. As the lowest internal energy states are used in this experiment trap loss is due to three-body collisions only.

To achieve the atom number imbalance the ^{133}Cs MOT fluorescence servo was used to reduce the number of ^{133}Cs atoms loaded into the magnetic trap. In order to perform sensitive Feshbach spectroscopy a high atomic density for both species is essential as interspecies collisions govern the loss rates from the trap. To produce such a mixture of ^{87}Rb and ^{133}Cs the procedure detailed in section 6.6 was followed up to the first ramp of the dipole trap beam powers to 120 mW in 1.0 s. After this ramp the peak densities are $1.6(1)\times10^{12}$ cm^{-3} and $3.1(4)\times10^{11}$ cm^{-3} for ^{87}Rb and ^{133}Cs respectively. The mixture contains $3.0(3)\times10^{5}$ ^{87}Rb atoms, and $2.6(4)\times10^{4}$ ^{133}Cs atoms at 0.32(1) μK. This temperature is well below the p-wave threshold ($k_{\mathrm{B}}\times$ 56 μK based upon the published C_6 coefficient [102]), simplifying the interpretation of the Feshbach spectrum. For each experimental cycle the ultracold mixture is allowed to evolve at a specific homogeneous magnetic field for 5 s, and then the ^{133}Cs atom number is measured. In figure 6.9 the detection of a Feshbach resonance near 180 G is presented, each data point corresponds to an average of 3-5 measurements.

By fitting a Lorentzian function to the data shown in Fig. 6.9 the position of the Feshbach resonance was measured to be $B_0 = 181.7(5)$ G. This result is in excellent agreement with the previous measurement of this resonance

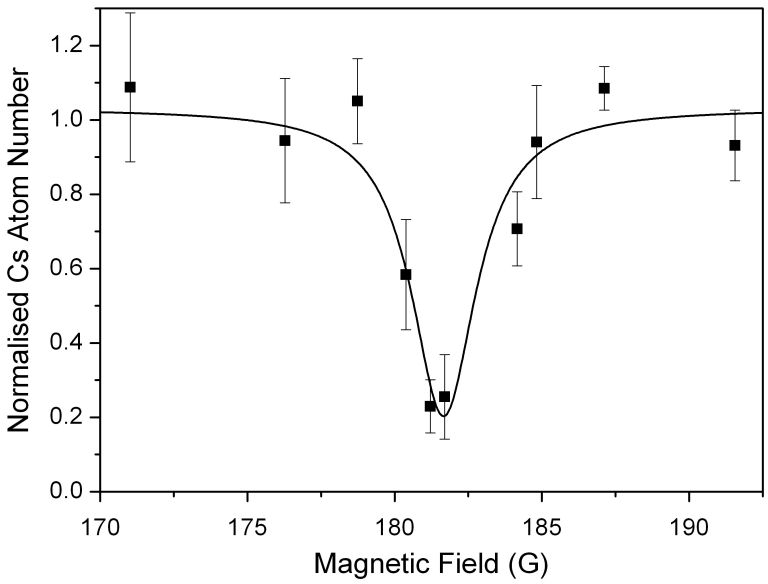

Figure 6.9: Observation of an interspecies ^{87}Rb^{133}Cs Feshbach resonance using loss spectroscopy. The $|1,+1\rangle$ and $|3,+3\rangle$ states were used for ^{87}Rb and ^{133}Cs respectively. The ^{133}Cs (minority species) atom number after a 5 s hold is normalised to the corresponding mean number recorded off resonance. A Lorentzian fit is applied to the data to yield a resonance position of $B_0 = 181.7(5)$ G and a width ≈ 3 G.

[88]. Using this setup we are currently extending the interspecies Feshbach resonance search up to bias fields in excess of 1150 G, and to ^{85}Rb and ^{133}Cs mixtures. Locating an interspecies Feshbach resonance now opens the possibility of creating RbCs molecules via magneto-association.

Chapter 7

Conclusions and Outlook

The work detailed in this thesis has yielded two key experimental results: the realisation of a new route to ^{133}Cs BEC by exploiting the efficient sympathetic cooling of ^{133}Cs via elastic collisions with ^{87}Rb; and the formation of a dual-species degenerate mixture of ^{87}Rb and ^{133}Cs in the same trapping potential. Significant results towards these achievements are drawn together in section 7.1 while an outlook towards future work on this project is discussed in section 7.2.

7.1 Summary

In the course of this work numerous upgrades have been made to the original ^{87}Rb - ^{133}Cs apparatus [93, 94]. The most significant of these is the replacement of the 'baseball' magnetic trap with the combined optical and magnetic hybrid trap. This versatile and simple trapping potential is operated either as a single beam trap or as a levitated crossed dipole trap. Both potentials are easily loaded from a magnetic quadrupole trap and depend critically on the alignment each dipole beam with respect to the magnetic field zero. This style of trap could be readily implemented into many existing experimental setups that have Helmholtz and anti-Helmholtz coils already in position.

Initial work focussed on ^{87}Rb alone in the single beam hybrid trap. Efficient evaporation in the magnetic quadrupole trap enabled $4.9(1) \times 10^6$ atoms to be loaded into the hybrid trap at 9.2(1) μK. Further evaporation produced

pure condensates in the $|1,-1\rangle$ state containing $9.1(2) \times 10^5$ atoms. This result marked the first BEC produced in our group at Durham University. Subsequent experiments soon moved into the crossed dipole trap which can confine high field seeking states and enables the magnetic field to become a free parameter. Both of these features are crucial for the efficient evaporation to BEC of ^{133}Cs which has only been condensed in the $|3,+3\rangle$ state between $21-25$ G. Two novel experiments involving the sympathetic cooling of different spin states in ^{87}Rb, and the production of a three-species spinor BEC, both tested our understanding of how to manipulate the crossed dipole trap.

The efficient sympathetic cooling of ^{133}Cs via ^{87}Rb in the quadrupole trap allowed $1.6(1) \times 10^6$ ^{87}Rb atoms and $5.1(2) \times 10^5$ ^{133}Cs atoms to be loaded into the levitated crossed dipole trap at 12.9(5) μK. Measurements of strong interspecies three body losses observed from this trap permitted an upper limit of $\sim 10^{-25}-10^{-26}$ cm^6/s to be placed on the interspecies three body loss rate coefficient. By sacrificing all of the ^{87}Rb during the sympathetic cooling in the magnetic trap up to $\sim 50\%$ of the ^{133}Cs atoms can be transferred to the levitated crossed dipole trap. Direct evaporation of ^{133}Cs alone then leads to the production of ^{133}Cs condensates containing $6.2(1) \times 10^4$ atoms. This result marks the discovery of a new route to ^{133}Cs BEC free of complexities such as degenerate Raman sideband cooling and multiple dipole traps [12].

By reducing the initial number of ^{133}Cs atoms and decreasing the evaporation time it is possible to produce dual-species condensates of ^{87}Rb and ^{133}Cs in the same trapping potential. The two condensates each contain up to 2×10^4 atoms and exhibit a striking phase separation revealing the mixture to be immiscible. The immiscible mixture always forms one of three structures correlated with the number of atoms present in each condensate. We believe this immiscibility aids the formation of the dual-species condensate by suppressing the interspecies inelastic losses as the mixture condenses. In the future we plan to explore the miscibility by Feshbach tuning both a_{Cs} and a_{RbCs} to test this assertion. Crucially, thermal clouds very close to degeneracy remain miscible, enabling the efficient magneto-association of RbCs molecules. With this in mind an interspecies Feshbach resonance has been observed at 181.7(5) G and Cs_2 dimers have been created using a ^{133}Cs Feshbach resonance to test experimental protocols.

Throughout this work our observations are consistent with the current best estimate of the interspecies scattering length $a_{\mathrm{RbCs}} \approx 650\ a_0$ [90, 92]. These observations include short interspecies rethermalisation times, enhanced loading of ^{133}Cs into the crossed dipole trap in the presence of ^{87}Rb, strong interspecies three body losses and immiscibility of the degenerate mixture at 22.4 G.

7.2 Outlook

The main goal of this experiment remains to be the production of ground state RbCs molecules via magneto-association followed by optical transfer into the rovibrational ground state. However during the course of this work continued advances in the field have resulted in other new and interesting experiments becoming available to study en route towards our main goal.

7.2.1 Towards a Quantum Gas of Polar RbCs Molecules

The next step towards our long term goal of ultracold polar RbCs molecules is to perform Feshbach association of ^{87}Rb and ^{133}Cs into weakly bound heteronuclear molecules via an interspecies Feshbach resonance. A broad entrance-channel dominated interspecies resonance such as that shown in chapter 6 could be an ideal candidate for Feshbach-association [13, 74]. Exploration of the bound molecular state spectrum close to threshold [110] is crucial and will allow the identification of a molecular state suitable for optical transfer to the rovibrational ground state. Suitable molecular states will need to have a good Franck-Condon overlap with both the intermediate excited state and the target molecular state used in the STIRAP process [75].

The STIRAP laser system is currently under development and will follow the transfer scheme highlighted in figure 7.1 and first proposed in [175]. The optical excitation of the Feshbach molecule is at a wavelength of ~ 1570 nm. The wavelength of the second photon is then selected to remove the 3811.5755(16) cm^{-1} of binding energy [176] of the rovibrational molecular ground state.

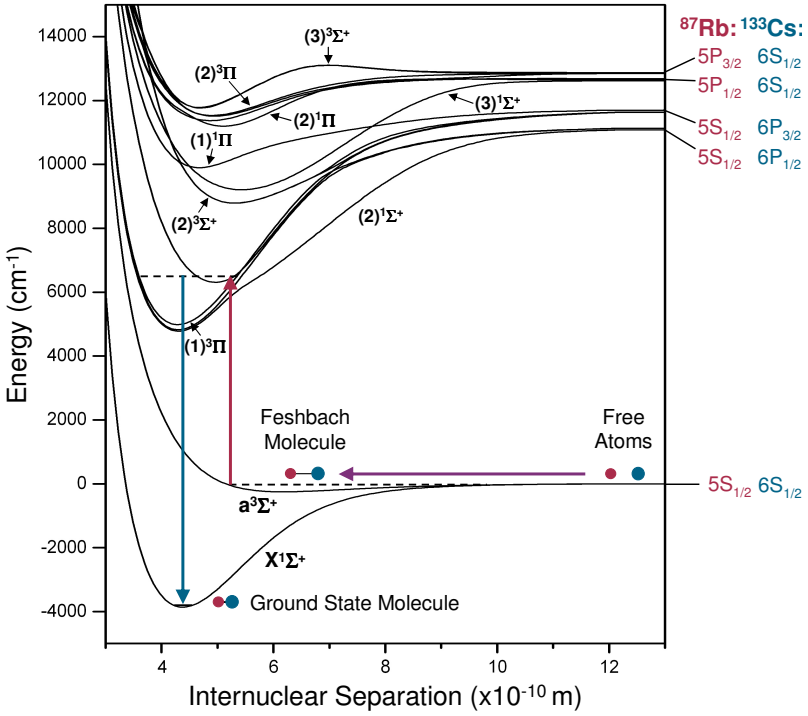

Figure 7.1: Scheme for the production of heteronuclear RbCs molecules in the lowest rovibrational level of the ground state. Highly excited Feshbach molecules are produced from an ultracold mixture of atomic ^{87}Rb and ^{133}Cs via a sweep of the magnetic field (purple arrow). The molecules are then coherently transferred into the vibrational and rotational ground state via a stimulated Raman transition. Here two laser frequencies (red and blue lines) couple the initial and final molecular states via an intermediate excited state. The RbCs molecular potentials plotted are taken from *ab initio* calculations by Allouche *et al.* [174].

Very recently the Innsbruck group have published exciting results on the high resolution spectroscopy of 4000 RbCs Feshbach molecules. These data reveal the location of the rovibrational ground state and quote the required laser frequencies as 6364.0439 cm^{-1} and 10175.2913 cm^{-1} corresponding to wavelengths of $\simeq$ 1571.33 nm and $\simeq$ 982.77 nm respectively [176]. Knowledge of these transition frequencies will greatly accelerate our progress towards polar RbCs molecules.

In parallel to progress towards ground state RbCs molecules a significant short term goal is to reduce the interspecies three-body losses observed in the

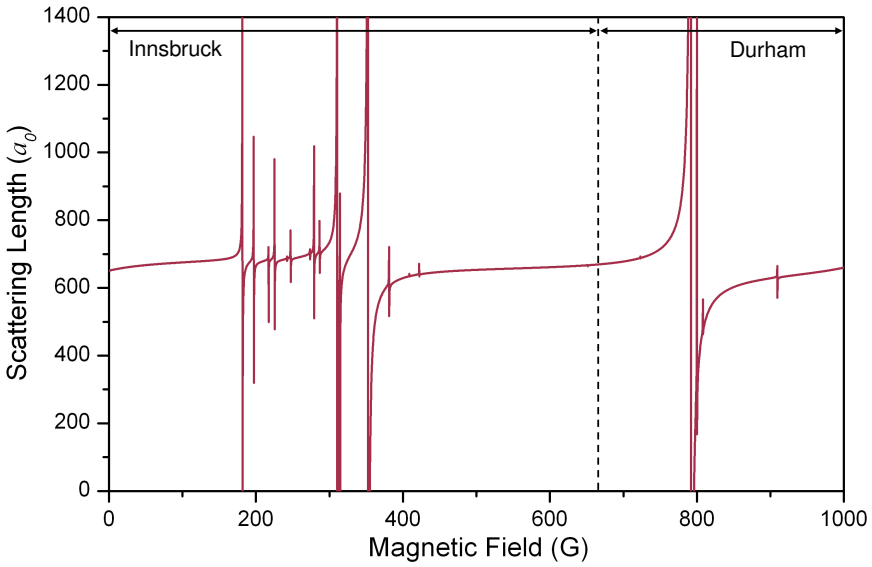

Figure 7.2: The theoretical interspecies s-wave scattering length for a mixture of ^{87}Rb and ^{133}Cs in the $|1, +1\rangle$ and $|3, +3\rangle$ states respectively [177]. These data reveal numerous interspecies Feshbach resonances below 400 G in good agreement with experimental observations [88] which have searched up to fields of 667 G [90, 91]. A broad resonance predicted near 800 G is yet to be observed and is accessible to the Durham experiment.

levitated crossed dipole trap. Such a reduction would increase the efficiency of the evaporative and sympathetic cooling leading to bigger condensates, and ultimately the production of more RbCs Feshbach molecules for optical transfer.

Several options are available to achieve this goal. Firstly coupled channels calculations performed by the group of J. Hutson in Durham have used the observed interspecies Feshbach resonances in a ^{87}Rb - ^{13}Cs mixture [88] to accurately model the interspecies collisional potential [177]. The theoretical behaviour of the interspecies scattering length can then be extrapolated to higher magnetic fields, figure 7.2. These calculations predict a broad interspecies resonance near 800 G that has not been observed and is accessible to the Durham experiment. If the real position of this resonance is closer to 900 G it may coincide near the zero crossing of the ^{133}Cs scattering length at $\simeq$ 890 G, figure 7.4. This coincidence may provide a region where all three scattering lengths (a_{Rb}, a_{Cs}, and a_{RbCs}) are small and positive therefore re-

ducing the interspecies three-body loss rate. By tuning $|a_{\mathrm{RbCs}}| < \sqrt{a_{\mathrm{Rb}} a_{\mathrm{Cs}}}$ the degenerate mixture would also become miscible [34, 36], providing an ideal starting point for efficient magneto-association.

Secondly the waists of the focussed dipole beams could be increased to relax the dipole trap and reduce the initial densities after loading. For example, increasing the beam waists to 80 μm requires the power in each beam to be 10 W to give a trap of the same depth (90 μK for ^{87}Rb). This change reduces ω_{ho} and therefore the density in the trap by $\simeq 25$ % and would result in the trap lifetime due to three-body losses increasing by a factor of ~ 2.

Finally a two colour dipole trap could be implemented to spatially separate the two species [90, 178]. Useful wavelengths for this technique include 532 nm which produces a potential barrier for both species and 880 nm which produces an attractive potential for ^{87}Rb and leaves the ^{133}Cs potential unchanged as here $\alpha_{\mathrm{Cs}} \simeq 0$. At 820 nm the polarisabilities of both species are equal and opposite giving rise to a potential well for ^{87}Rb and a barrier for ^{133}Cs with equal heights [179].

7.2.2 A Mixture of ^{85}Rb and ^{133}Cs

As discussed in chapter 3 the Rb optical setup has been designed to switch between the ^{87}Rb and ^{85}Rb isotopes allowing mixtures of ^{85}Rb and ^{133}Cs to be investigated using this apparatus. Such a mixture consisting of two 'difficult' species with low single species elastic to inelastic collision ratios may prove to be challenging to work with. However theoretical calculations indicate that there is potentially some interesting physics in this mixture to investigate. Coupled channels calculations have been performed for this mixture by the group of J. Hutson. Using a preliminary version of the interspecies collisional potential they have investigated the interspecies s-wave scattering length as a function of magnetic field up to 1000 G [177]. The results of this theoretical work are presented in figure 7.3 for the $|2, +2\rangle$ and $|3, +3\rangle$ states in ^{85}Rb and ^{133}Cs respectively. These data predict several interspecies Feshbach resonances in this magnetic field range and a near zero interspecies background scattering length. Preliminary work is now underway to experimentally locate these interspecies Feshbach resonances. This will test the

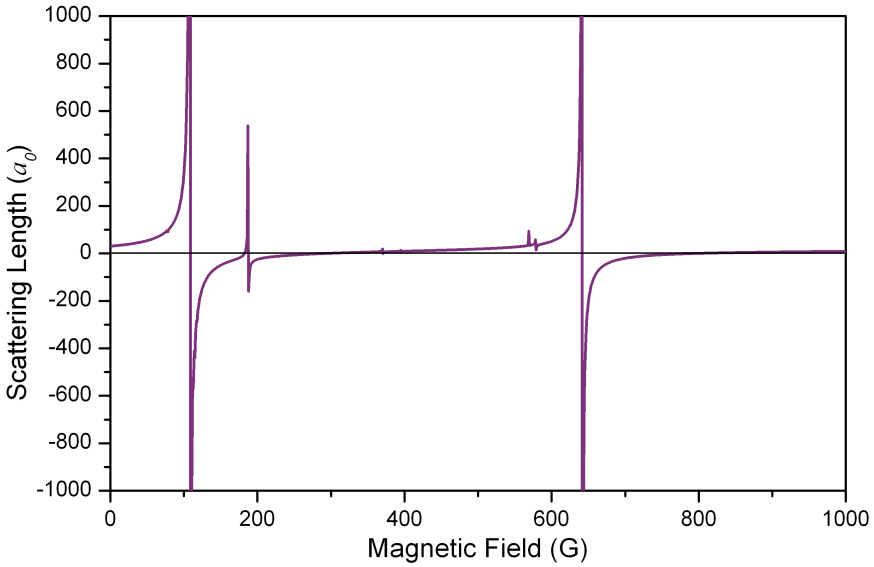

Figure 7.3: The theoretical interspecies s-wave scattering length for a mixture of ^{85}Rb and ^{133}Cs in the $|2,+2\rangle$ and $|3,+3\rangle$ states respectively [177]. These data reveal interspecies Feshbach resonances at 109 G, 188 G and 641 G and a near zero interspecies background scattering length.

theoretical model and allow the collisional potential used to be refined. The results of our standard method in this mixture, by sympathetically cooling ^{133}Cs using ^{85}Rb, will be very interesting. One would expect the sympathetic cooling to initially be effective due to interspecies p- and d-wave elastic collisions in the mixture. However as the mixture temperature decreases these higher partial waves become energetically forbidden. At this point further sympathetic cooling may not be effective due to the small interspecies s-wave scattering length.

7.2.3 ^{133}Cs BEC at High Bias Fields

As shown in this thesis the ^{133}Cs s-wave scattering length is a critical parameter that dictates the single species collisional behaviour at ultracold temperatures. In order for evaporative or sympathetic cooling to be effective and result in the formation of stable condensates a_{Cs} must be $< 400a_0$ and positive. The ^{133}Cs s-wave scattering length for the $|3,+3\rangle$ state is plotted in figure 7.4 for magnetic fields up to 1000 G. This plot shows two windows

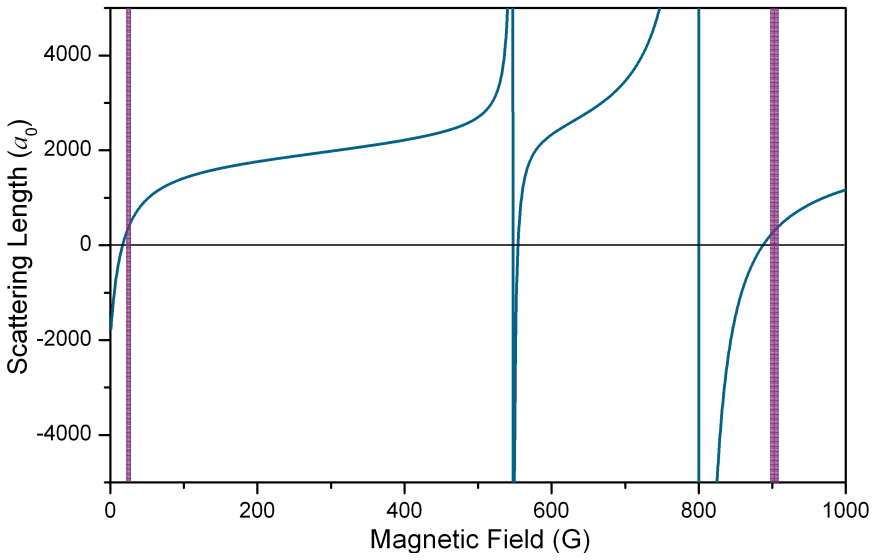

Figure 7.4: The s-wave scattering length for ^{133}Cs in the $|3, +3\rangle$ state. This plot shows two narrow windows (purple lines) where ^{133}Cs can be efficiently evaporated to BEC at $\sim 21 - 25$ G and $\sim 900 - 910$ G. The data shown in this figure are taken from reference [82].

where ^{133}Cs can be efficiently evaporated to BEC. The first window is the well explored region between $\sim 21 - 25$ G that has been used to produce every ^{133}Cs BEC made to date [12, 83]. This region in magnetic field corresponds to a_{Cs} values in the range $\sim 200 - 400a_0$. A second magnetic field window of $\sim 900-910$ G also gives rise to this range of scattering lengths and may be used in future experiments to provide a new gateway into the world of ^{133}Cs BEC. As discussed in section 7.2.1 the zero crossing at $\simeq 890$ G may coincide with an interspecies Feshbach resonance offering prospects of a highly tunable mixture and a magnetic field region where all three scattering lengths are small. Other work with ^{133}Cs in this field range has focussed on the field dependance of three body losses due to Efimov resonances [176].

7.2.4 Concluding Remarks

Within the Durham ^{87}Rb - ^{133}Cs experiment there are two main directions of research available. The first involves experiments with the two-species condensate itself and the second is towards a high phase-space density sample

of ground state RbCs molecules.

The dual species ^{87}Rb - ^{133}Cs BEC allows access to rich physics inaccessible to single species experiments. The phase separation observed between the degenerate species is a dramatic example and may allow access to highly sensitive force measurements in future experiments [180]. By introducing an optical lattice to the mixture [181] a myriad of quantum phases for the two atomic species become available to study [39, 40]. These go far beyond the seminal observations of the superfluid to Mott insulator transition [22].

By combining a three dimensional optical lattice with the degenerate ^{87}Rb - ^{133}Cs mixture a Mott insulator phase transition can give exactly one atom of each species per lattice site provided that the mixture is miscible [182]. For an immiscible mixture the same phase transition gives homonuclear atom pairs at each lattice site. The creation of heteronuclear atom pairs will avoid the strong interspecies three-body losses and provide an ideal starting point for the efficient magneto-association of RbCs Feshbach molecules. Optical transfer via STIRAP into the rovibrational ground state will then produce a dipolar Mott insulator state of one ground state RbCs molecule per lattice site. This method has already been demonstrated for Cs_2 molecules [73]. Dipolar molecules in a optical lattice offer many new research directions including simulations of many-body quantum systems [48], quantum simulation [60] and precision metrology [46]. By moving from the dipolar Mott-insulator to the superfluid state a dipolar molecular condensate could be realised [183]. If this approach causes a loss of phase-space density and is unsuccessful direct evaporative cooling [184] could also lead to the production of a quantum degenerate gas of polar molecules - a current 'Holy Grail' in this field [49]. Of the possible bosonic heteronuclear molecules RbCs is currently the prime candidate for which this will be achieved in the near future.

The numerous experimental routes available in the fields of quantum degenerate mixtures and ultracold polar molecules ensure that both directions for this experiment have bright and exciting futures.

Appendix A

Atomic Properties

Relevant properties of ^{87}Rb and ^{133}Cs are given below. All data specific to an atomic transition are given for the D_2 line in both species.

Quantity	Symbol	^{87}Rb	^{133}Cs
Atomic Number	A	87	133
Mass	m	1.44×10^{-25} kg	2.21×10^{-25} kg
Nuclear Spin	I	3/2	7/2
Vapour Pressure at 25°C	P_v	3.92×10^{-7} Torr	1.49×10^{-6} Torr
Wavelength ($S_{1/2} \rightarrow P_{3/2}$)	λ	780.24 nm	852.35 nm
Wavenumber	$k = 2\pi/\lambda$	8.053×10^6 m^{-1}	7.372×10^6 m^{-1}
Natural Linewidth	Γ	$2\pi \times 6.067$ MHz	$2\pi \times 5.234$ MHz
Doppler Width at 25°C	$\Delta f_{\text{Doppler}}$	500 MHz	370 MHz
Saturation Intensity ($\sigma^{\pm}$)	I_{sat}	1.67 mW/cm^2	1.10 mW/cm^2
Recoil Velocity	$v_r = \hbar k/m$	5.88 mm/s	3.52 mm/s
Recoil Temperature	$T_r = mv_r^2/2k_B$	180 nK	99 nK
g_F factor for ground state	g_F	1/2 ($5S_{1/2},\ F = 2$)	1/4 ($6S_{1/2},\ F = 4$)
g_F factor for excited state	g_F	2/3 ($5P_{3/2},\ F = 3$)	2/5 ($6S_{3/2},\ F = 5$)
Background Scattering Length	a_{bg}	$110a_0$	$2400a_0$
Interaction Parameter	$g = 4\pi\hbar^2 a/m$	5.64×10^{-51} m/kg	8.04×10^{-50} m/kg
Collision Cross-section (ultracold limit)	$8\pi a^2$	8.51×10^{-16} m^2	4.05×10^{-13} m^2

Appendix B

Atom Number Calculations

The properties of trapped atom clouds at various stages of the experiment can be probed either by fluorescence detection or by absorption imaging. These two methods are discussed in detail in section 3.9. Section B.1 presents how to calculate the atom number from the measured fluorescence voltage and section B.2 discusses how to extract the properties of an atomic cloud probed using absorption imaging.

B.1 Fluorescence Detection

The total fluorescence power emitted by N atoms illuminated by light with intensity I is given by

$$P_{\text{total}} = N\frac{hc}{\lambda}\Gamma_{\text{scat}}, \tag{B.1}$$

where

$$\Gamma_{\text{scat}} = \Gamma\frac{\frac{1}{2}C_1\left(\frac{I}{I_{\text{sat}}}\right)}{1 + C_2\left(\frac{I}{I_{\text{sat}}}\right) + 4\left(\frac{2\pi\delta}{\Gamma}\right)^2}. \tag{B.2}$$

with Γ the natural decay rate of the excited state and δ being the laser detuning from resonance. Here C_1 and C_2 are empirical coefficients determined by Townsend *et al.* for ^{133}Cs [185] with $C_1^2 = 0.7(1)$ and $C_2^2 = 0.73(1)$. The intensity I is the total laser intensity *i.e.* 6 times that of a single MOT beam and the saturation intensity I_{sat} is defined as

$$I_{\text{sat}} = \frac{I}{2}\left(\frac{\Gamma}{\Omega_{\text{Rabi}}}\right)^2 = \frac{\pi hc\Gamma}{3\lambda^3}. \tag{B.3}$$

Of the total power emitted a fraction $P_{\rm det}$ is measured given by

$$P_{\rm det} = \frac{\pi d^2/4}{4\pi s^2} P_{\rm total} = \frac{d^2}{16 s^2} P_{\rm total}, \tag{B.4}$$

where d is the diameter of the collecting lens at a distance s from the atoms. The power detected then results in a photodiode current and a voltage across a load resistance R of

$$V_{\rm sig} = I_{\rm p.d.} R = \mathcal{R}(\lambda) P_{\rm det} R \tag{B.5}$$

where $\mathcal{R}(\lambda)$ is the detector responsivity. The number of atoms in the MOT can then be written as a function of the measured voltage

$$N = \frac{1}{\Gamma_{\rm scat}} \frac{V_{\rm sig}}{\mathcal{R}(\lambda) R} \frac{16 s^2}{d^2} \frac{\lambda}{hc}. \tag{B.6}$$

The Townsend coefficients in equation B.2 correct for atoms in the MOT being in an unknown distribution of magnetic sublevels which makes the correct choice of the saturation intensity, $I_{\rm sat}$, difficult. The two extreme possibilities are $I_{\rm sat-closed}$ for the closed stretched transition and $I_{\rm sat-isotropic}$ for an equal distribution over all states. When these saturation intensities are implemented (with $C_1 = C_2 = 1$) the calculated atom numbers differ by a factor of ~ 2. The Townsend result lies between these two extreme cases. The error in N calculated from fluorescence detection can be estimated to be the Townsend value with the two extreme calculations as upper and lower limits. These errors will dominate any other uncertainties provided that the MOT beam intensities have been carefully balanced and measured.

B.2 Absorption Imaging

The number of photons absorbed per second from an incident probe beam of intensity I by an atom is described by equation B.2 with $C_1 = C_2 = 1$. For absorption imaging the probe intensity is typically set at $I \simeq 0.1 I_{\rm sat}$ to ensure that fluctuations in the probe beam intensity do not have a large effect on the measured peak absorption. This allows equation B.2 to be approximated as

$$\Gamma_{\rm scat} = \frac{\Gamma}{2} \frac{I}{I_{\rm sat}} = \frac{3\lambda^3 I}{2\pi hc}. \tag{B.7}$$

The probe intensity after transmission through a layer of atoms of thickness δy with number density n is $I_{\text{new}} = I - \delta I$, where

$$\delta I = n\delta y \Gamma_{\text{scat}} \frac{hc}{\lambda} = \frac{3\lambda^2}{2\pi} nI\delta y. \tag{B.8}$$

For a Gaussian number density distribution, rearranging equation B.8 gives

$$\frac{\delta I}{I} = \frac{3\lambda^2}{2\pi} n_{\text{pk}} \text{exp}\left[\frac{-m}{2k_{\text{B}}T}(\omega_x^2 x^2 + \omega_y^2 y^2 + \omega_z^2 z^2)\right]\delta y. \tag{B.9}$$

Taking the limit of $\delta y \to 0$ ($\delta I \to 0$) and summing over the total thickness of the Gaussian cloud gives

$$\int_{I(x,z)}^{I_{\text{new}}(x,z)} \frac{1}{I}\text{d}I = \frac{3\lambda^2}{2\pi} n_{\text{pk}} \text{exp}\left[\frac{-m}{2k_{\text{B}}T}(\omega_x^2 x^2 + \omega_z^2 z^2)\right] \int_{-\infty}^{\infty} \text{exp}\left[\frac{-m}{2k_{\text{B}}T}\omega_y^2 y^2\right]\text{d}y, \tag{B.10}$$

$$\Rightarrow -\ln\left(\frac{I(x,z)}{I_{\text{new}}(x,z)}\right) = \frac{3\lambda^2 n_{\text{pk}}}{\omega_y}\sqrt{\frac{k_{\text{B}}T}{2\pi m}} \text{exp}\left[\frac{-m}{2k_{\text{B}}T}(\omega_x^2 x^2 + \omega_z^2 z^2)\right]. \tag{B.11}$$

Here $I(x,z)$ and $I_{\text{new}}(x,z)$ are the intensity profiles of the incident and transmitted probe beams respectively. Using equations 3.9 and B.11 the optical depth distribution can be expressed as

$$\text{OD}(x,z) = \frac{3\lambda^2 n_{\text{pk}}}{\omega_y}\sqrt{\frac{k_{\text{B}}T}{2\pi m}} \text{exp}\left[\frac{-m}{2k_{\text{B}}T}(\omega_x^2 x^2 + \omega_z^2 z^2)\right]. \tag{B.12}$$

The peak optical depth, OD_{pk}, occurs at the centre of the cloud ($x = z = 0$), this simplifies equation B.12 to

$$\text{OD}_{\text{pk}} = \frac{3\lambda^2 n_{\text{pk}}}{\omega_y}\sqrt{\frac{k_{\text{B}}T}{2\pi m}}. \tag{B.13}$$

The widths of the number density distribution along the x and z axes of the image plane are exactly equal to the fitted widths of the optical depth distribution.

By substituting equation 3.11 for n_{pk} into equation B.13 gives

$$\text{OD}_{\text{pk}} = \frac{3\lambda^2 N}{4\pi^2}\frac{m\omega_x\omega_z}{k_{\text{B}}T}, \tag{B.14}$$

and by substituting for ω_x and ω_z using equation 3.12 this becomes

$$\text{OD}_{\text{pk}} = \frac{3\lambda^2 N}{4\pi^2}\frac{1}{\sigma_x\sigma_z}. \tag{B.15}$$

By rearranging this equation to express the total number of atoms N equation 3.10 is acquired which allows the atom number to be determined from the clouds widths and optical depth

$$N = \frac{4\pi^2 \mathrm{OD}_{\mathrm{pk}} \sigma_{\mathrm{x}} \sigma_{\mathrm{z}}}{3\lambda^2}. \tag{B.16}$$

Appendix C

Coil Parameters

For simplicitiy the magnetic coils in the assembly were approximated by 'equivalent coils'. Each coil of N turns carrying a current I was replaced with a single turn of infinitesimal thickness carrying a current $I' = N \times I$. The equivalent coil separations and radii were calculated by matching the theoretical first and third spatial field derivatives to the measured values from the real coils. A comparison between the calculated and measured fields revealed a normalised RMS deviation of ~ 1 %, confirming the validity of this approximation. The measured magnetic coil parameters and corresponding 'equivalent coil' dimensions are presented in table C.1.

	Bias 1	Bias 2	Bias 3	Quad 1	Quad 2
Number of turns	2 × 2	6 × 2	2 × 1	3 × 3	2 × 2
Tubing size (mm)	3.5	4.0	4.0	3.5	3.5
Inner diameter (mm)	72.0(1)	96.0(1)	155.6(1)	44.0(1)	103.9(1)
Outer diameter (mm)	85.0(1)	144.0(1)	173.6(1)	65.0(1)	118.0(1)
Inner separation (mm)	32.5(1)	50.0(1)	62.0(1)	37.0(1)	88.8(1)
Outer separation (mm)	46.5(1)	66.0(1)	70.0(1)	58.0(1)	102.8(1)
Resistance of pair (mΩ)	7.56(1)	18.8(1)	5.5(1)	10.5(1)	9.9(1)
Bias Field (G/A)	0.913(2)	1.848(3)	0.261(2)	-	-
Field Curvature ($G/cm^2/A$)	0.003(1)	0.0011(6)	0.0032(2)	-	-
Field Gradient (G/cm/A)	-	-	-	1.001(7)	0.106(9)
Third Derivative ($G/cm^3/A$)	-	-	-	0.005(8)	0.003(2)
Equivalent coil radius (mm)	39.1(1)	58.6(1)	76.3(4)	26.9(1)	58(2)
Equivalent coil separation (mm)	39.6(1)	58.3(1)	62.7(5)	46.7(2)	91(5)

Table C.1: Measured parameters of the real magnetic coils and dimensions of the corresponding 'equivalent coils'. All coils are wound from square cross-section copper tubing. The 3.5 mm^2 (4.0 mm^2) tubing contains a circular hole with a 2 mm (2.75 mm) diameter.

Appendix D

Electronics

The servo circuit used to control and stabilise power in each dipole trap beam is shown in figure D.1.

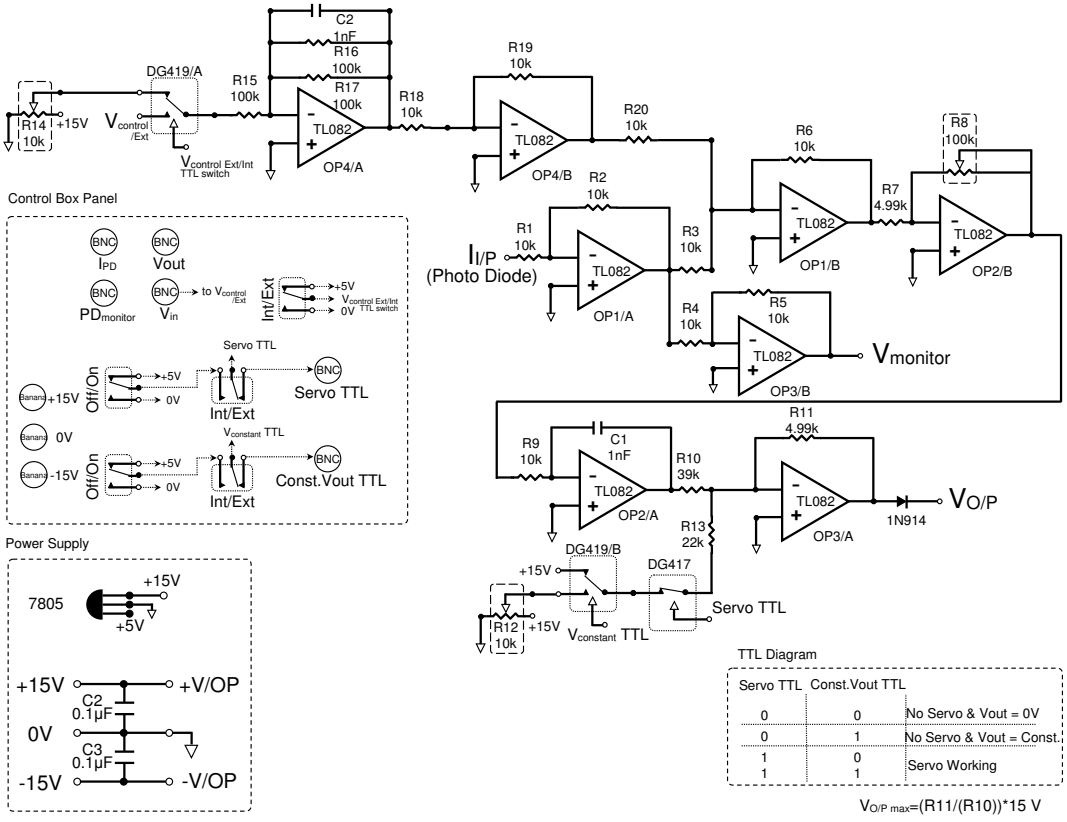

Figure D.1: Electronics circuit used to servomechanically control each dipole trap beam.

The servo circuit used to tune and stabilise the ^{133}Cs atom number loaded into the science MOT is shown in figure D.2.

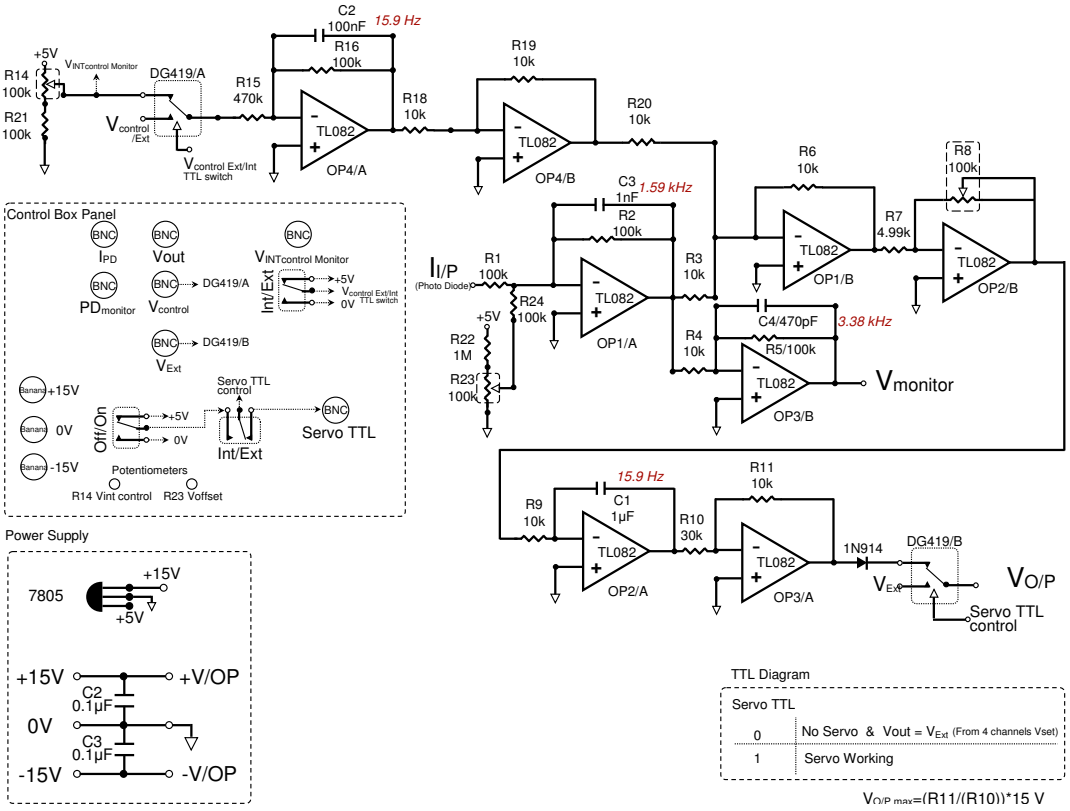

Figure D.2: Electronics circuit used to servomechanically control the number of atoms loaded into the ^{133}Cs science MOT.

Bibliography

[1] H. J. Metcalf and P. van der Straten, *Laser Cooling and Trapping* (Springer, 1999).

[2] K. B. Davis, M.-O. Mewes, M. A. Joffe, M. R. Andrews, and W. Ketterle, *Evaporative Cooling of Sodium Atoms*, Phys. Rev. Lett. **74**, 5202 (1995).

[3] M. H. Anderson, J. R. Ensher, M. R. Matthews, C. E. Wiemann, and E. A. Cornell, *Observation of Bose-Einstein Condensation in a Dilute Atomic Vapour*, Science **269**, 198 (1995).

[4] K. B. Davis *et al.*, *Bose-Einstein Condensation in a Gas of Sodium Atoms*, Phys. Rev. Lett. **75**, 3969 (1995).

[5] C. C. Bradley, C. A. Sackett, J. J. Tollett, and R. G. Hulet, *Evidence of Bose-Einstein Condensation in an Atomic Gas with Attractive Interactions*, Phys. Rev. Lett. **75**, 1687 (1995).

[6] S. Chu, *Nobel Lecture: The manipulation of neutral particles*, Rev. Mod. Phys. **70**, 685 (1998).

[7] C. N. Cohen-Tannoudji, *Nobel Lecture: Manipulating atoms with photons*, Rev. Mod. Phys. **70**, 707 (1998).

[8] W. D. Phillips, *Nobel Lecture: Laser cooling and trapping of neutral atoms*, Rev. Mod. Phys. **70**, 721 (1998).

[9] E. A. Cornell and C. E. Wieman, *Nobel Lecture: Bose-Einstein condensation in a dilute gas, the first 70 years and some recent experiments*, Rev. Mod. Phys. **74**, 875 (2002).

[10] W. Ketterle, *Nobel lecture: When atoms behave as waves: Bose-Einstein condensation and the atom laser*, Rev. Mod. Phys. **74**, 1131 (2002).

[11] S. L. Cornish, N. R. Claussen, J. L. Roberts, E. A. Cornell, and C. E. Wieman, *Stable ^{85}Rb Bose-Einstein Condensates with Widely Tunable Interactions*, Phys. Rev. Lett. **85**, 1795 (2000).

[12] T. Weber, J. Herbig, M. Mark, H.-C. Nägerl, and R. Grimm, *Bose-Einstein Condensation of Cesium*, Science **299**, 232 (2003).

[13] C. Chin, R. Grimm, P. Julienne, and E. Tiesinga, *Feshbach resonances in ultracold gases*, Rev. Mod. Phys. **82**, 1225 (2010).

[14] M. R. Andrews *et al.*, *Observation of Interference Between Two Bose Condensates*, Science **275**, 637 (1997).

[15] M.-O. Mewes *et al.*, *Output Coupler for Bose-Einstein Condensed Atoms*, Phys. Rev. Lett. **78**, 582 (1997).

[16] I. Bloch, T. W. Hänsch, and T. Esslinger, *Atom Laser with a cw Output Coupler*, Phys. Rev. Lett. **82**, 3008 (1999).

[17] M. R. Matthews *et al.*, *Vortices in a Bose-Einstein Condensate*, Phys. Rev. Lett. **83**, 2498 (1999).

[18] K. W. Madison, F. Chevy, W. Wohlleben, and J. Dalibard, *Vortex Formation in a Stirred Bose-Einstein Condensate*, Phys. Rev. Lett. **84**, 806 (2000).

[19] K. E. Strecker, G. B. Partridge, A. G. Truscott, and R. G. Hulet, *Formation and propagation of matter-wave soliton trains*, Nature **417**, 150 (2002).

[20] S. L. Cornish, S. T. Thompson, and C. E. Wieman, *Formation of Bright Matter-Wave Solitons during the Collapse of Attractive Bose-Einstein Condensates*, Phys. Rev. Lett. **96**, 170401 (2006).

[21] I. Bloch, J. Dalibard, and W. Zwerger, *Many-body physics with ultracold gases*, Rev. Mod. Phys. **80**, 885 (2008).

[22] M. Greiner, O. Mandel, T. Esslinger, T. W. Hänsch, and I. Bloch, *Quantum phase transition from a superfluid to a Mott insulator in a gas of ultracold atoms*, Nature **415**, 39 (2002).

[23] M. Greiner, C. A. Regal, and D. S. Jin, *Emergence of a molecular Bose-Einstein condensate from a Fermi gas*, Nature **426**, 537 (2003).

[24] S. Jochim *et al.*, *Bose-Einstein Condensation of Molecules*, Science **302**, 2101 (2003).

[25] M. W. Zwierlein *et al.*, *Observation of Bose-Einstein Condensation of Molecules*, Phys. Rev. Lett. **91**, 250401 (2003).

[26] M. Inguscio, W. Ketterle, and C. Salomon, editors, *Ultacold Fermi Gases*, Proceedings of the International School of Physics "Enrico Fermi", IOS Press, Amsterdam, 2006, course CLXIV, Varenna 2006.

[27] C. J. Myatt, E. A. Burt, R. W. Ghrist, E. A. Cornell, and C. E. Wieman, *Production of Two Overlapping Bose-Einstein Condensates by Sympathetic Cooling*, Phys. Rev. Lett. **78**, 586 (1997).

[28] J. Stenger *et al.*, *Spin domains in ground state spinor Bose-Einstein condensates*, Nature **396**, 345 (1998).

[29] A. G. Truscott, K. E. Strecker, W. I. McAlexander, G. B. Partridge, and R. G. Hulet, *Observation of Fermi Pressure in a Gas of Trapped Atoms*, Science **291**, 2570 (2001).

[30] Z. Hadzibabic *et al.*, *Two-Species Mixture of Quantum Degenerate Bose and Fermi Gases*, Phys. Rev. Lett. **88**, 160401 (2002).

[31] G. Roati, F. Riboli, G. Modugno, and M. Inguscio, *Fermi-Bose Quantum Degenerate* $^{40}K - ^{87}$ *Rb Mixture with Attractive Interaction*, Phys. Rev. Lett. **89**, 150403 (2002).

[32] G. Modugno, M. Modugno, F. Riboli, G. Roati, and M. Inguscio, *Two Atomic Species Superfluid*, Phys. Rev. Lett. **89**, 190404 (2002).

[33] C. Silber *et al.*, *Quantum-Degenerate Mixture of Fermionic Lithium and Bosonic Rubidium Gases*, Phys. Rev. Lett. **95**, 170408 (2005).

[34] M. Zaccanti *et al.*, *Control of the interaction in a Fermi-Bose mixture*, Phys. Rev. A **74**, 041605 (2006).

[35] S. Ospelkaus, C. Ospelkaus, L. Humbert, K. Sengstock, and K. Bongs, *Tuning of Heteronuclear Interactions in a Degenerate Fermi-Bose Mixture*, Phys. Rev. Lett. **97**, 120403 (2006).

[36] S. B. Papp, J. M. Pino, and C. E. Wieman, *Tunable Miscibility in a Dual-Species Bose-Einstein Condensate*, Phys. Rev. Lett. **101**, 040402 (2008).

[37] M. Taglieber, A.-C. Voigt, T. Aoki, T. W. Hänsch, and K. Dieckmann, *Quantum Degenerate Two-Species Fermi-Fermi Mixture Coexisting with a Bose-Einstein Condensate*, Phys. Rev. Lett. **100**, 010401 (2008).

[38] M. K. Tey, S. Stellmer, R. Grimm, and F. Schreck, *Double-degenerate Bose-Fermi mixture of strontium*, Phys. Rev. A **82**, 011608 (2010).

[39] E. Altman *et al.*, *Phase diagram of two-component bosons on an optical lattice*, New J. Phys. **5**, 113 (2003).

[40] A. Kuklov, N. Prokof'ev, and B. Svistunov, *Commensurate Two-Component Bosons in an Optical Lattice: Ground State Phase Diagram*, Phys. Rev. Lett. **92**, 050402 (2004).

[41] L. D. Carr, D. DeMille, R. V. Krems, and J. Ye, *Cold and ultracold molecules: science, technology and applications*, New J. Phys. **11**, 055049 (2009).

[42] B. DeMarco and D. S. Jin, *Onset of Fermi degeneracy in a trapped atomic gas*, Science **285**, 1703 (1999).

[43] G. Modugno *et al.*, *Collapse of a Degenerate Fermi Gas*, Science **297**, 2240 (2002).

[44] B. Friedrich and J. M. Doyle, *Why are Cold Molecules so Hot?*, ChemPhysChem **10**, 604 (2009).

[45] O. Dulieu and C. Gabbanini, *The formation and interactions of cold and ultracold molecules: new challenges for interdisciplinary physics*, Rep. Prog. Phys. **72**, 086401 (2009).

[46] T. Zelevinsky, S. Kotochigova, and J. Ye, *Precision Test of Mass-Ratio Variations with Lattice-Confined Ultracold Molecules*, Phys. Rev. Lett. **100**, 043201 (2008).

[47] R. V. Krems, *Cold controlled chemistry*, Phys. Chem. Chem. Phys. **10**, 4079 (2008).

[48] G. Pupillo, A. Micheli, H. P. Büchler, and P. Zoller, *Cold molecules: Theory, experiment, applications* (CRC Press, Boca Raton, 2009), chap. 12.

[49] T. Lahaye *et al.*, *The physics of dipolar bosonic quantum gases*, Rep. Prog. Phys. **72**, 126401 (2009).

[50] M. A. Baranov, *Theoretical progress in many-body physics with ultracold dipolar gases*, Phys. Rep. **464**, 71 (2008).

[51] M. Fattori *et al.*, *Magnetic Dipolar Interaction in a Bose-Einstein Condensate Atomic Interferometer*, Phys. Rev. Lett. **101**, 190405 (2008).

[52] A. Griesmaier *et al.*, *Comparing Contact and Dipolar Interactions in a Bose-Einstein Condensate*, Phys. Rev. Lett. **97**, 250402 (2006).

[53] K.-K. Ni *et al.*, *A High Phase-Space-Density Gas of Polar Molecules*, Science **322**, 231 (2008).

[54] M. Aymar and O. Dulieu, *Calculation of accurate permanent dipole moments of the lowest $^{1,3}\Sigma^+$ states of heteronuclear alkali dimers using extended basis sets*, J. Chem. Phys. **122**, 204302 (2005).

[55] S. Kotochigova and E. Tiesinga, *Ab initio relativistic calculation of the RbCs molecule*, J. Chem. Phys. **123**, 174304 (2005).

[56] S. Kotochigova, P. S. Julienne, and E. Tiesinga, *Ab initio calculation of the KRb dipole moments*, Phys. Rev. A **68**, 022501 (2003).

[57] A. V. Avdeenkov, M. Kajita, and J. L. Bohn, *Suppression of inelastic collisions of polar $^1\Sigma$ state molecules in an electrostatic field*, Phys. Rev. A **73**, 022707 (2006).

[58] B. Capogrosso-Sansone, C. Trefzger, M. Lewenstein, P. Zoller, and G. Pupillo, *Quantum Phases of Cold Polar Molecules in 2D Optical Lattices*, Phys. Rev. Lett. **104**, 125301 (2010).

[59] D. DeMille, *Quantum Computation with Trapped Polar Molecules*, Phys. Rev. Lett. **88**, 067901 (2002).

[60] A. Micheli, G. K. Brennen, and P. Zoller, *A toolbox for lattice-spin models with polar molecules*, Nat. Phys. **2**, 341 (2006).

[61] H. L. Bethlem, G. Berden, and G. Meijer, *Decelerating Neutral Dipolar Molecules*, Phys. Rev. Lett. **83**, 1558 (1999).

[62] J. D. Weinstein, R. deCarvalho, T. Guillet, B. Friedrich, and J. M. Doyle, *Magnetic trapping of calcium monohydride molecules at millikelvin temperatures*, Nature **395**, 148 (1998).

[63] G. Modugno *et al.*, *Bose-Einstein Condensation of Potassium Atoms by Sympathetic Cooling*, Science **294**, 1320 (2001).

[64] B. K. Stuhl, B. C. Sawyer, D. Wang, and J. Ye, *Magneto-optical Trap for Polar Molecules*, Phys. Rev. Lett. **101**, 243002 (2008).

[65] E. S. Shuman, J. F. Barry, and D. DeMille, *Laser cooling of a diatomic molecule*, Nature **467**, 820 (2010).

[66] K. M. Jones, E. Tiesinga, P. D. Lett, and P. S. Julienne, *Ultracold photoassociation spectroscopy: Long-range molecules and atomic scattering*, Rev. Mod. Phys. **78**, 483 (2006).

[67] J. M. Sage, S. Sainis, T. Bergeman, and D. DeMille, *Optical Production of Ultracold Polar Molecules*, Phys. Rev. Lett. **94**, 203001 (2005).

[68] J. Deiglmayr *et al.*, *Formation of Ultracold Polar Molecules in the Rovibrational Ground State*, Phys. Rev. Lett. **101**, 133004 (2008).

[69] M. Viteau *et al.*, *Optical Pumping and Vibrational Cooling of Molecules*, Science **321**, 232 (2008).

[70] F. Lang, K. Winkler, C. Strauss, R. Grimm, and J. H. Denschlag, *Ultracold Triplet Molecules in the Rovibrational Ground State*, Phys. Rev. Lett. **101**, 133005 (2008).

[71] K. Aikawa *et al.*, *Coherent Transfer of Photoassociated Molecules into the Rovibrational Ground State*, Phys. Rev. Lett. **105**, 203001 (2010).

[72] J. G. Danzl *et al.*, *Quantum Gas of Deeply Bound Ground State Molecules*, Science **321**, 1062 (2008).

[73] J. G. Danzl *et al.*, *An ultracold high-density sample of rovibronic ground-state molecules in an optical lattice*, Nature Phys. **6**, 265 (2010).

[74] T. Köhler, K. Góral, and P. S. Julienne, *Production of cold molecules via magnetically tunable Feshbach resonances*, Rev. Mod. Phys. **78**, 1311 (2006).

[75] K. Bergmann, H. Theuer, and B. W. Shore, *Coherent population transfer among quantum states of atoms and molecules*, Rev. Mod. Phys. **70**, 1003 (1998).

[76] A. Marte *et al.*, *Feshbach Resonances in Rubidium 87: Precision Measurement and Analysis*, Phys. Rev. Lett. **89**, 283202 (2002).

[77] C. Chin *et al.*, *Precision Feshbach spectroscopy of ultracold* Cs_2, Phys. Rev. A **70**, 032701 (2004).

[78] P. J. Leo, C. J. Williams, and P. S. Julienne, *Collision Properties of Ultracold* ^{133}Cs *Atoms*, Phys. Rev. Lett. **85**, 2721 (2000).

[79] J. Herbig *et al.*, *Preparation of a Pure Molecular Quantum Gas*, Science **301**, 1510 (2003).

[80] T. Kraemer *et al.*, *Evidence for Efimov quantum states in an ultracold gas of caesium atoms*, Nature **440**, 315 (2006).

[81] M. Gustavsson *et al.*, *Control of Interaction-Induced Dephasing of Bloch Oscillations*, Phys. Rev. Lett. **100**, 080404 (2008).

[82] P. Julienne and co-workers at NIST Gaithersburg, Private Communication (2005).

[83] C.-L. Hung, X. Zhang, N. Gemelke, and C. Chin, *Accelerating evaporative cooling of atoms into Bose-Einstein condensation in optical traps*, Phys. Rev. A **78**, 011604 (2008).

[84] G. Delannoy *et al.*, *Understanding the production of dual Bose-Einstein condensation with sympathetic cooling*, Phys. Rev. A **63**, 051602 (2001).

[85] M. Anderlini *et al.*, *Sympathetic cooling and collisional properties of a* $Rb - Cs$ *mixture*, Phys. Rev. A **71**, 061401 (2005).

[86] M. J. Jamieson *et al.*, *Elastic scattering of cold caesium and rubidium atoms*, J. Phys. B **36**, 1085 (2003).

[87] M. Haas *et al.*, *Species-selective microwave cooling of a mixture of rubidium and caesium atoms*, New J. Phys. **9**, 147 (2007).

[88] K. Pilch *et al.*, *Observation of interspecies Feshbach resonances in an ultracold Rb-Cs mixture*, Phys. Rev. A **79**, 042718 (2009).

[89] P. S. Żuchowski and J. M. Hutson, *Reactions of ultracold alkali-metal dimers*, Phys. Rev. A **81**, 060703 (2010).

[90] A. Lercher *et al.*, *Production of a dual-species Bose-Einstein condensate of Rb and Cs atoms*, Eur. Phys. J. D (2011).

[91] T. Takekoshi *et al.*, in preparation (2011).

[92] J. M. Hutson, Private Communication (2010).

[93] M. L. Harris, *Realisation of a Cold Mixture of Rubidium and Caesium*, PhD thesis, Durham University, 2008.

[94] P. Tierney, *Magnetic Trapping of an Ultracold* ^{87}Rb-^{133}Cs, PhD thesis, Durham University, 2009.

[95] J. Weiner, V. S. Bagnato, S. Zilio, and P. S. Julienne, *Experiments and theory in cold and ultracold collisions*, Rev. Mod. Phys. **71**, 1 (1999).

[96] F. Dalfovo, S. Giorgini, L. P. Pitaevskii, and S. Stringari, *Theory of Bose-Einstein condensation in trapped gases*, Rev. Mod. Phys. **71**, 463 (1999).

[97] C. Pethick and H. Smith, *Bose-Einstein Condensation in Dilute Gases* (Cambridge University Press, 2002).

[98] J. Sakurai, *Modern Quantum Mechanics*, Second edition ed. (Addison Wesley, 1993).

[99] L. S. Butcher, D. N. Stacey, C. J. Foot, and K. Burnett, *Ultracold collisions for Bose-Einstein condensation*, Phil. Trans. R. Soc. Lond. A **357**, 1421 (1999).

[100] C. Chin, *Cooling, Collisions and Coherence of Cold Cesium Atoms in a Trap*, PhD thesis, Stanford University, 2001.

[101] A. Derevianko, W. R. Johnson, M. S. Safronova, and J. F. Babb, *High-Precision Calculations of Dispersion Coefficients, Static Dipole Polarizabilities, and Atom-Wall Interaction Constants for Alkali-Metal Atoms*, Phys. Rev. Lett. **82**, 3589 (1999).

[102] M. Marinescu and H. R. Sadeghpour, *Long-range potentials for two-species alkali-metal atoms*, Phys. Rev. A **59**, 390 (1999).

[103] S. Kotochigova, E. Tiesinga, and P. S. Julienne, *Relativistic ab initio treatment of the second-order spin-orbit splitting of the* $a3\Sigma u+$ *potential of rubidium and cesium dimers*, Phys. Rev. A **63**, 012517 (2000).

[104] D. M. Stamper-Kurn *et al.*, *Reversible Formation of a Bose-Einstein Condensate*, Phys. Rev. Lett. **81**, 2194 (1998).

[105] S. Inouye *et al.*, *Observation of Feshbach resonances in a Bose-Einstein condensate*, Nature **392**, 151 (1998).

[106] A. J. Moerdijk, B. J. Verhaar, and A. Axelsson, *Resonances in ultracold collisions of* $Li6$, $Li7$, *and* $Na23$, Phys. Rev. A **51**, 4852 (1995).

[107] T. Weber, J. Herbig, M. Mark, H.-C. Nägerl, and R. Grimm, *Three-Body Recombination at Large Scattering Lengths in an Ultracold Atomic Gas*, Phys. Rev. Lett. **91**, 123201 (2003).

[108] M. Theis *et al.*, *Tuning the Scattering Length with an Optically Induced Feshbach Resonance*, Phys. Rev. Lett. **93**, 123001 (2004).

[109] F. Ferlaino and R. Grimm, *Forty years of Efimov physics: How a bizarre prediction turned into a hot topic*, Physics **3** (2010).

[110] M. Mark *et al.*, *Spectroscopy of ultracold trapped cesium Feshbach molecules*, Phys. Rev. A **76**, 042514 (2007).

[111] T. Mukaiyama, J. R. Abo-Shaeer, K. Xu, J. K. Chin, and W. Ketterle, *Dissociation and Decay of Ultracold Sodium Molecules*, Phys. Rev. Lett. **92**, 180402 (2004).

[112] G. Thalhammer *et al.*, *Long-Lived Feshbach Molecules in a Three-Dimensional Optical Lattice*, Phys. Rev. Lett. **96**, 050402 (2006).

[113] C. A. Regal, C. Ticknor, J. L. Bohn, and D. S. Jin, *Creation of ultracold molecules from a Fermi gas of atoms*, Nature **424**, 47 (2003).

[114] C. Chin, A. J. Kerman, V. Vuletić, and S. Chu, *Sensitive Detection of Cold Cesium Molecules Formed on Feshbach Resonances*, Phys. Rev. Lett. **90**, 033201 (2003).

[115] S. Bose, *Plankcks Gesetz und Lichtquantenhypothese*, Z. Phys. **26**, 178 (1924).

[116] A. Einstein, *Quantentheorie des einatomigen idealen Gases.*, Sitzungber. Preuss. Akad. Wiss. , 261 (1924).

[117] S. R. de Groot, G. R. Hooyman, and C. A. ten Seldam, *On the Bose-Einstein Condensation*, Proc. R. Soc. Lond. A **203**, 266 (1950).

[118] K. Huang, *Statistical Mechanics*, Second edition ed. (J. Wiley and Sons, New York, 1987).

[119] N. Bogoliubov, *On the Theory of Superfluidity*, J. Phys. **11**, 23 (1947).

[120] E. Gross, *Structure of Quantized Vortex in Boson Systems*, Il Nuovo Cimento **20**, 454 (1961).

[121] L. P. Pitaevskii, *Vortex lines in an imperfect Bose gas*, Sov. Phys. JETP **13**, 451 (1961).

[122] M.-O. Mewes *et al.*, *Bose-Einstein Condensation in a Tightly Confining dc Magnetic Trap*, Phys. Rev. Lett. **77**, 416 (1996).

[123] M. J. Holland, D. S. Jin, M. L. Chiofalo, and J. Cooper, *Emergence of Interaction Effects in Bose-Einstein Condensation*, Phys. Rev. Lett. **78**, 3801 (1997).

[124] T. Kraemer *et al.*, *Optimized production of a cesium Bose-Einstein condensate*, Appl. Phys. B **79**, 1013 (2004).

[125] P. A. Ruprecht, M. J. Holland, K. Burnett, and M. Edwards, *Time-dependent solution of the nonlinear Schrödinger equation for Bose-condensed trapped neutral atoms*, Phys. Rev. A **51**, 4704 (1995).

[126] E. A. Donley *et al.*, *Dynamics of collapsing and exploding Bose-Einstein condensates*, Nature **412**, 295 (2001).

[127] Y. Castin and R. Dum, *Bose-Einstein Condensates in Time Dependent Traps*, Phys. Rev. Lett. **77**, 5315 (1996).

[128] B. D. Esry, C. H. Greene, J. P. Burke, Jr., and J. L. Bohn, *Hartree-Fock Theory for Double Condensates*, Phys. Rev. Lett. **78**, 3594 (1997).

[129] F. Riboli and M. Modugno, *Topology of the ground state of two interacting Bose-Einstein condensates*, Phys. Rev. A **65**, 063614 (2002).

[130] H. J. Metcalf and P. van der Straten, *Laser Cooling and Trapping* (Springer, 2002).

[131] G. K. Woodgate, *Elementary Atomic Structure.* (Oxford University Press, 2002).

[132] W. Petrich, M. H. Anderson, J. R. Ensher, and E. A. Cornell, *Stable, Tightly Confining Magnetic Trap for Evaporative Cooling of Neutral Atoms*, Phys. Rev. Lett. **74**, 3352 (1995).

[133] Y.-J. Lin, A. R. Perry, R. L. Compton, I. B. Spielman, and J. V. Porto, *Rapid production of ^{87}Rb Bose-Einstein condensates in a combined magnetic and optical potential*, Phys. Rev. A **79**, 063631 (2009).

[134] W. Ketterle and N. J. V. Druten, *Evaporative cooling of trapped atoms*, Adv. Atom. Mol. Opt. Phys. **37**, 181 (1996).

[135] R. Grimm, M. Weidermüller, and Y. B. Ovchinnikov, *Optical Dipole Traps for Neutral Atoms*, Adv. Atom. Mol. Opt. Phys **42**, 95 (2000).

[136] K. J. Weatherill, *A CO_2 Laser Lattice Experiment for Cold Atoms*, PhD thesis, Durham University, 2007.

[137] D. J. McCarron, I. G. Hughes, P. Tierney, and S. L. Cornish, *A heated vapor cell unit for dichroic atomic vapor laser lock in atomic rubidium*, Rev. Sci. Inst. **78** (2007).

[138] B. Cherón, H. Gilles, J. Hamel, O. Moreau, and H. Sorel, *Laser Frequency Stabilization using Zeeman Effect*, J. Physique III **4**, 401 (1994).

[139] K. L. Corwin, Z.-T. Lu, C. F. Hand, R. J. Epstein, and C. E. Wieman, *Frequency-Stabilized Diode Laser with the Zeeman Shift in an Atomic Vapor*, Appl. Opt. **37**, 3295 (1998).

[140] M. L. Harris, S. L. Cornish, A. Tripathi, and I. G. Hughes, *Optimization of sub-Doppler DAVLL on the rubidium D2 line*, J. Phys. B **41**, 085401 (2008).

[141] C. Wieman and T. Hänsch, *Doppler-Free Laser Polarization Spectroscopy*, Phys. Rev. Lett. **36**, 11170 (1976).

[142] J. H. Shirley, *Modulation transfer processes in optical heterodyne saturation spectroscopy*, Opt. Lett. **7**, 537 (1982).

[143] D. J. McCarron, S. A. King, and S. L. Cornish, *Modulation transfer spectroscopy in atomic rubidium*, Meas. Sci. Technol. **19**, 105601 (2008).

[144] G. C. Bjorklund, *Frequency-modulation spectroscopy: a new method for measuring weak absorptions and dispersions*, Opt. Lett. **5**, 15 (1980).

[145] D. A. Smith and I. G. Hughes, *The Role of Hyperfine Pumping in Multilevel Systems Exhibiting Saturated Absorption*, Am. J. Phys **72**, 631 (2004).

[146] R. K. Raj, D. Bloch, J. J. Snyder, G. Camy, and M. Ducloy, *High-Frequency Optically Heterodyned Saturation Spectroscopy Via Resonant Degenerate Four-Wave Mixing*, Phys. Rev. Lett. **44**, 1251 (1980).

[147] E. Jaatinen, *Theoretical investigation of maximum signal levels obtainable with modulation transfer spectroscopy*, Optics Communications **120**, 91 (1995).

[148] I. S. Grant and W. R. Phillips, *Electromagnetism*, 2^{nd} ed. (Wiley & Sons).

[149] R. Loudon, *The Quantum Theory of Light, 3^{rd} Edition.* (Oxford University Press, 2004).

[150] G. C. Bjorklund, M. D. Levenson, W. Lenth, and C. Ortiz, *Frequency Modulation (FM) Spectroscopy Theory of Lineshapes and Signal-to-Noise Analysis*, Appl. Phys. B **32**, 145 (1983).

[151] S. Händel *et al.*, *Magnetic merging of ultracold atomic gases of ^{85}Rb and ^{87}Rb*, Phys. Rev. A **83**, 053633 (2011).

[152] J. Arlt, O. Maragò, S. Webster, S. Hopkins, and C. Foot, *A Pyramidal Magneto-Optical Trap as a Source of Slow Atoms*, Opt. Comm. **157**, 303 (1998).

[153] N. Lundblad *et al.*, *Two-species cold atomic beam*, J. Opt. Soc. Am. B **21**, 3 (2004).

[154] M. L. Harris, P. Tierney, and S. L. Cornish, *Magnetic trapping of a cold RbCs atomic mixture*, J. Phys. B **41**, 035303 (2008).

[155] N. Hoang, N. Zahzam, S. Guibal, and P. Pillet, *Collisions in a cesium hybrid optical and magnetic trap*, Eur. Phys. J. D **36**, 95 (2005).

[156] J. Kobayashi, Y. Izumi, M. Kumakura, and Y. Takahashi, *Stable all-optical formation of Bose-Einstein condensate using pointing-stabilized optical trapping beams*, Appl. Phys. B **83**, 21 (2006).

[157] B. Fröhlich *et al.*, *Two-frequency acousto-optic modulator driver to improve the beam pointing stability during intensity ramps*, Rev. Sci. Instrum. **78**, 043101 (2007).

[158] M. S. Safronova, B. Arora, and C. W. Clark, *Frequency-dependent polarizabilities of alkali-metal atoms from ultraviolet through infrared spectral regions*, Phys. Rev. A **73**, 022505 (2006).

[159] M. King, *Process Control: A Practical Approach* (J. Wiley and Sons, New York, 2010).

[160] S. Chu, L. Hollberg, J. E. Bjorkholm, A. Cable, and A. Ashkin, *Three-dimensional viscous confinement and cooling of atoms by resonance radiation pressure*, Phys. Rev. Lett. **55**, 48 (1985).

[161] J. Dalibard and C. Cohen-Tannoudji, *Laser Cooling Below the Doppler Limit by Polarization Gradients: Simple Theoretical Models*, J. Opt. Soc. Am. B **6**, 2023 (1989).

[162] D. J. Wineland and W. M. Itano, *Laser Cooling of Atoms*, Phys. Rev. A **20**, 1527 (1979).

[163] L. Landau and E. Lifschitz, *Mechanik* (Akademie-Verlag, 1964).

[164] D. Guéry-Odelin, J. Söding, P. Desbiolles, and J. Dalibard, *Is Bose-Einstein condensation of atomic cesium possible?*, Europhys. Lett. **44**, 25 (1998).

[165] J. R. Rubbmark, M. M. Kash, M. G. Littman, and D. Kleppner, *Dynamical effects at avoided level crossings: A study of the Landau-Zener effect using Rydberg atoms*, Phys. Rev. A **23**, 3107 (1981).

[166] D. Jenkin *et al.*, *Bose-Einstein condensation of ^{87}Rb in a levitated crossed dipole trap*, Eur. Phys. J. D (2011).

[167] A. V. Smith, *Numerical studies of adiabatic population inversion in multilevel systems*, J. Opt. Soc. Am. B **9**, 1543 (1992).

[168] G. Barontini *et al.*, *Observation of Heteronuclear Atomic Efimov Resonances*, Phys. Rev. Lett. **103**, 043201 (2009).

[169] P. F. Bedaque, E. Braaten, and H.-W. Hammer, *Three-body Recombination in Bose Gases with Large Scattering Length*, Phys. Rev. Lett. **85**, 908 (2000).

[170] G. Pupillo, A. Micheli, H. P. Büchler, and P. Zoller, *Cold molecules: Theory, experiment, applications* (CRC Press, Boca Raton, 2009), chap. 4.

[171] V. Vuletić, C. Chin, A. J. Kerman, and S. Chu, *Suppression of Atomic Radiative Collisions by Tuning the Ground State Scattering Length*, Phys. Rev. Lett. **83**, 943 (1999).

[172] M. Trippenbach, K. Góral, K. Rzążewski, B. Malomed, and Y. B. Band, *Structure of binary Bose-Einstein condensates*, J. Phys. B **33**, 4017 (2000).

[173] E. Wille *et al.*, *Exploring an Ultracold Fermi-Fermi Mixture: Interspecies Feshbach Resonances and Scattering Properties of* ^6Li *and* ^{40}K, Phys. Rev. Lett. **100**, 053201 (2008).

[174] A. R. Allouche *et al.*, *Theoretical electronic structure of RbCs revisited*, J. Phys. B **33**, 2307 (2000).

[175] W. Stwalley, *Efficient conversion of ultracold Feshbach-resonance-related polar molecules into ultracold ground state* $(X^1\Sigma^+ v = 0, J = 0)$ *molecules*, Eur. Phys. J. D **31**, 221 (2004).

[176] M. Debatin *et al.*, *Molecular spectroscopy for ground-state transfer of ultracold RbCs molecules*, arxiv:1106.0129 (2011).

[177] C. R. LeSueur and J. M. Hutson, Private Communication (2011).

[178] L. J. LeBlanc and J. H. Thywissen, *Species-specific optical lattices*, Phys. Rev. A **75**, 053612 (2007).

[179] K. L. Butler, *Towards RbCs and YbCs ground-state molecules*, PhD First Year Report, Durham University (2011).

[180] S. G. Bhongale and E. Timmermans, *Phase Separated BEC for High-Sensitivity Force Measurement*, Phys. Rev. Lett. **100**, 185301 (2008).

[181] J. Catani, L. De Sarlo, G. Barontini, F. Minardi, and M. Inguscio, *Degenerate Bose-Bose mixture in a three-dimensional optical lattice*, Phys. Rev. A **77**, 011603 (2008).

[182] B. Damski *et al.*, *Creation of a Dipolar Superfluid in Optical Lattices*, Phys. Rev. Lett. **90**, 110401 (2003).

[183] D. Jaksch, V. Venturi, J. I. Cirac, C. J. Williams, and P. Zoller, *Creation of a Molecular Condensate by Dynamically Melting a Mott Insulator*, Phys. Rev. Lett. **89**, 040402 (2002).

[184] A. V. Gorshkov *et al.*, *Suppression of Inelastic Collisions Between Polar Molecules With a Repulsive Shield*, Phys. Rev. Lett. **101**, 073201 (2008).

[185] C. G. Townsend, N. H. Edwards, C. J. Cooper, K. P. Zetie, and C. J. Foot, *Phase-Space Density in the Magneto-Optical Trap*, Phys. Rev. A. **52**, 1423 (1995).